Fall 2009

Nonlinear evolution of annular layers and liquid threads in electric fields

Qiming Wang
New Jersey Institute of Technology

ABSTRACT

NONLINEAR EVOLUTION OF ANNULAR LAYERS AND LIQUID THREADS IN ELECTRIC FIELDS

by
Qiming Wang

The nonlinear dynamics of viscous perfectly conducting liquid jets or threads under the action of a radial electric field are studied theoretically and numerically here. The field is generated by a potential difference between the jet surface and a concentrically placed electrode of given radius. A long-wave nonlinear model that is used to predict the dynamics of the system and in particular to address the effect of the radial electric field on jet breakup is developed. Two canonical regimes are identified that depend on the size of the gap between the outer electrode and the unperturbed jet surface. For relatively large gap sizes, long waves are stabilized for sufficiently strong electric fields but remain unstable as in the non-electrified case for electric field strengths below a critical value. For relatively small gaps, an electric field of any strength enhances the instability of long waves as compared to the non-electrified case. Accurate numerical simulations are carried out based on our nonlinear models to describe the nonlinear evolution and terminal states in these two regimes. It is found that jet pinching does not occur irrespective of the parameters. Regimes are identified where capillary instability leads to the formation of stable quasi-static microthreads (connected to large main drops) whose radius decreases with the strength of the electric field. The generic ultimate singular event described by our models is the attraction of the jet surface towards the enclosing electrode and its contact with the electrode in finite time. A self-similar closed form solution is found that describes this event with the interface near touchdown having locally a cusp geometry. The theory is compared with the time-dependent simulations with excellent agreement.

In addition a core-annular flow problem is considered to include the external viscous fluid. A full problem simulation, based on a boundary integral technique is carried out to capture the full dynamics of the electrified viscous jet in the zero Reynolds number limit. Pinching solutions of either electrified or non-electrified viscous jets are obtained and the instantaneous velocity field and flow patterns are studied numerically near breakup. As the electric field strength increases, the size and shape of the drops are changed dramatically compared with the non-electrified problem. However, the local dynamics remain the same as shown in the non-electrified capillary breakup problem, since the main and satellite liquid masses joined by a collapsing neck have the same potential and would not feel the strong influence of the external field. The pinching is suppressed if the field strength is sufficiently large and another type of breakup behavior appears. Briefly speaking, the interface is attracted and touches the outer electrode in the radial direction in a similar phenomenon found for a single jet problem. This type of terminal state is also described by a lubrication model in the thin annulus limit. A comparison between the boundary-integral simulations and the asymptotic results is also carried out.

NONLINEAR EVOLUTION OF ANNULAR LAYERS AND LIQUID THREADS IN ELECTRIC FIELDS

by
Qiming Wang

A Dissertation
Submitted to the Faculty of
New Jersey Institute of Technology and
Rutgers, The State University of New Jersey – Newark
in Partial Fulfillment of the Requirements for the Degree of
Doctor of Philosophy in Mathematical Sciences

Department of Mathematical Sciences, NJIT
Department of Mathematics and Computer Science, Rutgers-Newark

January 2010

APPROVAL PAGE

NONLINEAR EVOLUTION OF ANNULAR LAYERS AND LIQUID THREADS IN ELECTRIC FIELDS

Qiming Wang

Demetrios T. Papageorgiou, Ph.D, Dissertation Advisor — Date
Professor, Department of Mathematical Sciences, NJIT
Department of Mathematics, Imperial College London, UK

Michael Siegel, Ph.D, Committee Member — Date
Professor, Department of Mathematical Sciences, NJIT

Michael Booty, Ph.D, Committee Member — Date
Professor, Department of Mathematical Sciences, NJIT

Peter G. Petropoulos, Ph.D, Committee Member — Date
Associate Professor, Department of Mathematical Sciences, NJIT

Pushpendra Singh, Ph.D, Committee Member — Date
Professor, Department of Mechanical and Industrial Engineering, NJIT

BIOGRAPHICAL SKETCH

Author: Qiming Wang

Degree: Doctor of Philosophy

Date: January 2010

Undergraduate and Graduate Education:

- Doctor of Philosophy in Mathematical Sciences,
  New Jersey Institute of Technology, Newark, NJ, 2010
- Master of Science in Applied Mathematics,
  New Jersey Institute of Technology, Newark, NJ, 2008
- Bachelor of Science in Mathematics,
  Nanjing University, Nanjing, China, July 2005

Major: Applied Mathematics

Publication:

Q. Wang and S. Mählmann and D. T. Papageorgiou, "Dynamics of liquid jets and threads under the action of radial electric fields: Microthread formation and touchdown singularities" *Phys. Fluids,* 21-032109, 2009.

To My Beloved Wife and Parents

ACKNOWLEDGMENT

I would like to give my special thanks to my advisor Prof. Demetrios T. Papageorgiou for his patient guidance, valuable advice and encouragement throughout. I am very fortunate to have had him as my advisor.

I am very grateful to Professors Pushpendra Singh, Michael Siegel, Michael Booty and Peter Petropoulos for agreeing to be on my committee and for their generous support during my study in NJIT. Discussions with Prof. Siegel and Prof. Booty are gratefully acknowledged. Special thanks are due to the Chair of the Department of Mathematical Sciences, Dr. Daljit Ahluwalia and Professors Robert Miura, Gregory Kriegsmann, Eliza Michalopoulou, Sheldon Wang, Shidong Jiang and Jonathan Luke.

Thanks to my friends, Xinli Wang, Yu Zhang, Fang Chu, Lingyan Shi, Tao Wu, Wen Deng, for their support both in my study and life and for providing such a pleasant environment during my stay at NJIT.

Finally, grateful thanks and deep appreciation to my beloved wife, Ye Yang, and my parents, Zhiqiang Wang and Shuping Jiao, for their precious love and great confidence in me. Without them this dissertation would have not been possible.

TABLE OF CONTENTS

TABLE OF CONTENTS
(Continued)

Chapter Page

LIST OF TABLES

Table **Page**

LIST OF FIGURES

LIST OF FIGURES
(Continued)

Figure **Page**

LIST OF FIGURES
(Continued)

Figure **Page**

LIST OF FIGURES
(Continued)

Figure **Page**

CHAPTER 1

INTRODUCTION

The effect of electric fields on the capillary instability of liquid jets is a fundamental problem found in several applications, including ink-jet printing, fuel atomization, electrohydrodynamic spraying of liquids and so on. Capillary instability in liquid cylinders manifests itself whenever the wavelength of the perturbation is longer than the undisturbed jet circumference. See the theoretical work of Rayleigh [52] and the subsequent analyses of Tomotika [64] and Chandrasekhar [8]. As the perturbation grows into the nonlinear regime the jet disintegrates into droplets and such terminal states were described recently in terms of similarity solutions of the Stokes and Navier-Stokes equations (Papageorgiou [45], Eggers & Dupont [17], Papageorgiou [44]). Direct simulations of capillary instability have also been carried out by several investigators including Day *et al.* [13] and Lister & Leppinen [34] (for inviscid drops or threads), Stone & Leal [61], Lister & Stone [36] and Pozrikidis [49] (for Stokes flows), and Ambravaneswaran *et al.* [2] (for Navier-Stokes equations). Good agreement between one and two-dimensional models, as well as the experimental work of Zhang & Basaran [68], have also been obtained. Comprehensive reviews have appeared recently by Eggers [16] and Eggers & Villermaux [18].

Although electric field effects have been an active research area for decades there is still considerable work that needs to be done to understand the underlying nonlinear dynamics and mechanisms. It has been pointed out by Basset [6] and observed experimentally in various configurations (see Raco [50], Taylor [62] and Ramos *et al.* [51]) that axial electric fields stabilize liquid bridges and jets and can act to support liquid bridge lengths beyond their critical Rayleigh length, for example. Comprehensive linear theories providing an explanation for the effect of axial electric

field stabilization have been carried out by Saville [54], [55], [56]. A more recent study on this is done by Volkov *et al.* [65] who applied boundary integral methods to calculate the equilibrium shapes of the electrified liquid bridge.

In the present study the nonlinear evolution of a viscous liquid thread or jet in the presence of radial electric fields driven by a cylindrical electrode placed coaxially to the undisturbed jet is considered. Linear stability analyses in this case have been carried out by Basset [6], Schneider et al. [58], Huebner & Chu [27] for both viscous and inviscid fluids, typically taken to be perfect conductors. The main findings are that electric charge tends to produce smaller droplets after breakup and evidence for this is presented in the experiments of Magarvey & Outhouse [40]. More recent work concentrating on absolute/convective instabilities of electrified jets under radial fields has been carried out by Artana et al. [4], [3], where it is shown that the electric field reduces perturbation wave speeds thereby increasing the parameter space where absolute instability emerges. The linear theory for an imperfectly conducting jet has been built up by Lopez-Herrera et al. [39] based on a leaky-dielectric model (Melcher & Taylor [41] and Saville [57]). The role of finite permittivity and conductivity has been explored and also the validity of lower order approximations was examined and discussed in detail. Interestingly the linear theories show that the electric stresses also tend to destabilize the non-axisymmetric modes. This phenomenon is observed experimentally as so called kink instabilities or whipping jets (e.g. Saville [56], Mestel [42] and Hohman *et al.* [24]).

The nonlinear dynamics of electrified jets under the action of radial fields have not received a lot of attention. Setiawan & Heister [59] computed the evolution of an inviscid jet using a boundary integral method and found that the terminal states can involve the usual main- and satellite-drop pinching states or, at higher electric field values, spiky features form without jet thinning. The latter states correspond to an axisymmetric Taylor cone and are a precursor to small droplet atomization taking

place around the periphery of the jet as was observed in the experiments of Cloupeau & Prunet-Foch [9] and Kelly [30]. The resolution of the computations in Setiawan & Heister [59], however, may be not sufficiently definitive to provide accurate terminal structures - in particular the minimum jet radii achieved may not be small enough for the stabilizing effects of the radial field to enter and compete, as our results in the present study. Such issues are addressed in the present work by performing accurate numerics for reduced systems.

In addition, a Korteweg-de Vries (KdV) equation is derived through a weakly nonlinear analysis for the inviscid jet in the long-wave limit. The electric force acts as a radial gravity term and hence plays the role of gravity in the classical water waves derivation. This is a novel and interesting application of the KdV in axisymmetric electrohydrodynamics.

In another related work, Lopez-Herrera et al. [38] consider one-dimensional models of electrified capillary jets placed in a coaxial electrode. They assume that the fluid is a perfect conductor and derive a model that includes viscosity and inertia. In addition they use the full curvature term in the normal stress balance (even though this is not correct asymptotically) following the ideas adopted by Lee [32], for example. (A comparison of the effect of different models and representations of the curvature on pinching singularities is given in Papageorgiou & Orellana [47].) The computations in [38] are mostly carried out for small Ohnesorge numbers (defined as $Oh = \mu/(\rho\gamma R_0)^{1/2}$ where μ, ρ, γ and R_0 are the fluid viscosity, density, surface tension coefficient and the undisturbed jet radius respectively) and pertain to fluids with small viscosities. In addition, the computations are not exhaustive enough to provide the definitive dynamics for large times - for example, it is not conclusive from the results that pinching does indeed take place and some results are presented where pinching appears to be arrested with a different terminal state becoming relevant. Such phenomena are computationally challenging and one objective of the present study is to obtain

accurate descriptions of terminal states at order one or large Ohnesorge numbers. Our findings indicate that according to the one-dimensional models, pinching does not occur but an interfacial cusp at a finite jet radius emerges instead. Similarity solutions that describe these terminal structures are also constructed, and confirmed numerically. It is intriguing to find, therefore, that the solutions near the singular time can be expressed in closed form. Recently the work by Collins *et al.* [11] shows, however, that pinchoff does happen for certain electrification levels in full simulations of the Navier-Stokes equations using finite-element methods. Those results suggest that the global effect of the electric field is important and the local approximation is rather inaccurate at some point (the axial velocity may depend on the radial coordinate) which may exaggerate the effect of the electric field in the vicinity of the breakup point. In the work of Collins *et al.* [11] they did an extensive and general computational investigation on the influence of electric stresses, capillary pressure and surface charges to the formation of satellites and breakup times. It turns out that the size of satellite drops will be bigger than the uncharged case and the main drops will be elongated in the direction of electric fields, which is similar to our findings as shown later. Another interesting result is that the charged Stokes jet breaks down asymmetrically not like the uncharged problem, which is due to the migration of the surface charge as the surface deforms. The sign reversal of the electric pressure, depending on the position of the electrode wall, accelerates the breakup and attributes to form a local thread, hence shifts the breakup points.

The core-annular flow problem is also studied in the present work by including the effect of external viscous fluid. The problem without electric effects is itself interesting enough, where the possible self-similar description of pinch-off solutions has been of considerable interest for decades. The analytic solution is described by Papageorgiou [45] for a single viscous jet in vacuum. The infinite liquid-liquid jet problem seems more complicated and no analytic solutions are available so far.

Lister & Stone [36] numerically solved the equal viscosity problem in the Stokes limit and showed evidence of self-similar collapse close to breakup with very high accuracy. Zhang & Lister [67] and Sireou & Lister [60] considered a wide range of viscosity ratios and solved the self-similar equations in a transformed domain but the question remains, and the real physical problems have not been solved as far as we know except for the computations of Pozrikidis [49]. In our work more accurate computations than these in the literature are carried out to capture the breakup and understand the nonlinear evolution for different ranges of viscosity ratios. In particular the satellite structure, as shown in a later section, is quite different as the viscosity ratio varies. For the case that the core-thread is more viscous than the surrounding fluid, $\lambda = \mu_{ext}/\mu_{int} \ll 1$ (μ the viscosity), the main drops become close to spherical and are connected with a thin microthread. In the opposite limit, i.e. the surrounding fluids more viscous, different satellite shapes form compared to the previous case, and appear to be visually similar to the results of Tjahjadi *et al.* [63]. Interestingly, the extreme limits, $\lambda = 0$ and $\lambda = \infty$ in which case the jet surface is symmetric in the axial coordinate near breakup, do not seem to connect with the finite λ shapes.

When the fluids are confined to a long cylindrical tube, the tube radius also affects the nonlinear evolution and pinching may be even suppressed. This problem was studied in a weakly nonlinear fashion by Papageorgiou *et al.* [46], where rich dynamics, governed by a modified Kuramoto-Sivashinsky equation, are explored in several distinct limits. A lubrication model was derived by Hammond [22] for an annular film and was recently revisited by Lister *et al.* [35]. Complex film drainage occurs at very long times with tiny film thickness and self-sustained axial motion driven by surface tension alone. Their results also showed that the long-time behavior depends on the length of the domain as well as initial conditions. Numerical computation of the full Stokes problem with arbitrary gap between the core-fluid surface and the

tube wall, through a boundary-integral technique, was carried out by Newhouse & Pozrikidis [43] for purely capillary-driven flows and Kwak & Pozrikidis [31] for flows with an interface covered by insoluble surfactant. Our present work will revisit some of their calculations and then include the effect of electric fields. Not surprisingly the electric force causes finite-time rupture and suppresses the axial motion found in the uncharged case when the annulus is thin. The coupled Stokes and Laplace problems for the fluid dynamics and electrostatics, respectively, are solved utilizing a similar boundary-integral method to that mentioned earlier.

The structure of the thesis is as follows: In Chapter 2 the physical model of electrohydrodynamics is introduced and the general governing equations as well as the dimensionless parameters are given. In Chapter 3 we begin by considering a single viscous jet subject to a radial electric field. Linear stability theory is carried out to gain some analytic insights. A one-dimensional model is then derived and used to investigate the nonlinear dynamics with or without inertia. Different nonlinear behaviors for various parameters are determined. Self-similar solution in the inertialess case is also constructed to describe flows that terminates in finite-time singularities. The effect of inertia is discussed through a simple scaling analysis. In addition, the reason for pinching being suppressed in the asymptotic model is given with the help of numerical simulations. A novel derivation of the KdV equation in the long-wave limit for an electrified inviscid thread is presented in Chapter 4. In Chapter 5 the general problem of core-annular flows by including the effect of annular fluids is considered. The numerical results of this chapter are presented based on boundary-integral methods. The Green's function for the electrostatic problem in a long tube with a periodic boundary condition is derived. In particular, we examine how the viscosity ratio, the dimensionless tube radius and the electric parameter affect the nonlinear behavior. Various breakup characteristics can be determined and a new type of breakup, 'splashing', is found as a transition between the core-fluid-pinching

solution and annular film-rupture solution. A lubrication model is also presented in the limit of thin annulus similar to the uncharged case (e.g. Hammond [22]) and the self-similar scalings are identified through accurate numerical simulations. Finally in Chapter 5 the results from the lubrication model and the full boundary-integral simulations are compared together. In Chapter 6 some concluding remarks are discussed.

CHAPTER 2

MATHEMATICAL FORMULATIONS

2.1 Flow Domain and Governing Equations

Axisymmetric viscous core-annular flows in cylindrical coordinates (r, z) are considered. The fluids are confined to a cylindrical tube (electrode) as illustrated in Figure 2.1. The parameters a and b are unperturbed thread radius and tube radius respectively. L is typically one period (later the problem is formulated in a periodic domain). The fluids are assumed to be immiscible, incompressible and the effect of gravity and buoyancy is neglected. For simplicity, the core fluids are assumed to be perfect

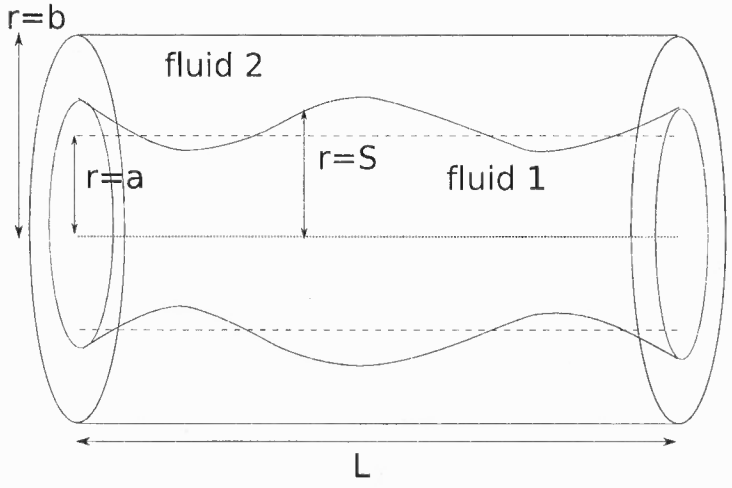

Figure 2.1 A sketch of the domain.

conductors and the annular fluids to be perfect dielectrics with no effective charge density at the interface. The radial electric field is generated by the potential difference between the interface and the outer electrode. Under this assumption, the time scale required for charge to move around the fluid surface is much smaller than the time

scale on which the hydrodynamics occurs. Therefore an electrostatic problem exterior to the core thread needs to be solved. Note that in the static case, the equations for the electric field and magnetic field are uncoupled. Since we are not interested in the effect of magnetic fields only the equations for the electric field will be considered. If the external magnetic field is absent magnetic effects can be completely ignored (see Saville [57]).

More specifically from Maxwell's equations the characteristic time scale for electric phenomena (charge relaxation time) and magnetic phenomena are

$$\tau_e = \frac{\epsilon_p}{\sigma}, \quad \tau_m = \mu_m \sigma l^2, \tag{2.1}$$

where ϵ_p, μ_m and σ are, respectively, the electric permittivity, magnetic permeability and electric conductivity of the material, and l is the characteristic length scale of the system. For a typical system in experiments (around 20^oC) with

$$\sigma = O(10^{-3}) \text{ S m}^{-1}, \quad \gamma = \text{O}(50) \text{ dyn cm}^{-1}, \quad \epsilon_\text{p} = \text{O}(50)\epsilon_0, \quad \mu_\text{m} = \text{O}(1)\mu_0, \tag{2.2}$$

where $\epsilon_0 \approx 8.854 \times 10^{-12}$ Fm^{-1} and $\mu_0 = 4\pi \times 10^{-7}$NA^{-2} are the electric permittivity and permeability of free space respectively, the time scale in (2.1) gives $\tau_e \sim 5 \times 10^{-7}$ s, and $\tau_m \sim 10^{-12}$ s for a 0.01 m jet and even smaller τ_m for thinner jet.

For the electrostatic problem, the electric potential is denoted by $\phi(r, z, t)$ and satisfies $\mathbf{E} = -\nabla\phi$, where $\mathbf{E}$ is the electric field and in component form we write $\mathbf{E} = (E_1, 0, E_2)$. Since $\mathbf{E}$ is divergence free, the electric potential satisfies Laplace's equation in the annular region $S(z, t) < r < b$,

$$\nabla^2 \phi = 0, \tag{2.3}$$

with boundary conditions $\phi = V_0$ on the wall and $\phi = 0$ at the interface, without loss of generality.

The governing equations for the fluids are then given by the Navier-Stokes equations and the continuity equation in the core (fluid 1) and annular (fluid 2) regions respectively.

$$\rho_i(\boldsymbol{u}_t + \boldsymbol{u}\cdot\nabla\boldsymbol{u}) = -\nabla p + \mu_i\nabla^2\boldsymbol{u}, \tag{2.4}$$

$$\nabla\cdot\boldsymbol{u} = 0, \tag{2.5}$$

where $\boldsymbol{u} = (u_r, u_z)$ is the fluid velocity vector, p is the pressure and ρ_i, μ_i, $i = 1, 2$ are respectively the density and viscosity of the fluids.

On the tube wall, the no-slip and no-penetration boundary conditions require that

$$\boldsymbol{u} = 0. \tag{2.6}$$

In addition, at the fluid interface, $F(r, z, t) = 0$, the kinematic condition is,

$$F_t + \boldsymbol{u}\cdot\nabla F = 0, \tag{2.7}$$

and tangential and normal stress balances ([ ] = indicates the jump from inside to outside)

$$[\boldsymbol{t}\cdot\boldsymbol{T}\cdot\boldsymbol{n}] = 0, \tag{2.8}$$

$$[\boldsymbol{n}\cdot\boldsymbol{T}\cdot\boldsymbol{n}] = -\gamma\kappa, \tag{2.9}$$

where $\boldsymbol{t}$ and $\boldsymbol{n}$ are unit tangential and normal vector respectively on the surface and κ is the curvature at the interface, defined as

$$\kappa = \frac{1}{S(1+S_z^2)^{1/2}} - \frac{S_{zz}}{(1+S_z^2)^{3/2}}, \tag{2.10}$$

with γ the coefficient constant surface tension, $\boldsymbol{T} = \sigma + \boldsymbol{M}$, a Newtonian stress tensor and a Maxwell stress tensor which are given by

$$\sigma = -p\boldsymbol{I} + \mu(\nabla \boldsymbol{u} + \nabla \boldsymbol{u}^T), \tag{2.11}$$

$$\boldsymbol{M} = \epsilon_p(\boldsymbol{E}\boldsymbol{E} - \tfrac{1}{2}\boldsymbol{I}|\boldsymbol{E}|^2). \tag{2.12}$$

2.2 Dimensionless Parameters

The problem is nondimensionalized using a for lengths, γ/μ_1 for velocities, γ/a for pressure, $\mu_1 a/\sigma$ for time and V_0 for the voltage potential:

$$(r, z) = a(r', z'), \quad (u_r, u_z) = \frac{\gamma}{\mu_1}(u_r', u_z'), \quad p = \frac{\gamma}{a}p', \quad t = \frac{\mu_1 a}{\gamma}t', \quad \phi = V_0\phi'. \tag{2.13}$$

The prime variables are dimensionless and we end with several parameters to measure the physical quantities,

$$R_e = \frac{\rho_1 \gamma a}{\mu_1^2}, \quad \chi = \frac{\rho_2}{\rho_1}, \quad \lambda = \frac{\mu_2}{\mu_1}, \quad d = \frac{b}{a}, \quad E_b = \frac{\epsilon_p V_0^2}{\gamma a}. \tag{2.14}$$

R_e is the Reynolds number; χ and λ are the density and viscosity ratios the of two fluids respectively; d is the dimensionless tube radius; E_b is the electric Taylor number which represents the ratio of electric to surface tension forces and measures the strength of the electric fields. Sometimes, the electric Taylor number is also described by $E_b = \epsilon_p E_\infty^2 a/\gamma$ (e.g. López-Herrera et al. [38]), where E_∞ is the electric field strength far away. Using (2.2) and taking the fluid viscosity to be $O(10)$ Pa s, the Reynolds number and the electric Taylor number are estimated as

$$R_e \sim 5 \times 10^{-3}, \quad E_b \sim 10^{-10} E_\infty^2. \tag{2.15}$$

So to obtain an electric Taylor number of $E_b = 1$, an electric field of strength $E_\infty = 10^5$ V/m is required. At a temperature of 25^oC, common water has electric permittivity $\epsilon_p = 80.1\epsilon_0$ with $\gamma = 71.97$ dyn/cm, while glycerol at 20^oC, has $\epsilon_p = 47\epsilon_0$

with $\gamma = 63$ dyn/cm. In order to cover certain ranges of viscosities and conductivities, mixtures of water and glycerol are usually used (see López-Herrera & Gañán-Calvo [37]) and they typically are of the order that is considered here. At the same time inertial effects are seen to be fairly small. In the present study, highly viscous flows are of particular interest and an asymptotic theory is built up for a single Stokes jet in Chapter 3. A boundary-integral simulation is carried out for Stokes flows in Chapter 5. The parameter estimates given above provide good support for our nonlinear modeling. Another relevant parameter for two-phase fluid systems is the Bond number, defined as

$$B_o = \frac{\triangle \rho g a^2}{\gamma}, \tag{2.16}$$

with g the acceleration due to the gravity and $\triangle p$ is the density difference between the fluids. The Bond number measures the relative importance of gravity over surface tension, and using the physical values given above $B_o = O(10^{-5})$. Hence, gravitational effects can be neglected in the problems considered here.

CHAPTER 3

ELECTRIFIED VISCOUS THREADS

In this chapter the axisymmetric deformation of a perfectly conducting, single viscous jet or thread under a radial electric field is considered. Hence $\mu_1 = \mu$ and $\rho_1 = \rho$ and fluid 2 is passive, i.e. air or vacuum ($\rho_2 = 0$, $\mu_2 = 0$). Using cylindrical coordinates (r, θ, z) and assuming axisymmetry, the fluid dynamics in the region $0 < r < S(z,t)$ (region 1, say) and for the electrostatics in $S(z,t) < r < d$ (region 2, say), where $r = S(z,t)$ denotes the jet interface, need to be solved.

3.1 Governing Equations

Nondimensionalization has already been introduced in Chapter 2. The dimensionless Navier-Stokes equations are (in cylindrical coordinates).

$$R_e\left(u_t + uu_r + uw_z\right) = -p_r + \Delta u - \frac{u}{r^2}, \tag{3.1}$$

$$R_e\left(w_t + uw_r + ww_z\right) = -p_z + \Delta w, \tag{3.2}$$

$$\frac{1}{r}(ru)_r + w_z = 0, \tag{3.3}$$

$$\Delta\phi = 0, \tag{3.4}$$

where

$$\Delta = \frac{\partial^2}{\partial r^2} + \frac{1}{r}\frac{\partial}{\partial r} + \frac{\partial^2}{\partial z^2}.$$

The parameter $R_e = (\gamma\rho a/\mu^2)$ is the square of the inverse Ohnesorge number, $Oh = (\mu/\sqrt{\gamma\rho a})$ - R_e is referred as a Reynolds number, as mentioned in Chapter 2. u and w are the radial and axial velocity components, respectively. ϕ is the voltage potential and note that the electrostatic problem needs to be solved in $S(z,t) < r < d$.

The boundary conditions at $r = S(z,t)$ are those of tangential and normal stress balances, a kinematic condition, and a zero equipotential condition for the voltage. Written out in full these read,

$$(u_z + w_r)(1 - S_z^2) + 2u_r S_z - 2w_z S_z = 0, \tag{3.5}$$

$$-p(1+S_z^2) + 2u_r + 2S_z^2 w_z - 2S_z(u_z + w_r) - E_b\left[\frac{1}{2}(1-S_z^2)(E_1^2 - E_2^2) - 2S_z E_1 E_2\right] = \frac{S_{zz} - (1+S_z^2)/S}{(1+S_z^2)^{3/2}}, \tag{3.6}$$

$$u = S_t + wS_z, \tag{3.7}$$

$$\phi(S(z,t), z, t) = 0. \tag{3.8}$$

Recall that the dimensionless parameter $E_b = (\epsilon_0 V_0^2/\gamma a)$ represents the ratio of electric to surface tension forces and measures the strength of the electric field. In addition to the interfacial conditions (3.5)-(3.8) regularity conditions are required for the velocities at $r = 0$ and a Dirichlet condition for ϕ at the cylindrical electrode

$$\phi(d, z, t) = 1, \tag{3.9}$$

where $d = (b/a)$ is the dimensionless radius of the cylindrical electrode (note that $0 < S(z,t) < d$, unless the jet pinches or touches the outer electrode).

3.2 Linear Stability

3.2.1 Characteristic Equation

Linear stability theory is used to investigate the behavior of a small disturbance to an initially uniform, unbounded liquid thread stressed by a radial electric field. The base states are

$$u = w = 0, \qquad p = 1 - \frac{E_b}{2(\ln d)^2}, \qquad S = 1, \qquad \phi = \frac{\ln r}{\ln d}, \tag{3.10}$$

and it is assumed that infinitesimally small perturbations have the normal-mode form

$$\left(\tilde{u}, \tilde{w}, \tilde{f}\right) = \left(\hat{u}, \hat{w}, \hat{f}\right)(r)\exp(ikz + \omega t), \tag{3.11}$$

where k is the wavenumber, ω the growth rate of the disturbance and $\tilde{f}$ denotes a perturbation function which can be pressure, interface position or electric potential.

The linearized field equations become:

$$R_e\omega\hat{u} = -\hat{p}' + \hat{u}'' + \frac{\hat{u}'}{r} - k^2\hat{u} - \frac{\hat{u}}{r^2}, \tag{3.12}$$

$$R_e\omega\hat{w} = -ik\hat{p} + \hat{w}'' + \frac{\hat{w}'}{r} - k^2\hat{w}, \tag{3.13}$$

$$\frac{1}{r}(r\hat{u})' + ik\hat{w} = 0, \tag{3.14}$$

$$\hat{\phi}'' + \frac{1}{r}\hat{\phi}' - k^2\hat{\phi} = 0, \tag{3.15}$$

where $' = d/dr$. The linearized version of the tangential and normal stress balance equations (3.5), (3.6) and also the kinematic condition (3.7), on $r = 1$ read

$$-\hat{p} + 2\hat{u}' - p^e = -k^2\hat{S} + \hat{S}, \tag{3.16}$$

$$ik\hat{u} + \hat{w}' = 0, \tag{3.17}$$

$$\hat{u} = \omega\hat{S}, \tag{3.18}$$

where p^e denotes the linearized Maxwell stress contribution to (3.6).

Then in a similar manner to Tomotika [64] and Papageorgiou [45], for example, the linear system is solved to obtain the characteristic equation determining the growth rate $\omega(k)$, to find

$$R_e\omega^2 F(k) + 2k^2\omega(2F(k) - 1) + \frac{4k^4}{R_e}(F(k) - F(\tilde{k})) - k^2(1 - k^2 - p^e) = 0, \tag{3.19}$$

where $F(k) = kI_0(k)/I_1(k)$, $\tilde{k}^2 = k^2 + R_e\omega$ and p^e comes from solving the Laplace equation in region 2 and evaluating the Maxwell stresses at $r = 1$ (see also Saville

[56] and Collins *et al.* [11])

$$p^e = \frac{E_b}{\ln^2 d}\left(1 + k\frac{K_0(kd)I_1(k) + I_0(kd)K_1(k)}{I_0(k)K_0(kd) - I_0(kd)K_0(k)}\right). \tag{3.20}$$

It is noticed immediately that (3.19) recovers the result of an uncharged jet when $E_b = 0$ and this serves as a quick check for our results.

The stability for a highly viscous jet and inviscid jet can be obtained from (3.19) by taking appropriate limits. In the viscous limit, $R_e \to 0$, the effect of inertia can be neglected relative to viscosity. Consider the Taylor series of $F(\tilde{k})$ for small R_e so that

$$\tilde{k} \approx k + \frac{R_e\omega}{2k}, \tag{3.21}$$

to find that (3.19) becomes

$$2\omega(F(k)^2 - 1 - k^2) - (1 - k^2 - p^e) = 0, \tag{3.22}$$

which coincides with the result in Wang *et al.* [66], where (3.22) is derived by directly solving the linearized system with $R_e = 0$. In another limit, the inviscid limit, $R_e \to \infty$, viscosity can be neglected relative to inertia and $\tilde{k}$ can be written as

$$\tilde{k} \approx (R_e\omega)^{1/2}\left(1 + \frac{k^2}{2R_e\omega}\right). \tag{3.23}$$

After some algebra, (3.19) becomes

$$\omega^2 = \frac{k^2(1 - k^2 - p^e)}{R_e F(k)}. \tag{3.24}$$

In the inviscid case the nondimensionalization is different in that the time scale is taken as $(\rho a^3/\gamma)^{1/2}$ instead of $\mu_1 a/\gamma$. Therefore (3.24) turns out to be, after rescaling,

$$\omega^2 = \frac{k^2(1 - k^2 - p^e)}{F(k)}. \tag{3.25}$$

3.2.2 Long-wave Expansion

The characteristic equation (3.19) is complicated since $\tilde{k}$ is a function of ω and is contained in the arguements of the Bessel functions. In order to get analytic insight, simplified equations in the long-wave limit $k \to 0$ is considered. Thus (3.19), assuming $R_e\omega \ll 1$, becomes

$$2R_e\omega^2 + 6k^2\omega - k^2(1-\alpha) = O(k^4, k^2\omega, \omega^2), \tag{3.26}$$

where $\alpha = E_b(\ln d - 1)/(\ln d)^3$. Immediately it is seen that some transition would happen at $\ln d = 1$ which indicates that the electric fields do not affect the linear stability in the long-wave limit at this point. By solving equation (3.26) for ω, the following relation is found,

$$\omega(k) = \frac{-3k^2 \pm (9k^2 - 2R_e(\alpha-1))^{1/2}k}{2R_e}, \tag{3.27}$$

and it is seen that the instability occurs when $\alpha < 1$ while $\alpha = 1$ gives the neutral stability. In addition, negative α always gives instability which corresponds to the case $d < e \approx 2.7183$, irrespective of E_b. This implies the necessity of investigating this case since in the literature (e.g. Satiawan & Heister [59], Lopez-Herrera et al. [38] and Collins *et al.* [11]) people usually take $d = 10$ which is far away from the critical value e. In the highly viscous and inviscid limit the same result is obtained in the long-wave limit, since, as we mentioned, the electric effect only enters the normal stress balance that gives the term $1 - k^2 - \alpha$. To summarize, then, the following expressions are obtained in the long-wave limit from the full dispersion relation ((3.22) and (3.24))

$$\omega(k) = \frac{1}{6}(1-\alpha), \quad \text{as} \quad R_e \to 0, \tag{3.28}$$

and

$$\omega^2(k) = \frac{k^2}{2R_e}(1-\alpha), \quad \text{as} \quad R_e \to \infty. \tag{3.29}$$

They will be revisited when the long-wave model is discussed. On the other hand, for $\ln d > 1$, increasing E_b is stabilizing against capillarity and stable wave solutions ($\alpha > 1$) might be expected when inertia is present (Grandison *et al.* [21] and Gleeson *et al.* [20]). However it should be noted that non-axisymmetric modes may dominate when the electrification level is too high (Saville [56]). Different breakup modes are identified asymptotically by Hohman *et al.* [24].

3.2.3 A Note on The Linear Stability of An Imperfectly Conducting Jets

For a poorly conducting jet, the governing equations for the electric potential follow the leaky-dielectric model (e.g. Saville [57]). The long-wave axisymmetric perturbation is still of interest and after some algebra the growth rate in highly viscous jets (the derivation not shown here) becomes

$$\omega(k) = \frac{1}{6}\left(1 + \frac{3 - 4\ln d}{\ln^2 d} E_b\right). \tag{3.30}$$

Similar to the perfect conductor case the electric field still has the stabilizing effect depending on d and E_b and it is observed that poor-conductor assumption only shifts the 'critical' value on the parameters. For example, in the case of perfect conductor, the dispersion relation in long-wave limit indicates that $d = e$ for fixed E_b is critical. Going below or above it will give different dynamic behaviors, while in the poor conductor case, the critical value for d is $e^{3/4} \approx 2.117$. Similar results in the long-wave limit but for different viscosity ranges have been obtained by Lopez-Herrera et al. [39].

3.3 Long-wave Model

A slenderness parameter δ is introduced such that

$$\frac{\partial}{\partial r} \to \frac{\partial}{\partial r}, \qquad \frac{\partial}{\partial z} \to \delta \frac{\partial}{\partial z}, \tag{3.31}$$

and no confusion should be caused by the same symbol z being used for the scaled axial coordinate. In addition $d \ll \delta^{-1}$ is assumed. The asymptotic analysis is similar to that of Papageorgiou [45], Craster et al. [12] who analyzed the non-electrified problem.

Applying the change of variables (3.31) to (3.4) and the expansion $\phi = \phi_0 + \delta^2\phi_1 + \ldots$, leads to the leading order problem

$$\frac{1}{r}\frac{\partial}{\partial r}\left(r\frac{\partial \phi_0}{\partial r}\right) = 0, \tag{3.32}$$

$$\phi_0(S(z,t),z,t) = 0, \qquad \phi_0(d,z,t) = 1. \tag{3.33}$$

The solution is

$$\phi_0(r,z,t) = \frac{\ln(r/S)}{\ln(d/S)}. \tag{3.34}$$

The appropriate expansions in region 1 are

$$\begin{aligned} u &= u_0 + \delta^2 u_1 + \ldots, \quad w = \frac{1}{\delta}w_0 + \delta w_1 + \ldots, \\ p &= p_0 + \delta^2 p_1 + \ldots, \quad S = S_0 + \delta^2 S_1 + \ldots \end{aligned} \tag{3.35}$$

which on substitution into the Navier-Stokes equations (3.2), (3.3) and then (3.1) and consideration of the leading order problem yields

$$\frac{1}{r}(rw_{0r})_r = 0 \quad \Rightarrow \quad w_0 \equiv w_0(z,t), \tag{3.36}$$

$$\frac{1}{r}(ru_0)_r + w_{0z} = 0 \quad \Rightarrow \quad u_0(r,z,t) = -\frac{r}{2}w_{0z}, \tag{3.37}$$

$$u_{0rr} + \frac{1}{r}u_{0r} - \frac{1}{r^2}u_0 = p_{0r} \quad \Rightarrow \quad p_{0r} = 0 \quad \Rightarrow \quad p_0 \equiv p_0(z,t). \tag{3.38}$$

Using (3.36)-(3.38) into the normal stress balance (3.6) at $r = S_0$ provides an expression for the leading order pressure at a given axial position,

$$p_0 + w_{0z} + \frac{E_b}{2S_0^2[\ln(d/S_0)]^2} = \frac{1}{S_0}. \tag{3.39}$$

One evolution equation (corresponding to mass conservation) connecting the leading order quantities w_0 and S_0 follows from the kinematic condition (3.7) at leading order, and reads

$$S_{0t} + \frac{1}{2}S_0 w_{0z} + S_{0z}w_0 = 0. \tag{3.40}$$

To close the system we need to proceed to the next order solution of the Navier-Stokes system and its boundary conditions (the tangential stress balance (3.5) enters at this order). In order to retain inertia in the second order terms of (3.2), the canonical scaling $R_e = \delta^2\mathscr{R}$ with $\mathscr{R}$ a positive constant is chosen. At order δ, then, the axial momentum balance becomes

$$\mathscr{R}(w_{0t} + w_0 w_{0z}) = -p_{0z} + \frac{1}{r}\left(r w_{1r}\right)_r + w_{0zz}. \tag{3.41}$$

Since all terms in (3.41), except the one containing w_1, are independent of r, we integrate and use regularity at $r = 0$ to obtain

$$w_{1r} = \frac{r}{2}\left[\mathscr{R}(w_{0t} + w_0 w_{0z}) - w_{0zz} + p_{0z}\right]. \tag{3.42}$$

The second evolution equation connecting w_0 and S_0 arises from the tangential stress balance condition (3.5) at leading order (order δ; the $O(\delta^{-1})$ equation is satisfied identically), which provides an expression for $w_{1r}(S_0, z, t)$; equating with (3.42) and evaluating at $r = S_0$, after some algebra the equation becomes

$$\mathscr{R}\left(w_{0t} + w_0 w_{0z}\right) = \frac{3\left(S_0^2 w_{0z}\right)_z}{S_0^2} - \left(\frac{1}{S_0}\right)_z + \frac{E_b}{2}\left(\frac{1}{S_0^2[\ln(d/S_0)]^2}\right)_z. \tag{3.43}$$

The evolution is governed by the nonlinear system (3.40) and (3.43) (see also Eggers & Dupont [17] and Craster *et al.* [12]). When $E_b = 0$ the system is that derived and studied by Eggers & Dupont ([17]), while in the additional limit $\mathscr{R} = 0$ the inertialess Stokes flow model of Papageorgiou [45] is obtained. We are in a position, therefore, to evaluate quantitatively the effect of the radial electric field on capillary instability and jet pinching. In what follows the subscript zero is dropped from the dependent variables and the problem on 2π spatially periodic domains is considered.

3.3.1 Conserved Quantities

Equation (3.40) represents mass conservation which can be seen by multiplication by S and integration with respect to z to obtain

$$\int_{-L}^{L} S^2 dz = \texttt{const}, \tag{3.44}$$

where $2L$ periodicity is assumed. Equation (3.43) represents conservation of momentum, that is

$$\int_{-L}^{L} S^2 w dz = \texttt{const}. \tag{3.45}$$

To show this (3.43) is multiplied by S^2 and the left hand side is rewritten as

$$\mathscr{R}\left[(S^2 w)_t - (S^2)_t w + S^2 w w_z\right],$$

which on elimination of $(S^2)_t$ from (3.40) and manipulation of the right hand side, casts (3.43) into

$$\mathscr{R}\left[(S^2 w)_t + (S^2 w^2)_z\right] = 3(S^2 w_z)_z + S_z - E_b\left(\frac{1}{\ln(d/S)} - \frac{1}{2[\ln(d/S)]^2}\right)_z. \tag{3.46}$$

This is a conservation law for $S^2 w$ and integration in z and use of periodicity gives the result (3.45). Both conserved quantities are utilized to monitor the accuracy of the numerical calculations described later.

3.3.2 Linear Stability Properties

Linearizing equations (3.40) and (3.43) about the undisturbed states $S = 1$, $w = 0$, and looking for solutions proportional to $\exp(ikz+\omega t)$, yields the following dispersion relation

$$\mathscr{R}\omega^2 + 3k^2\omega - \frac{1}{2}\left(1 - \frac{E_b(\ln d - 1)}{(\ln d)^3}\right)k^2 = 0. \tag{3.47}$$

which is consistent with the result (3.26) that was derived in section 3.2.2. In the Stokes limit $\mathscr{R} = 0$

$$\omega(k) = \frac{1}{6}\left(1 - \frac{E_b(\ln d - 1)}{(\ln d)^3}\right) \tag{3.48}$$

is found, which agrees with Papageorgiou [45] in the absence of an electric field, $E_b = 0$. It follows that if $\ln d > 1$ the electric field is increasingly stabilizing as E_b increases, whereas increasing destabilization takes place if $\ln d < 1$.

In understanding the numerical solutions that are presented later (in particular the formation of stable slender secondary threads), it is useful to consider the linear stability of the system about the state $S = a$, $w = 0$, where $0 < a < d$ is some constant. The growth rate in this case is

$$\omega(k) = \frac{1}{6}\left(\frac{1}{a} - \frac{\ln(d/a) - 1}{a^2 \ln^3(d/a)}E_b\right). \tag{3.49}$$

As $a \to 1$ (3.48) is recovered; the more relevant regime is $0 < a < 1$ for which neutral stability is always possible for non-zero E_b and a sufficiently small thread radius a, with stabilization of thinner threads. The reason for this is that as $a \to 0$ the electric field term dominates in (3.49). The physical reason for this is that the electric field pressure at the surface of a sufficiently thin thread dominates the capillary pressure which scales with $1/a$. Since the former pressure is stabilizing it competes and overcomes the capillary pressure that tends to pinch the thread. This mechanism is seen in the nonlinear calculations described later.

3.4 Results and Discussion

In this section the equations (3.40) and (3.43) are considered and solved numerically together with some analytic descriptions. The Stokes jet is investigated first and the results of Navier-Stokes jet are also presented.

3.4.1 Numerical Method

The highly nonlinear partial differential equations (3.40) and (3.43) are solved numerically through a pseudo-spectral method (e.g. Papageorgiou [45]) and advanced in time using a fourth order Runge-Kutta method, where proper filters are employed to smooth the calculation as explained below. Another code, EPDCOL (Keast & Muir [29]), is also used to solve the initial value problem and serves as a check. The numerical routine, which utilizes finite-element collocation in space and Gear's method in time, has been proven to be accurate and efficient for the jet problem (e.g Craster *et al.* [12]). In general, the numerical solutions are determined starting from the initial condition

$$S(z,0) = 1 + 0.5\cos(\pi z/L), \quad w = 0, \tag{3.50}$$

together with the boundary conditions

$$S_z(\pm L, t) = S_{zzz}(\pm L, t) = 0, \quad w(\pm L, t) = 0, \tag{3.51}$$

where $-L \leq z \leq L$.

In the case $\mathscr{R} = 0$, only the initial condition for S is needed and the axial velocity can be determined immediately from the momentum equation. To see this let $\chi = S - E_b\left(\frac{1}{\ln(d/S)} - \frac{1}{2[\ln(d/S)]^2}\right)$ and integrate (3.43) once to obtain

$$w_z = \frac{1}{3}\left(\frac{k(t) - \chi}{S^2}\right), \tag{3.52}$$

where $k(t)$ is to be found. A further integration over one period gives

$$k(t) = \frac{\int_0^{2\pi}(\chi/S^2)dz}{\int_0^{2\pi}(1/S^2)dz}. \tag{3.53}$$

Equation (3.52) shows that w follows from S and hence an initial condition on w would over specify the problem. The numerical method is similar to Papageorgiou [45] and utilizes the integrated form (3.52). A pseudo-spectral method is employed and all required integrals are evaluated spectrally (whether by computing the Fourier transform of the integrand or by using a trapezoidal quadrature) . The numerical procedure starts with knowing the shape S at either $t = 0$ or at a given time level and using it in (3.53) to compute $k(t)$. With $k(t)$ known we integrate (3.52) to obtain w - this is done by inverting $-i/k\hat{H}$, where $\hat{H}$ is the Fourier transform of the right hand side of (3.52) (the mode $k = 0$ is set to zero due to the odd parity of w). With w updated, S can be evolved through the kinematic condition (3.40). The derivative S_z is computed spectrally and time integration is done in real space using a fourth order Runge-Kutta method.

The numerical method deals with aliasing errors by employing a cutoff filter of the form (see Hou & Li [25])

$$e^{-c_0(2|k|/N)^p}\hat{f}(k), \tag{3.54}$$

which sets to zero all Fourier coefficients which are below the filter level ϵ_f. Unless otherwise specified, typical values used here are $c_0 = 36, p = 36, \epsilon_f = 10^{-12}$. The filter is implemented at every time step and whenever a fast fourier transform (FFT) is used. In order to resolve the solution near a finite time singularity, an adaptive method is implemented to gain spatial accuracy when needed. The computation monitors the index of the smallest non-zero Fourier mode after every filter operation. If this index is greater than $N/4$, where N is the number of current grid points, the solution is padded with zeroes in Fourier space to a transform containing $2N$

modes. An inverse FFT provides a spectrally interpolated solution in real space. The higher spatial resolution requires a smaller time step to preserve stability and this is implemented by choosing an empirical constant $C < 1$ and updating the time step using $\triangle t = C/N^{3/2}$. The adaptive method stops if the minimum value of the difference between jet and electrode, $d - S_{max}$ say, is less than 10^{-7}, i.e. right before the surface touches the outer electrode, or if S_{min} (the shape minimum) is less than 10^{-7}, or if the number of points becomes larger than 256^2. These stopping criteria are sufficient to produce an accurate almost singular solution that agrees with the self-similar asymptotic theory developed later.

In the Stokes limit the model contains two dimensionless parameters, d and E_b, that correspond to the distance between the undisturbed cylindrical liquid surface and the outer electrode, and the strength of the electric field, respectively. According to the linear dispersion relation (3.48), it is established that if $\ln(d) < 1$ the liquid jet will be linearly unstable, while if $\ln(d) > 1$ then linear stability ensues if $E_b > E_{bc} = (\ln d)^3/(\ln d - 1)$. Both of these cases are considered and in particular the dynamics is followed numerically into the nonlinear regime.

3.4.2 Stokes Jet: $\ln(d) > 1$

Numerical solutions are first presented for the system (3.40) and (3.43) in the Stokes limit $\mathscr{R} = 0$. In order to fix things the effect of the radial electric field on the dynamics when $d = 5$ is considered. Note that this implies the value $E_{bc} \approx 6.84$ and so according to linear theory the jet is unstable if $E_b < 6.84$ and stable if $E_b > 6.84$.

The relatively large initial condition (3.50) with $L = \pi$ places us outside the realm of linear theory, but as the latter suggests, two distinct behaviors are found depending on the value of E_b. If E_b is sufficiently small (smaller than a number between 1 and 1.5 for the present set of parameters - this is smaller than $E_{bc} \approx 6.84$ due to the size of the initial disturbances), we find that the shape evolves to a sequence

of large drops connected with very thin stable threads whose radius decreases with decreasing E_b. Figure 3.1 ($L = \pi$) depicts the evolution of S and w for $E_b = 1$ as well as the corresponding electric stresses (square of surface charge density q), defined as

$$q^2 = \frac{1}{S^2 \ln^2(d/S)}, \tag{3.55}$$

which relates the electric pressure as

$$p^E = -\frac{E_b}{2} q^2, \tag{3.56}$$

and the minimum thread thickness S_{min}. At early stages the shapes of the surface and the axial velocity (Figure (3.1) (a), (b)) evolve in a fashion reminiscent of non-electrified inertialess jet breakup (see Papageorgiou [45]) but at large times breakup is arrested and a long thin thread survives connecting neighboring drops. The surface charge begins to accumulate around the center-thread part as seen in panel (c), and panel (d) shows that S_{min} becomes almost a constant. The magnitude of the axial velocity decreases monotonically with time but eventually sharp features evolve at large times as can be seen in the results of Figure 3.2 which show the final computed interfacial profile and corresponding axial velocity. It is observe that S becomes increasingly steeper with time and w appears to be forming a cusp singularity - eventually the interfacial slope becomes unbounded and violates the long wave approximation. What is particularly striking, however, is the stabilization and formation of the thin connecting threads. Considering the results of Figure 3.1(d) for $E_b = 1$, for example, the asymptotic value $S_{min} \approx 0.022872$ is found. The linear result (3.49) predicts a balance between capillary destabilization and electric field stabilization (i.e. neutral stability) at a value $a \approx 0.0311$ and the agreement is seen to be good - a possible source for the discrepancy is the fact that the linear stability is performed about a uniform quiescent state which is not quite the case in the quasi-static stages of the dynamics.

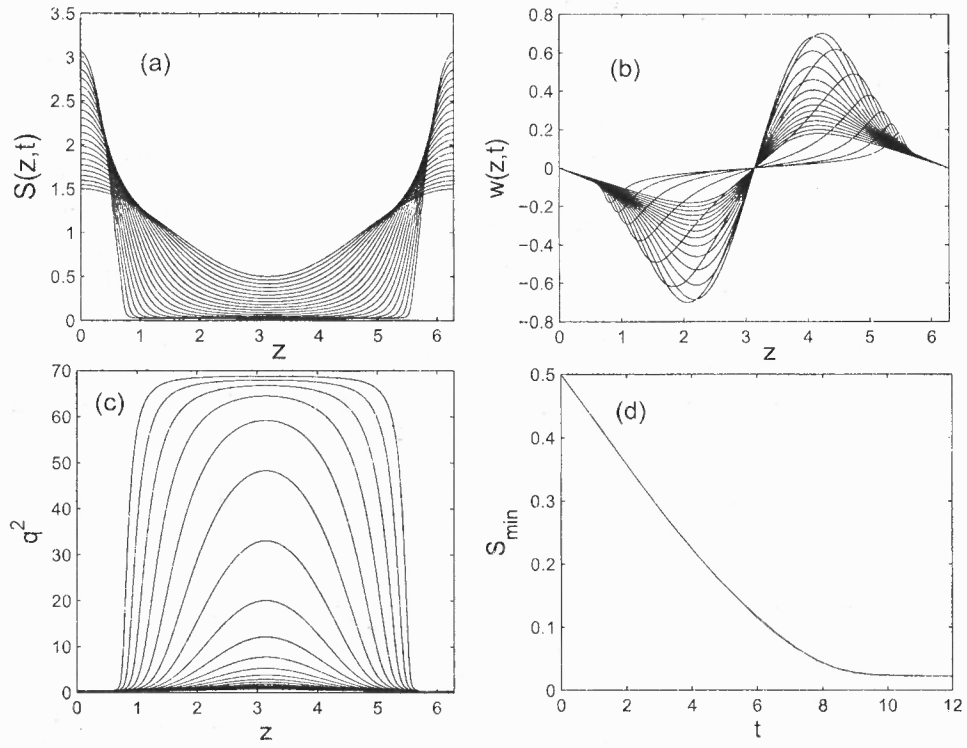

Figure 3.1 (a) Evolution of the interfacial shape $S(z,t)$, (b) the axial velocity $w(z,t)$, and, (c) the electric stresses, (d) the S_{min}. $d = 5, E_b = 1.0$ and the final time is 12 time units.

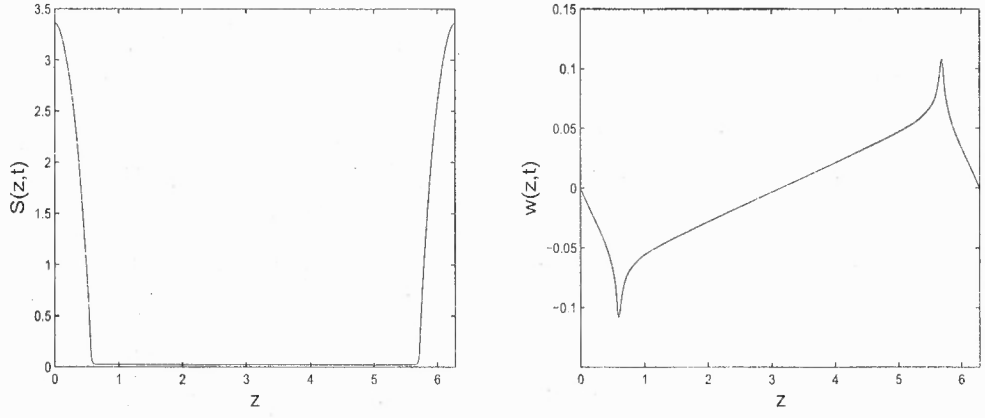

Figure 3.2 The solutions at the final computed time $t = 12$ for $d = 5, E_b = 1$. (left panel) Interfacial shape S, (right panel) the axial velocity w.

Small values of E_b are also attempted in the numerical simulations and even for a very weak electric effect a thin thread is formed eventually. A typical example

for $E_b = 0.1$ is shown in the left panel of Figure 3.3 and a comparison between the nonlinear calculations and linear predictions is performed in the right panel of the same figure. In the left panel, $S_{min} \approx 8.2 \times 10^{-4}$ and it is amplified in the insets for the local thread formation and the corresponding axial velocity (dark line) which is similar to the results in Figure 3.2. This suggests that the linear result (3.49) can be used to predict the radius of the stable thin threads that can form in this regime.

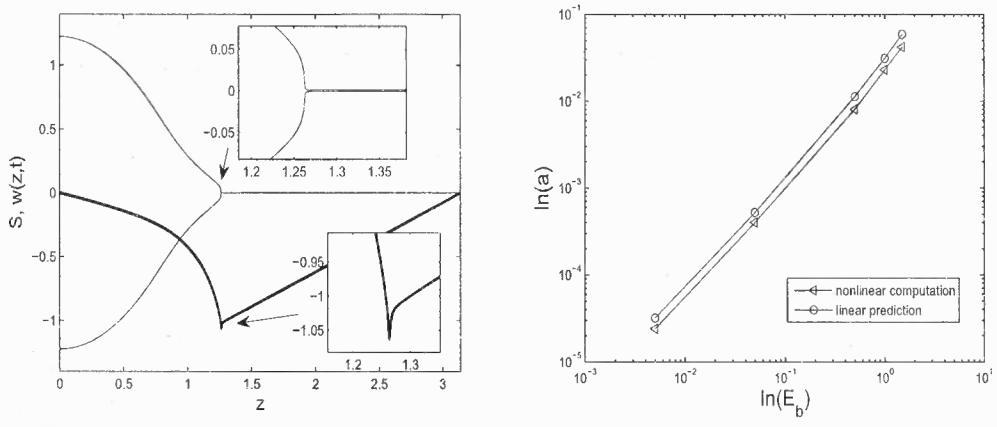

Figure 3.3 Final computed stage for the Stokes jet profile S with corresponding axial velocity w in the case $d = 5$ and $E_b = 0.1$. The local formation of the microthread is illustrated in the small box above. (Right) S_{min} for different E_b. $\Delta-$ numerical computation; $\circ-$ prediction of linear theory

Next we consider larger values of E_b but still small enough to make ω in (3.48) positive. $E_b = 5$ ($d = 5$ is fixed) is chosen and the left panel of Figure 3.4 shows that in this case the dynamics are significantly different from those corresponding to the smaller values of E_b described above. It is found that the local interfacial maximum in the initial condition spikes up and eventually touches the wall in finite time (the bounding top horizontal line in the figure is the position of the electrode at $r = 5$); the corresponding axial velocity develops an infinite slope singularity at the terminal time (not shown here) and the slenderness assumption is violated. The mathematical structure of these solutions is analyzed later and we show that the dynamics is self-similar. It is interesting to note that such terminal behavior is found

for other parameter values also and that the structures observed are cylindrically symmetric analogues of a Taylor cone.

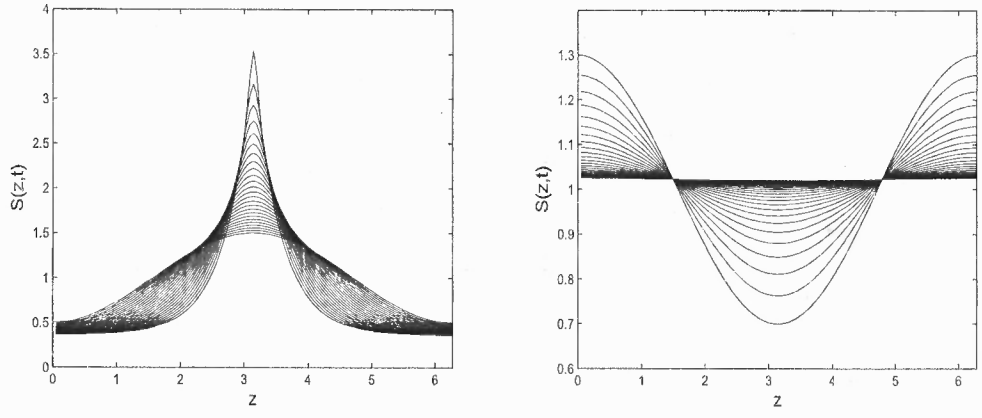

Figure 3.4 Evolutions of the thread interface S for (left) $d = 5$, $E_b = 5$ and (right) $d = 5$, $E_b = 10$.

For E_b bigger than E_{bc}, the electric field is stabilizing and the deformed jet surface returns to a flat state (see the right panel of Figure 3.4) under the consideration of axisymmetric perturbations. Of course as mentioned above, in this case high electrification level risks the activation of non-axisymmetric modes that are not covered by our model.

3.4.3 Stokes Jet: $\ln(d) < 1$

Taking $\ln(d) < 1$ in the linear dispersion relation (3.48) shows that the growth rate is a positive increasing function of E_b. To illustrate the dynamics typical values $d = 2$, $E_b = 2$ are chosen and the initial condition is the same as before. The evolution along with computed profiles at the final time $t \approx 0.19798$ are shown in Figure 3.5. The solutions terminate in a finite time singularity with the interface touching the wall electrode with a cusp geometry, and the corresponding axial velocity attaining a shock discontinuity in the vicinity of the touchdown point. Self-similar dynamics are again at play as will be shown later. The evolution of q^2 is shown in panel (c) of Figure

3.5 indicating the accumulation of charge near the sharp geometry when it is close to the electrode. Panel (d) shows the evolution of the minimum distance $d - S_{max}$ of the interface from the cylindrical electrode. The results show the fast touchdown at the final stages of the evolution and indicate that the approach to touchdown occurs with an infinite time rate of change (the slope of the curve is infinite and in fact it will be shown later that $d - S_{max} \sim (t_s - t)^{1/3}$ as $t \to t_s$ where t_s is the singular time). The rate of blow-up is determined analytically in a subsequent section. The

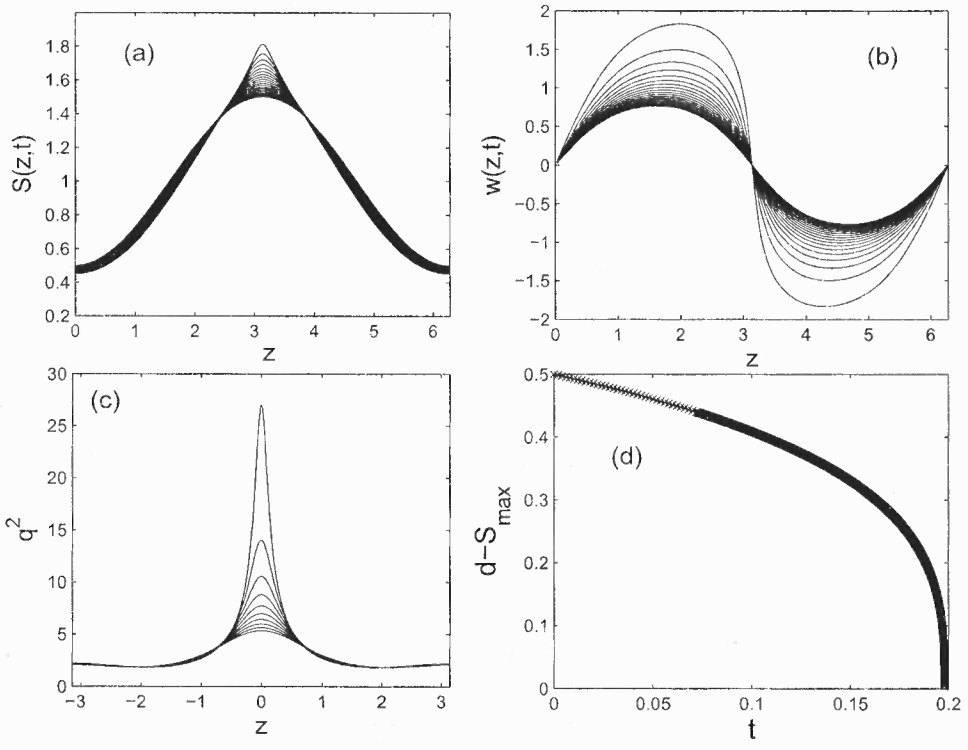

Figure 3.5 (a) Evolution of the interfacial shape $S(z,t)$, (b) the axial velocity $w(z,t)$, and, (c) the electric stresses, (d) the $d - S_{max}$. $d = 2$, $E_b = 2$ is fixed.

overall behavior is analogous to the $\ln(d) > 1$ cases at intermediately large values of E_b as computed in the example of figure 3.4. As E_b increases we have verified numerically (not included here) that the solution terminates with the same type of singular behavior but at smaller terminal times.

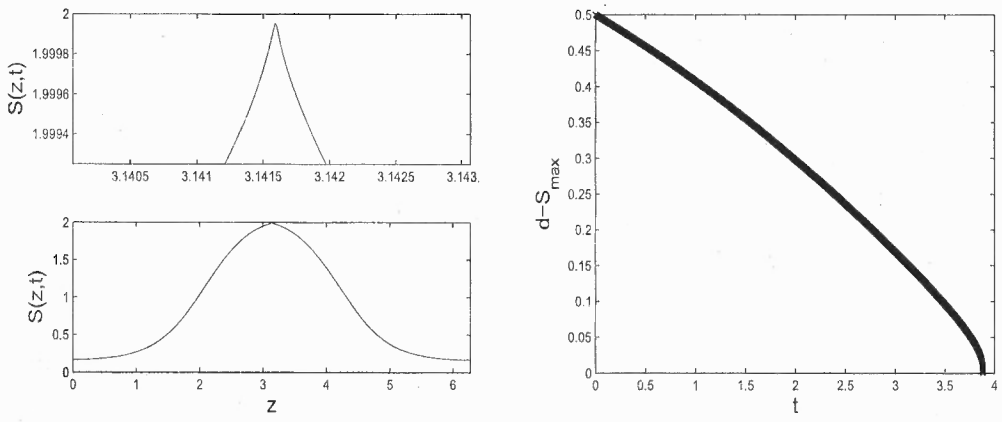

Figure 3.6 Touchdown with spike formation for small $E_b = 0.001$, $d = 2$. Left panels show the interface at the last computed time along with a magnification of the nearest approach region (top panel). Right panel shows the evolution of $d - S_{max}$ indicating the fast dynamics at the very late stages.

The dynamics are more intricate at very small values of E_b that correspond to a weak electric field. Ultimately a self-similar behavior at the very final stages of the evolution is obtained but the dynamics are altered resulting in significantly higher computational costs. A typical example with $E_b = 0.001$ ($d = 2$ as before) reveals that initially the evolution follows the capillary instability of the non-electrified flow with thinning taking place and no incipient spike formation. This is expected physically due to the dominance of capillary forces over electric ones, at least initially. Breaking does not take place and eventually the interfacial maxima evolve sufficiently close to the electrode so that electric forces enter and indeed eventually dominate over the capillary forces (see Figure 3.6). This electrostatic mechanism violently attracts the interface towards the electrode through a spike formation. The time-scale of the touchdown is very fast and it is found that it can only be resolved accurately with very small time-steps and long computations (the number of modes also increases due to singularity formation). It is noted that the dynamics away from the spiking region behaves quasi-statically. In our simulations of this example, it is found that the singular event is initiated when the interface evolves such that $d - S_{max}$ is between

10^{-3} and 10^{-4}. At previous times and in particular when $10^{-3} < d - S_{max} < 10^{-1}$ in this example, the interface behaves as if it is almost stationary. The singularity formation takes place over a very fast time-scale when the quasi-static evolution brings the interface very close to the electrode. The left panel in Figures 3.6 depicts the interface at the final time and a detail of the liquid surface near the electrode. The right panel shows the evolution of $d - S_{max}$ and indicates the fast dynamics as the singularity is approached.

3.4.4 Finite-time Singularity and Self-similar Solutions

The numerical results suggest two canonical scenarios: (i) the liquid jet thins to form an electrically stabilized micro-thread that does not break, and (ii) a nonlinear evolution that causes the interface to touch the cylindrical electrode in finite time. This section is concerned with the analysis of the second regime which is generic in cases where the electrode is sufficiently close to the undisturbed interface ($\ln(d) < 1$ - see results of section 3.4.3), or if it is sufficiently far away ($\ln(d) > 1$) then the electric field strength measured by E_b is in the spike formation range as discussed in the results of section 3.4.2. Our analysis is started from the dimensionless system below

$$S_t + \frac{1}{2} S w_z + S_z w = 0, \tag{3.57}$$

$$3(S^2 w_z)_z + S_z - E_b \left(\frac{1}{\ln(d/S)} - \frac{1}{2(\ln(d/S))^2} \right)_z = 0. \tag{3.58}$$

Since we are interested in solutions that touch the cylindrical electrode $r = d$ after a finite time, $t = t_s$ say, we look for similarity solutions near the touchdown point $z = z_s$ and at times $\tau = t_s - t$ close to the singular event. Introducing a similarity variable $\xi = (z - z_s)/\tau^\beta$, where $\beta > 0$ is to be determined, the following expressions are used

$$S(z,t) = d - \tau^\alpha f(\xi), \qquad w = \tau^\gamma g(\xi), \tag{3.59}$$

where $\alpha > 0$ but γ can be negative. Equations (3.57)-(3.58) transform according to $\frac{\partial}{\partial z} \to \frac{1}{\tau^\beta}\frac{\partial}{\partial \xi}$ and $\frac{\partial}{\partial t} \to -\frac{\partial}{\partial \tau} + \frac{\beta\xi}{\tau}\frac{\partial}{\partial \xi}$, and a dominant balance of terms can be carried out for $\tau \ll 1$. To leading order a balance of terms $S_t \sim Sw_z$ in equation (3.57) and a balance between the term $3S^2 w_{zz}$ and $(E_b/2)\left(\frac{1}{(\ln(d/S))^2}\right)_z$ in equation (3.58) are found. Note that not all terms in the equations balance because $S \sim d$ to leading order, and hence $Sw_z \gg S_z w$, for example, with similar deductions holding for equation (3.58). Carrying out the dominant balances gives $\alpha - 1 = \gamma - \beta$ and $\gamma - 2\beta = -2\alpha - \beta$ from equations (3.57) and (3.58), respectively. Solving yields

$$\alpha = \frac{1}{3}, \qquad \gamma = \beta - \frac{2}{3}, \tag{3.60}$$

and the following equations for the scaling functions:

$$f - 3\beta\xi f' + \frac{3d}{2}g' = 0, \tag{3.61}$$

$$g'' + \frac{E_b}{6}\left(\frac{1}{f^2}\right)' = 0. \tag{3.62}$$

g can also be eliminated to get a single equation for f,

$$3\beta\xi f'' + f'\left(3\beta - 1 - \frac{dE_b}{2f^3}\right) = 0. \tag{3.63}$$

. The equations (3.61)-(3.63) need to be solved for $-\infty < \xi < \infty$ and the numerical results will be shown later. It is noted that it is sufficient to solve for $\xi > 0$ due to the symmetry $g(-\xi) = -g(\xi)$ and $f(-\xi) = f(\xi)$ (observed from our numerical simulations also). Here, we first combine local analysis and far field solutions to fix the parameter β. The behavior for large ξ is established as

$$f(\xi) \sim |\xi|^{1/(3\beta)}, \quad g'(\xi) \sim |\xi|^{-2/(3\beta)}, \quad |\xi| \to \infty. \tag{3.64}$$

The balance can be obtained from equation (3.61) and (3.62), which means the solution should be quasisteady far away (the quantity w_z behaves quasi-statically

there). It is concluded that f grows and g' decays for all β. The large ξ behavior of $g(\xi)$ from (3.64) is obtained by integration to find

$$g(\xi) \sim c_1 + c_2 \xi^{1-\frac{2}{3\beta}}, \tag{3.65}$$

where the constant c_1 is undetermined by this analysis and the constant c_2 is expressible in terms of $A > 0$ if we write $f(\xi) = A\xi^{\frac{1}{3\beta}} + O(\xi^{-\frac{2}{3\beta}})$. The initial value problem indicates that $c_1 \neq 0$ because the axial velocity w blows up away from the similarity region - see Figure 3.5 (b) for example. Using (3.64) and (3.65) into the ansatz (3.59) and expressing in terms of z provides the behavior of the outer solutions as the touchdown region is approached, i.e. as $z \to 0+$. The result is

$$S \sim d - Az^{\frac{1}{3\beta}}, \qquad w \sim c_1 \tau^{\beta-\frac{2}{3}} + c_2 z^{1-\frac{2}{3\beta}}, \qquad z \to 0+, \tag{3.66}$$

which shows the blowup of w away from the centerline.

On the other hand, f and g are expanded near $\xi = 0$, which is a singular point of equations (3.61)-(3.62), to perform a local analysis:

$$f \sim f_0 + \xi^2 f_2 + \xi^4 f_4 + ..., \tag{3.67}$$

$$g \sim \xi g_1 + \xi^3 g_3 + \xi^5 g_5 + ... \tag{3.68}$$

From equation (3.63) and (3.61), the expression of f_0 and g_1 in terms of d, E_b and β are obtained

$$f_0 = \left(\frac{dE_b}{12\beta - 2}\right)^{1/3}, \tag{3.69}$$

$$g_1 = \frac{-2}{3d} f_0. \tag{3.70}$$

It can be shown that the higher order coefficients $f_4, f_6, \ldots, g_3, g_5, \ldots$ can be expressed in terms of f_2 (and β). In particular

$$g_{2n+1} = \frac{2(6n\beta - 1)}{3d(2n+1)} f_{2n}, \qquad n = 0, 1, \ldots . \tag{3.71}$$

Next (3.62) is integrated once to obtain

$$g'(\xi) = \kappa - \frac{E_b}{6f^2}, \tag{3.72}$$

where κ is some constant independent of ξ. Setting $\xi = 0$ in equation (3.72) and using (3.69), (3.70) gives

$$\kappa = \frac{f_0}{d}(2\beta - 1). \tag{3.73}$$

In (3.72), it has been shown that, $g' \to 0$, $1/f^2 \to 0$ for $\xi \to \infty$ which immediately implies that $\kappa = 0$. Hence, $\beta = 1/2$. So the scalings become

$$d - S \sim \tau^{1/3}, \quad w \sim \tau^{-1/6}, \quad \xi = z/\tau^{1/2}, \tag{3.74}$$

and

$$S_z \sim w \sim \tau^{-1/6}, \qquad w_z \sim \tau^{-2/3} \tag{3.75}$$

follows. Hence, equation (3.63) becomes

$$\frac{3\xi}{2}f' - f + \frac{dE_b}{4f^2} = 0, \qquad \xi \geq 0, \tag{3.76}$$

which can be solved in closed form to give

$$f = \left(A^3\xi^2 + \frac{dE_b}{4}\right)^{1/3}, \qquad -\infty < \xi < \infty \tag{3.77}$$

with $A > 0$ a constant introduced earlier in our far-field analysis. The analogous expression for $g(\xi)$ can be written as the quadrature

$$g(\xi) = -\frac{E_b}{6}\int_0^{\xi} \frac{d\eta}{\left(A^3\eta^2 + \frac{E_b d}{4}\right)^{2/3}}, \tag{3.78}$$

with the odd parity properties providing $g(-\xi) = -g(\xi)$. Sample solutions are given in figures 3.7 for two different values of $A^3 = 0.6, 1$, $d = 2$ and $E_b = 2$. As can be

seen from (3.77) the effect of A can be removed by a horizontal re-scaling and that an increase in d or E_b or both leads to sharper profiles.

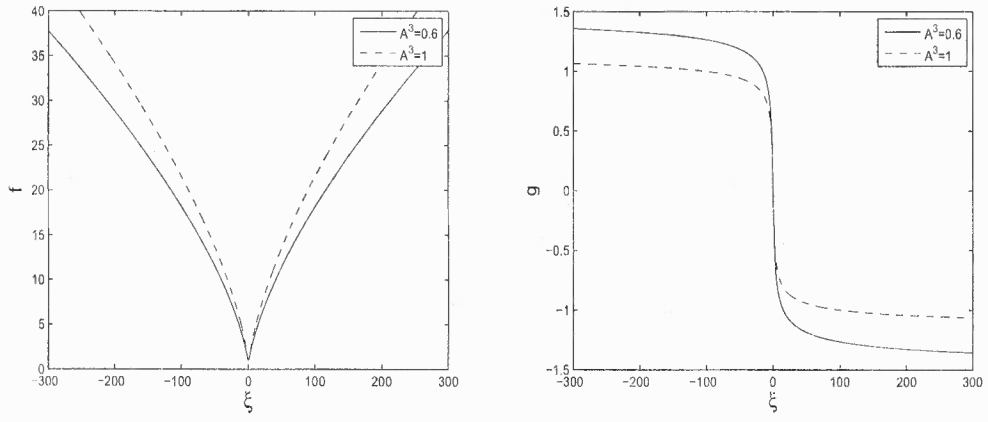

Figure 3.7 Typical similarity solutions $f(\xi)$ and $g(\xi)$ for $d = 2$, $E_b = 2$. The values of A are indicated on the figure.

Next we turn to the validation of the self-similar theory using the numerical solutions. If the functions are defined as $S_m(t) = \max_z (S(z,t))$ and $w_m(t) = \max_z (|w(z,t)|)$ then the theory predicts

$$d - S_m(t) \sim \left(\frac{E_b d}{4}\right)^{1/3} (t_s - t)^{1/3}, \qquad w_m(t) \sim (t_s - t)^{-1/6}. \tag{3.79}$$

In addition using the self-similar spatial scaling $\xi = z/(t_s - t)^{1/2}$ leads to the prediction:

$$\max_z (|S_z|) \sim w_m(t) \sim (t_s - t)^{-1/6}. \tag{3.80}$$

In Figure 3.8 we present numerical results as the singularity is approached. Panels (a) and (b) show, on log-log plots, the evolution of $d - S_m(t)$ and $w_m(t)$ with $(t_s - t)$, while panels (c) are log-log plots of the evolution of $\max_z (|S_z|)$ with $w_m(t)$. Panel (c) contains a collection of results for different values of the parameters d and E_b as shown in the figure, providing numerical confirmation that the asymptotic behavior is universal. To construct such plots the singular time t_s is required and is estimated as follows. Consider the evolution of $d - S_m(t)$ as in panel (d) of figure 3.5 and guided

by the predicted infinite slope of this function at $t = t_s$ we simply approximate t_s with the last computed time and exclude this data point from the constructions in the figures. Guided by the theoretical predictions (3.79) and (3.80) we superimpose dashed straight lines of slopes $1/3$ in panel (a), $-1/6$ in panel (b) and 1 in panels (c) respectively. It is seen that the predictions of the theory are supported very well by the numerical work. Additional evidence of the cusp-like behavior of $d - S(z,t)$ in the vicinity of the touchdown point can be inferred from the spectrum of $d - S(z,t)$ at times close to the singularity. According to the theory the spatial dependence of the singularity is given by $d - S \sim z^{2/3}$ as seen from (3.66) with $\beta = 1/2$. Using Watson's Lemma (see Bender & Orszag [7] for example) we deduce that for large k the spectrum should behave like $k^{-5/3}$. This agreement is shown in figure 3.9 where the evolution of the spectrum of $d - S(z,t)$ is depicted with the right panel showing the spectrum at the final time. A line of slope $-5/3$ is superimposed indicating good agreement and providing further support for the self-similar asymptotic structures.

Briefly speaking, we are interested in the spectrum of the function $d - S$,

$$F(k) = \int_{-\infty}^{\infty} e^{-ikx} f(x) dx, \tag{3.81}$$

and the asymptotic behavior for large k in the above integral. Assuming f is analytic (except perhaps at $x = 0$) and has an asymptotic approximation

$$f \sim a_0 x^{\alpha_0} + a_1 x^{\alpha_1} + \cdots, \qquad \text{as } x \to 0, \tag{3.82}$$

Watson's lemma enables us to integrate term by term to produce the asymptotic result,

$$\int_0^A e^{-zT} f(z) dz \sim \sum_0^n a_k T^{-\alpha_k - 1} \Gamma(\alpha_k + 1), \qquad \text{as } T \to \infty. \tag{3.83}$$

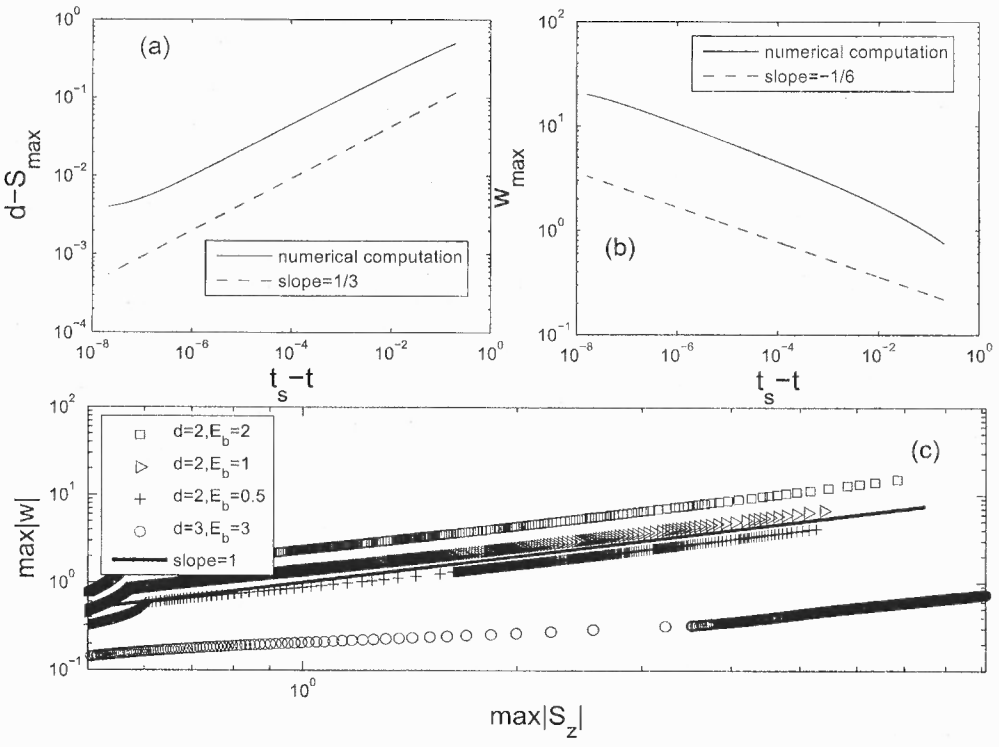

Figure 3.8 Comparison between numerical solutions and the self-similar theory for $d = 2$, $E_b = 2$, and an initial condition $S_0 = 1 - 0.5\cos(z)$. (a) Log-log plot of the evolution of $d - S_{max}$ with $t_s - t$; (b) log-log plot of the evolution of w_{max} with $t_s - t$; (c) log-log plot of the evolution of $\max|w|$ versus $\max|S_z|$ parameterized with time.

To apply this in our case, $T = ik$ and $z = x$ are chosen. Because x is proportional to ξ and in the far field $f \sim \xi^{2/3}$, $\alpha_0 = 2/3$ and $F(k) \sim k^{-5/3}$ follows. More details can be found in Hinch [23].

The numerical solutions of the initial boundary value problem can also be used to compare with the scaling functions $f(\xi)$ and $g(\xi)$. We focus on the case $d = 2, E_b = 2$ and numerical results for the initial condition $S_0 = 1 - 0.5\cos(z)$. The breakup time is estimated as described earlier and in this case $t_s = 0.1979805$ is found. The scaling functions are constructed from the computed solutions $S(z,t)$ and $w(z,t)$ using the ansatz (3.59) and $\xi = z/(t_s - t)^{1/2}$ for a sequence of times t near t_s. The results are given in Figure 3.10. It is seen that as $t \to t_s-$ there is

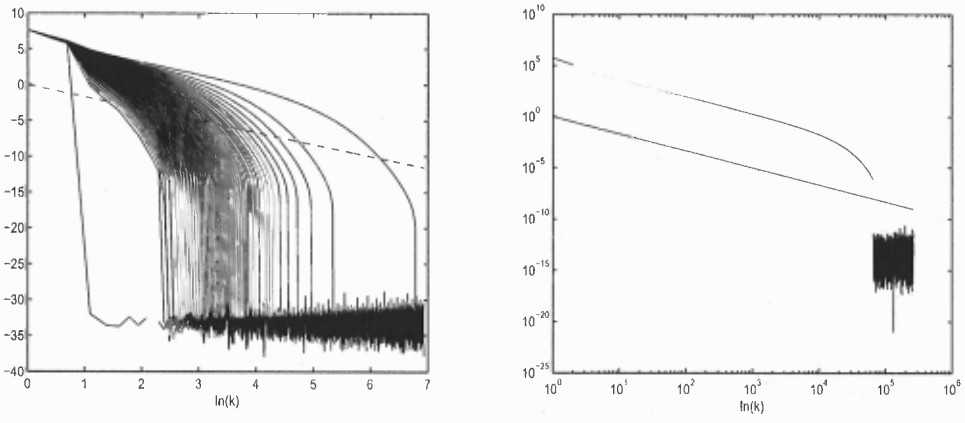

Figure 3.9 The evolution of the spectrum $|\hat{S}|^2$ of the interfacial shape indicating loss of analyticity as the singularity is approached. The right panel shows the spectrum at the final time along with the predicted line of slope $-5/3$ found from the self-similar analysis.

convergence to scaling functions in the vicinity of $\xi = 0$ which contain the features of those calculated using the similarity solutions (3.77) and (3.78). To make a direct comparison with the solutions (3.77)-(3.78) an estimate for the constant A is required from the constructed scaling functions of Figure 3.10 - note that in general A depends on initial conditions. This is achieved by using the large ξ form $f(\xi) \sim A\xi^{2/3}$ from (3.77) which in turn implies $\ln(f) \sim \ln(A) + (2/3)\ln(\xi)$ - a least squares fit from the data for $f(\xi)$ from Figure 3.10 at the last computed time yields the estimate $A^3 \approx 1.0343$. Figure 3.11 provides a comparison of the similarity solutions (3.77) and (3.78) calculated using $A^3 \approx 1.0343$, with the numerically computed scaling functions at the final time $t = 0.1979805$. Panel (c) of Figure 3.11 shows a detail of the region $\xi \leq 0$ - the solid line is the numerically computed scaling function $g(\xi)$ and the dotted line comes from the similarity solution (3.78). The horizontal dash-dotted lines denote the asymptotic values $g(\pm\infty)$ predicted by the theory once A is known. Once again agreement is very good and the self-similar structures derived analytically describe the final stages of the evolution very accurately.

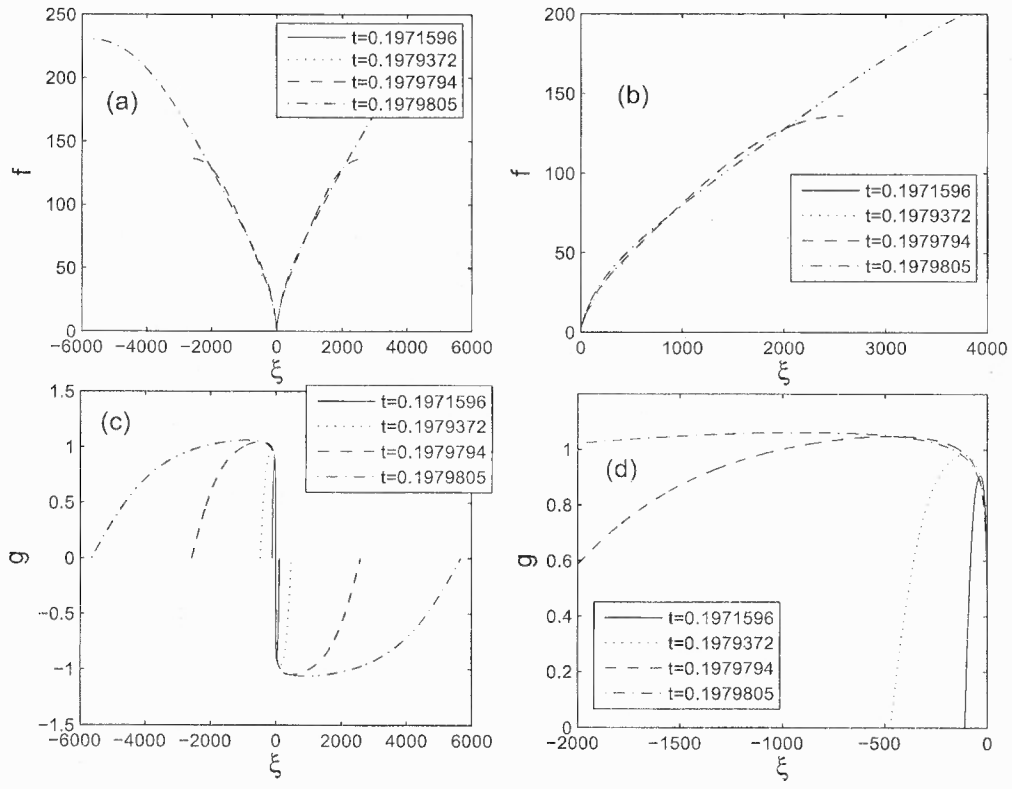

Figure 3.10 The scaling function $f(\xi)$ in panel (a) constructed from the computed solution $S(z,t)$ using (3.59) at times t indicated; $t_s \approx 0.197981$, $d = 2$, $E_b = 2$. Panel (b) shows detail in $\xi \geq 0$; The scaling function $g(\xi)$ in panel (c) constructed from the computed solution $w(z,t)$ using (3.59) at times t indicated; $t_s \approx 0.197981$, $d = 2$, $E_b = 2$. Panel (d) shows detail in $\xi \leq 0$.

Finally it should be pointed out that the surface tension at leading order is negligible compared with the electric force term. However, the axial curvature part, $\delta^2 S_{zz}$, blows up for the spike solutions. Then it is necessary to include this correction term in our model (see also Papageorgiou & Orellana [47]) so that the curvature reads $\kappa = 1/S - \delta^2 S_{zz}$. It is interesting to find that the scalings remain the same, since $S_{zz} \sim \tau^{-2/3}$ and is of the same order as the contribution from the electric force term $1/(S\ln(d/S))^2 \sim \tau^{-2/3}$ in equation (3.58). This self similar scalings are also observed in numerical simulations (not shown here) as expected, although the scaling functions in fact will be different.

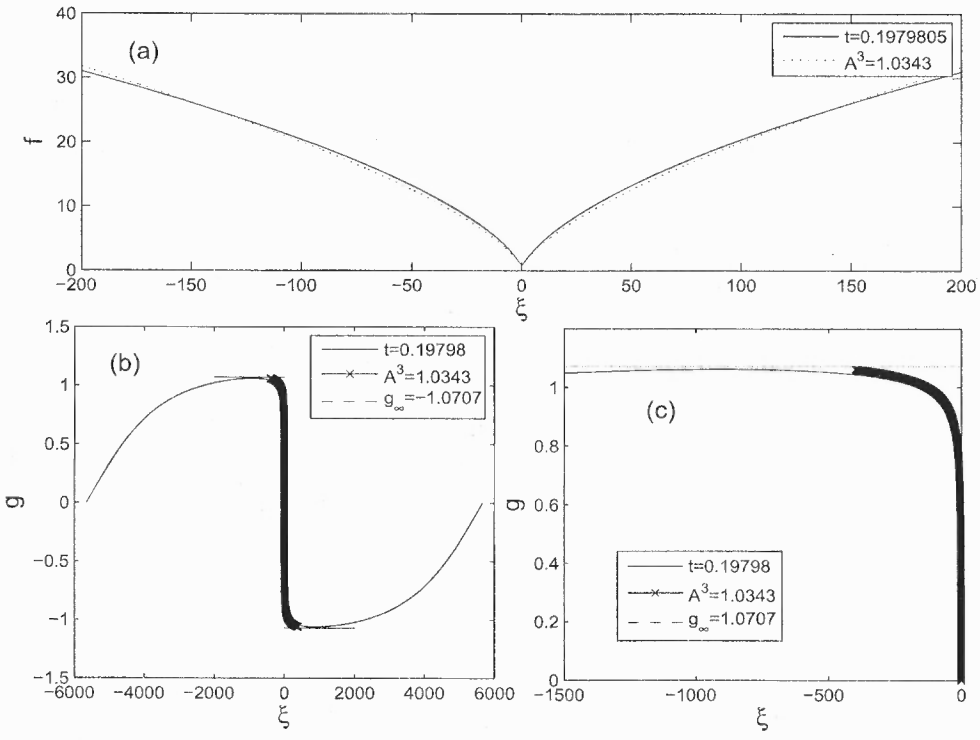

Figure 3.11 Comparison of scaling function $f(\xi)$ (dotted line) in panel (a) with the numerically constructed scaling function (solid line) for $d = 2, E_b = 2$. The value of $A^3 = 1.0343$ needed to obtain $f(\xi)$ was estimated by a least squares fit of the far-field of the computed solution. Panel (b) and (c) show comparing $g(\xi)$ (dashed line) with its numerically constructed analogue (solid line). The panel (c) is a detail of the region $\xi \leq 0$. The dotted lines represent the asymptotes $g(\pm\infty)$ provided by the theory.

3.4.5 Numerical Results for Navier-Stokes Jets and Scaling Arguments

In this section numerical results for Navier-Stokes jets are presented. The momentum equation (3.43) when inertia is included is rewritten as

$$\mathscr{R}(w_t + ww_z) = \frac{3\,(S^2 w_z)_z}{S^2} - \kappa_z + \frac{E_b}{2}\left(\frac{1}{S^2[\ln(d/S)]^2}\right)_z, \tag{3.84}$$

$$\kappa = \frac{1}{S} - \delta^2 S_{zz}, \tag{3.85}$$

where the S_{zz} term is asymptotically small but provides a higher order correction to the curvature and aids in the numerical simulations (e.g. Eggers & Dupont [17]).

In what follows $\mathscr{R}$ is taken to be one since it can be scaled out (e.g. Craster *et al.* [12]) and analogously to the Stokes jet case we will first consider $\ln d > 1$ followed by $\ln d < 1$. Before investigating the electrified jet, Figure 3.12 shows a numerical simulation for a non-electrified Navier-Stokes jet ($L = 5$). The code EPDCOL is used here. A satellite drop is formed in the middle of the domain and panels (b) and

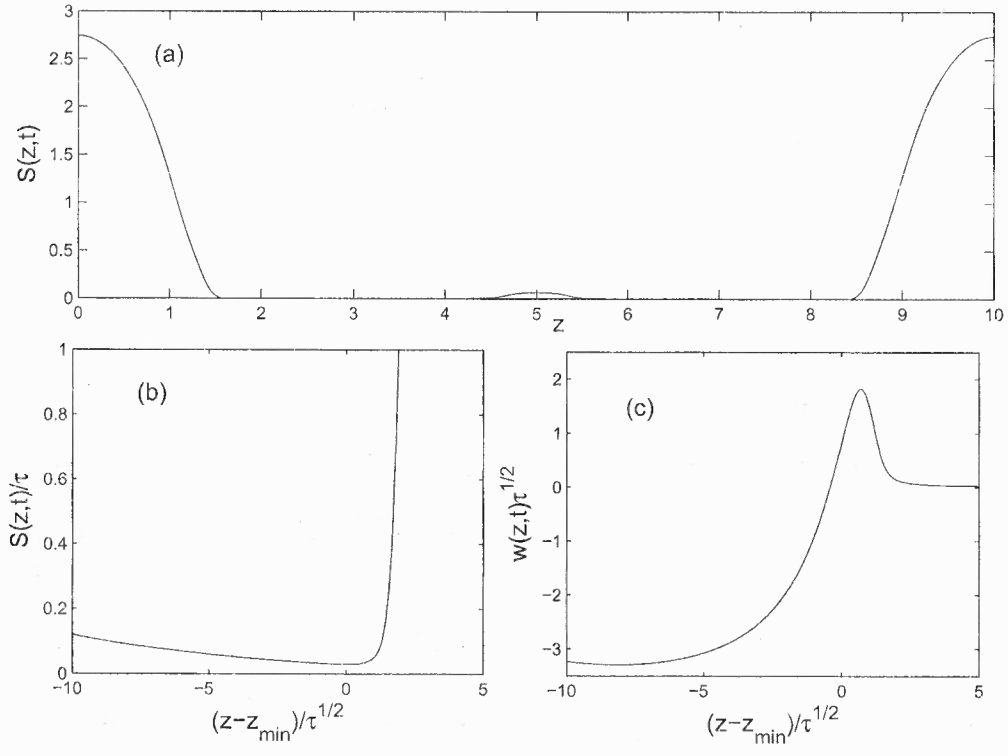

Figure 3.12 (a) The jet profile at pinching in the non-electrified case; panel (b) and (c) show the similarity solutions constructed from the final computed results. The initial conditions are $S(z,0) = 1 + 0.5\cos(\pi z/5)$ and $w(z,0) = 0$.

(c) in Figure 3.12 show the rescaled functions which follow the self-similar scalings derived by Eggers & Dupont [17], namely, $S(z,t) \sim \tau$ and $w(z,t) \sim \tau^{-1/2}$, where $\tau = t_s - t$ and t_s is the estimated breakup time. The scalings can be derived by considering the balance between the inertia, the capillary force and viscous force, i.e. $w_t \sim (1/S)_z \sim w_{zz}$ with the kinematic estimate $w \sim z/t$.

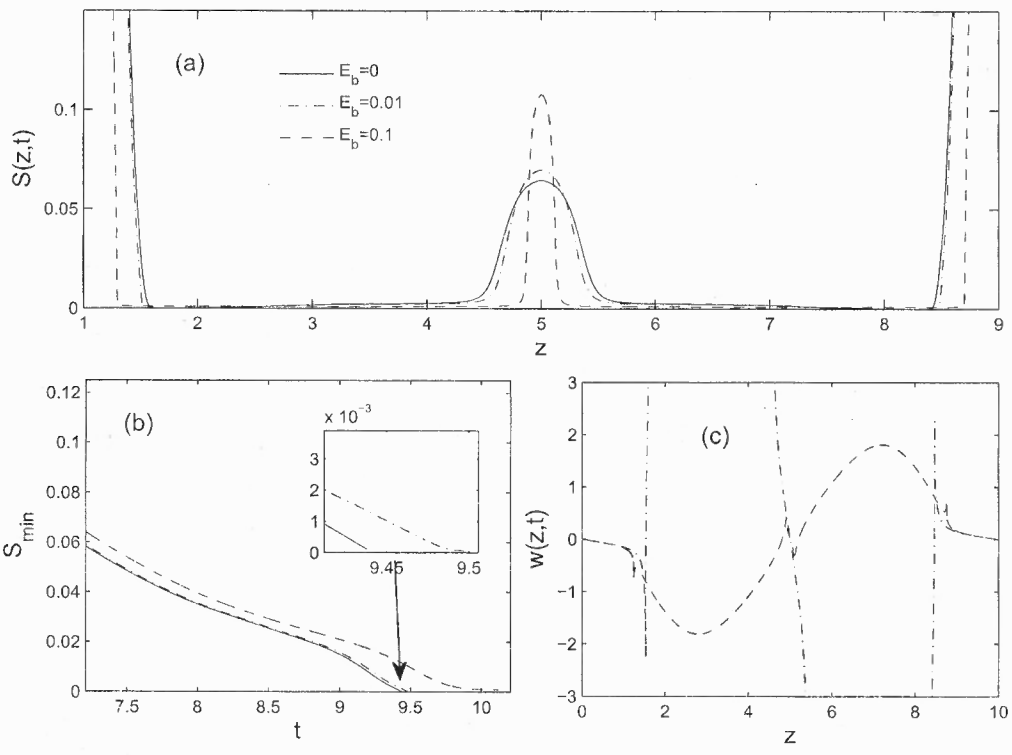

Figure 3.13 The jet profiles and satellite formation at final computed stage for $E_b = 0$, 0.01 and 0.1 respectively ($d = 5$ fixed) are shown in panel (a). With the same lines panel (b) shows the evolution of the S_{min} against time. Axial velocities in the case of $E_b = 0.01$ and $E_b = 0.1$ are presented in panel (c). The initial conditions are $S(z,0) = 1 + 0.5\cos(\pi z/5)$ and $w(z,0) = 0$.

The dynamics change dramatically when electric fields enter. In the Stokes limit it is found that the pinching solution is suppressed by the radial electric field. Electric stress competes with capillary stress and hence retards the breakup process and this also occurs in the presence of inertia. First $d = 5$ is taken which implies that the cylindrical electrode is initially far away from the fluid interface. In Figure 3.13, panel (a) outlines the final computed jet profiles for varying E_b as indicated in the figure. Panel (b) shows the corresponding evolution of S_{min} versus time. In contrast to the non-electrified case the thinning process slows down significantly due to the effect of electric stresses, at about $S_{min} \approx 5 \times 10^{-5}$ for $E_b = 0.01$ and $S_{min} \approx 9 \times 10^{-4}$ for $E_b = 0.1$. Panel (c) shows the axial velocity at $t = 9.498$ for $E_b = 0.01$ and

$t = 10.3$ for $E_b = 0.1$ compared to the breakup time $t = 9.4343$ for $E_b = 0$. The axial velocities decrease in magnitude (dash-dot line for $E_b = 0.01$ and dashed line for $E_b = 0.1$) when E_b increases as seen in panel (c) of Figure 3.13 and local cusps are observed corresponding to the points where a steep jet profile is found. Finally the interface meets with infinite slope singularity (see dashed line result in panel (a) of Figure 3.13) before it pinches. This result is consistent with the results that we show for the Stokes jets. The contribution of individual terms on the right hand side of (3.84) is investigated numerically at the final computed stage ($S_{min} \approx 0.001$) for $E_b = 0.1$ and $d = 5$ in Figure 3.14. Different terms are defined as follows,

$$x_1 = \frac{S_z}{S^2}, \quad x_2 = E_b \frac{S_z(\ln(d/S) - 1)}{S^3 \ln^3(d/S)},$$
$$x_3 = w_{zz} + \frac{2S_z w_z}{S}, \quad x_4 = 3x_3 + x_1 - x_2. \tag{3.86}$$

x_1 represents the capillary contribution to the momentum and x_2, x_3 stand for electric and viscous effect respectively. x_4 represents the total contribution at the right hand side of (3.84). It turns out that as the jet thins the gradient of the viscous, capillary effect and electric forces are comparable. Therefore it is conjectured that the local dynamics may be influenced significantly by the electric field and this is left for future work of simulation of the full problem.

Compared to the pinching solution presented by Collins *et al.* [11], for both Stokes and Navier-Stokes jets, the low order system derived in the long-wave approximation does not lead to the pinching phenomenon. The discrepancy occurs partially due to the long-wave description of the axial velocity, $w = w(z,t)$, which in the charged case depends on the radial variable as well (see Collins *et al.* [11]). However, the local behavior is expected to be captured. For Stokes jet in Figure 3.1, charge accumulates in the middle portion of the thin thread and acts against the surface tension, hence stabilizes the jet and a quasisteady microthread is formed between main drops. Before the neck reduces to zero the infinite-slope singularity is encountered first

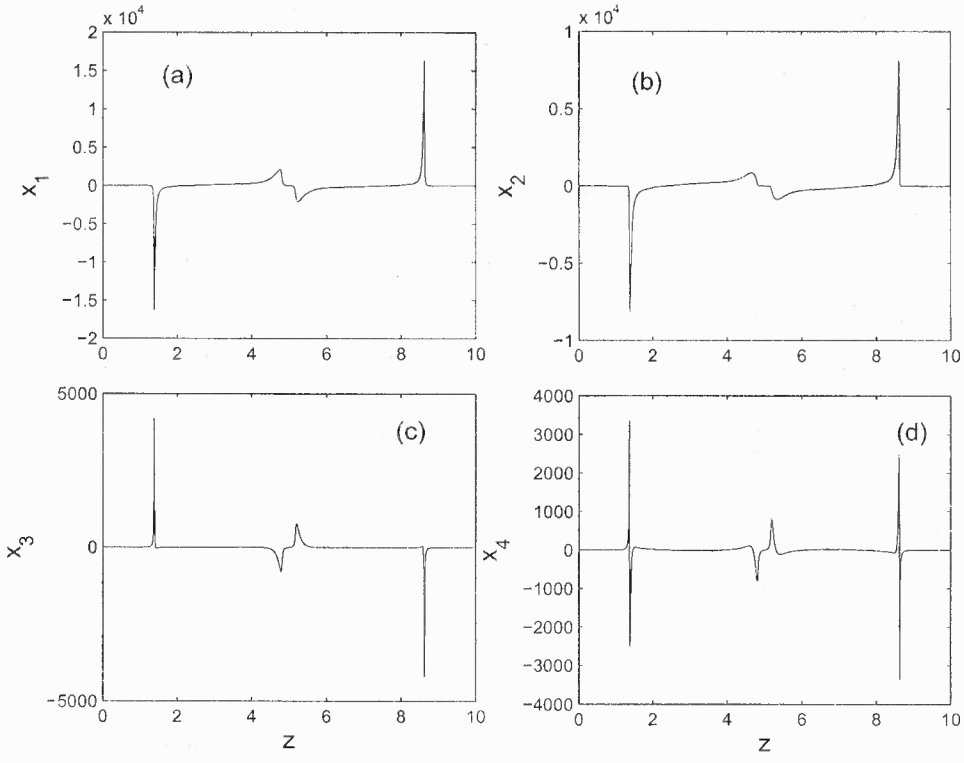

Figure 3.14 Panel (a)-(d) show different terms x_1-x_4 respectively.

at which point charge concentration also blows up since charge tends to accumulate at high-curvature regions where the long-wave model breaks down. This implies that if pinching happens, then it can be asymmetric as confirmed by the numerical simulations of Collins *et al.* [11]. It is also seen in our simulations of Stokes jets that the axial velocity decreases slowly as the microthread forms, which indicates that inertial effects are small; a similar phenomenon is desired in the long-wave simulation of electrified Navier-Stokes jet and this is confirmed by the results of Figure 3.13.

Similar to the electrified Stokes jet, (3.47) indicates that $\ln d < 1$ causes the jet to be linearly unstable. Here the neglect of inertia near the touchdown region is valid. Characterize the local dynamic response by a Reynolds number $R_e = \rho w z/\mu$ following the idea of Lister & Stone [36]. Initially the Reynolds number is expressed

as $R_{e0} = \rho\gamma a/\mu^2$. Near touchdown z and w evolve as

$$z \sim a(\frac{\tau}{t_0})^{\beta}, \qquad w \sim \frac{\gamma}{\mu}(\frac{\tau}{t_0})^{\nu}. \tag{3.87}$$

Substituting these into the expression for the Reynolds number and using the scalings we derived in the Stokes the limit gives,

$$R_e = \frac{\rho}{\mu}\frac{\gamma a}{\mu}(\frac{\tau}{t_0})^{\nu+\beta} = R_{e0}(\frac{\tau}{t_0})^{1/3}. \tag{3.88}$$

Hence $R_e \to 0$ as $\tau \to 0$, and it is concluded that we can approximate the motion by ignoring the inertia near touchdown. The inertia only affects the flow outside the touchdown region.

Next, if it is assumed that touching of the outer electrode takes place in finite time, then we proceed as before with a balance of terms in order to determine a possible self-similar structure. Assuming an ansatz as in (3.59), it is found that the kinematic condition (3.40) allows a leading order balance of terms $S_t \sim Sw_z$ if $\alpha - 1 = \gamma - \beta$, as before. In (3.84) balance the inertial terms on the left hand side with the second derivative of the axial velocity and electric field terms on the right hand side to obtain $\gamma - 1 = -2\gamma + \beta - 2$ and $\gamma - 1 = \gamma - 2\beta$. Combining these findings leads to the same scalings we found for the Stokes limit case, i.e. $\alpha = 1/3, \gamma = -1/6, \beta = 1/2$. For completeness, the similarity equations are given for the inertial analogues of the scaling functions $f(\xi)$ and $g(\xi)$ introduced by (3.59) - these equations are not pursued further in the present work:

$$f - \frac{3}{2}\xi f' + \frac{3d}{2}g' = 0, \tag{3.89}$$

$$\lambda(\frac{1}{6}g + \frac{\xi}{2}g') = 3g'' + \frac{E_b}{2}(\frac{1}{f^2})'. \tag{3.90}$$

In Figure 3.15, sample numerical results of the initial value problem are shown to support our analysis. Panel (a) shows the spike shape of liquid jet near touchdown. The axial velocity is plotted in panel (b) showing a shock discontinuity in the vicinity

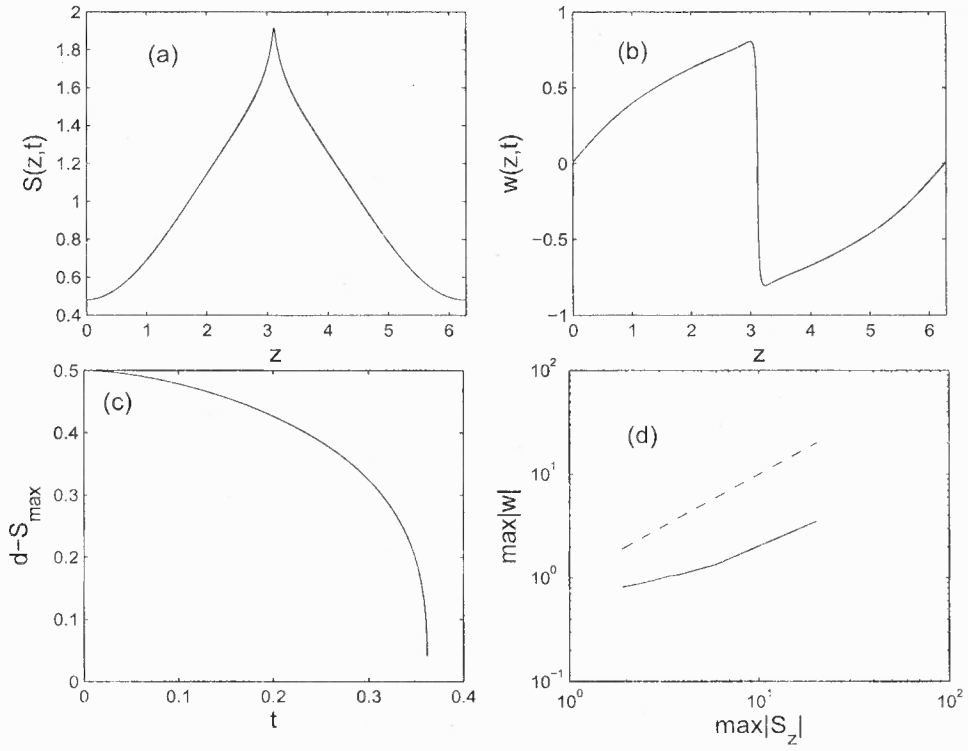

Figure 3.15 (a) Jet shape and (b) the corresponding axial velocity solution in the case $d = 2$, $E_b = 2$. (c) Evolution of $d - S_{max}$. (d) Log-log plot of evolution of $\max|w|$ versus $\max|S_z|$ parameterized by time. Initial condition is $S(z,0) = 1 + 0.5\cos(z)$ and $w(z,0) = 0$.

of S_{max} similar to the Stokes case. Rapid touchdown dynamics under the effect of the electric field is confirmed by the evolution of $d - S_{max}$ in panel (c). As time tends to the singular time, the scalings follow our theoretical prediction in panel (d) of Figure 3.15. The dashed line is from the theory and of unit slope, while the solid line represents the nonlinear computational result.

CHAPTER 4

ELECTRIFIED INVISCID THREADS

In this chapter the viscosity of the core jet is neglected and the annular fluid is taken to be passive. Hence the governing equations become the Euler equation. For convenience the velocity potential ϕ is introduced in the rest of this chapter, which satisfies $\mathbf{u} = \nabla\phi$ and $\nabla^2\phi = 0$ in the fluid domain. The boundary conditions are the kinematic and dynamic boundary condition (Bernoulli equation) on the jet surface. The electric potential ϕ^e as usual satisfies $\nabla^2\phi^e = 0$ in the annular region. The full nonlinear dynamics was investigated by Setiawan & Heister [59] by a boundary element method and axisymmetric traveling wave solutions were computed by Grandison *et al.* [21]. Our interest in the present work lies in the stabilizing effect of the electric fields in the long-wave limit as shown below. Therefore a slender jet will be considered for the rest of this chapter.

4.1 Linear Stability

Before deriving the evolution equations, the linear stability is reviewed. As mentioned in Chapter (3), the linear dispersion relation of the full problem is given by

$$\omega^2 = \frac{k^2\left(1 - k^2 - \frac{E_b}{\ln^2 d}\left(1 + k\frac{K_0(kd)I_1(k) + I_0(kd)K_1(k)}{I_0(k)K_0(kd) - I_0(kd)K_0(k)}\right)\right)}{kI_0(k)/I_1(k)}, \tag{4.1}$$

and in the long-wave limit ($k \to 0$)

$$\omega^2(k) \sim \frac{k^2}{2}(1 - \alpha), \tag{4.2}$$

where $\alpha = E_b(\ln d - 1)/(\ln d)^3$. The stabilizing effect of the electric fields is observed when α is sufficiently large ($\alpha > 1$) as illustrated in Figure (4.1) which shows the growth rate curves of the full dispersion relation (4.1). As the electric field increases,

a stability window emerges for small k (right panel in Figure (4.1)). Our aim is to describe the nonlinear dynamics in the presence of such dispersive effects and to derive Kortweg-de Vries type equations for this physical problem.

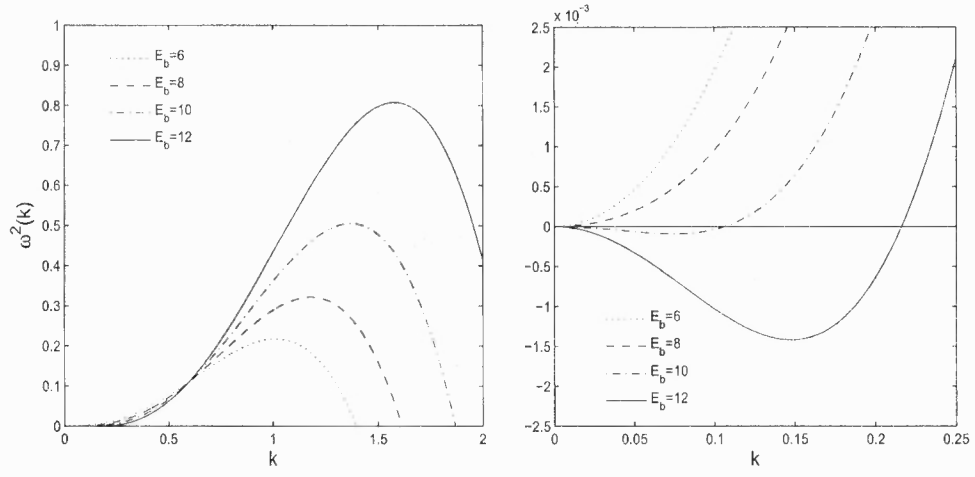

Figure 4.1 Growth rate for various E_b produced by linear theory with $d = 10$ fixed. Right panel shows the long-wave portion under the same condition.

4.2 Long-wave Equations

Since viscosity is absent, the characteristic capillary time scale that is used here is different from the one in Chapter 2 and is given by $t_0 = (\rho a^3/\gamma)^{1/2}$. Introduce a slenderness parameter $\epsilon = a/l$, where a and l are radial and axial length scales respectively. Given a typical velocity $W_0 = l/t_0$, and electric potential V_0, dimensionless variables are defined as follows:

$$z = lz', \quad r = ar', \quad \phi = W_0 l\phi', \quad p = \frac{\gamma}{\epsilon^2 a}p', \quad t = t_0 t', \quad \phi^e = V_0\phi'^e. \tag{4.3}$$

Then the dimensionless governing equations and boundary conditions (dropping the primes) are given by the Laplace equation for the velocity potential ϕ in the jet region

$$\phi_{rr} + \frac{1}{r}\phi_r + \epsilon^2\phi_{zz} = 0, \tag{4.4}$$

the kinematic condition on $r = S(z,t)$,

$$\phi_r = \epsilon^2(S_t + \phi_z S_z), \tag{4.5}$$

and the Bernoulli equation on $r = S(z,t)$,

$$\phi_t + \frac{1}{(1+\epsilon^2 S_z^2)^{3/2}}\left(\frac{1+\epsilon^2 S_z^2}{S} - \epsilon^2 S_{zz}\right) - \frac{E_b}{2}\left(\phi_n^e\right)^2 + \frac{1}{2}\left(\frac{\phi_r^2}{\epsilon^2} + \phi_z^2\right) = 1 - \frac{E_b}{2\ln^2 d}. \tag{4.6}$$

In (4.6) $\phi_n^e = n \cdot \nabla\phi^e$ and $(E_b/2)\phi_n^2$ represents the electric force and the constant on the right hand side is obtained from the unperturbed state. The electric potential in the annular region $(S < r < d)$ is governed by

$$\phi_{rr}^e + \frac{1}{r}\phi_r^e + \epsilon^2\phi_{zz}^e = 0, \tag{4.7}$$

with boundary conditions

$$\phi^e(r = S(z,t)) = 0, \quad \phi^e(r = d) = 1. \tag{4.8}$$

4.3 Weakly Nonlinear Analysis: Electro-capillary Solitary Waves

In addition to the long-wave assumption, the interface is assumed to deform to heights δ, that is we write $S = 1 + \delta\eta(z,t)$ where $\delta(\epsilon) \ll \epsilon$. The derivation here is similar to the derivation of the Korteweg-de Vries equation in shallow water theory (see Johnson [28]), but in a completely different physical problem and geometry.

The electric potential has the asymptotic representation in the annular region

$$\phi^e \sim \phi_0^e + \epsilon^2\phi_1^e + \epsilon^4\phi_2^e + \cdots. \tag{4.9}$$

From the Bernoulli equation (4.6) it is seen that $\left(\phi_n^e\right)^2$ is central in the derivation. Given the normal vector on the interface $\mathbf{n} = (1, -\epsilon S_z)/(1+\epsilon^2 S_z^2)^{1/2}$ the normal

derivative of the electric potential at the interface can be written as

$$\phi_n^e = \frac{\phi_r^e - \epsilon^2 \phi_z^e S_z}{(1+\epsilon^2 S_z^2)^{1/2}} \sim \phi_{0r}^e + \epsilon^2 \phi_{1r}^e - \epsilon^2 \delta \eta_z \phi_{0z}^e + \cdots .$$

$$\Rightarrow (\phi_n^e)^2 = (\phi_{0r}^e)^2 + 2\epsilon^2 \phi_{0r}^e \phi_{1r}^e + \cdots . \tag{4.10}$$

It will be shown later that higher order terms in (4.10) are not necessary in our derivation. First, the $O(1)$ equation is considered

$$\frac{1}{r}(\phi_{0r}^e)_r = 0, \tag{4.11}$$

which, subject to the boundary conditions $\phi_0^e(r=d)=1$ and $\phi_0^e(r=S(z,t))=0$, gives

$$\phi_0^e = \frac{\ln(r/S(z,t))}{\ln(d/S(z,t))}. \tag{4.12}$$

Substituting $S = 1 + \delta\eta(z,t)$ into ϕ_{0r}^e yields

$$\begin{aligned}
\phi_{0r}^e &= \frac{1}{(1+\delta\eta)(\ln d - \ln(1+\delta\eta))} \\
&\sim (1 - \delta\eta + \delta^2\eta^2 + \cdots)\frac{1}{\ln d - \delta\eta + \delta^2\eta^2/2 + \cdots} \\
&\sim \frac{1}{\ln d}(1 - \delta\eta + \delta^2\eta^2 + \cdots)\left(1 + \frac{\delta}{\ln d}(\eta - \frac{\delta}{2}\eta^2) + \frac{\delta^2}{\ln^2 d}\eta^2 + \cdots\right) \\
&\sim \frac{1}{\ln d}\left(1 + \frac{1-\ln d}{\ln d}\delta\eta + \frac{2 - 3\ln d + 2\ln^2 d}{2\ln^2 d}\delta^2\eta^2 + \cdots\right)
\end{aligned}$$

and

$$(\phi_{0r}^e)^2 \sim \frac{1}{\ln^2 d}\left(1 + 2\frac{1-\ln d}{\ln d}\delta\eta + \frac{3 - 5\ln d + 3\ln^2 d}{\ln^2 d}\delta^2\eta^2 + \cdots\right). \tag{4.13}$$

It is also necessary to proceed to the next order ($O(\epsilon^2)$) problem which is

$$\frac{1}{r}(\phi_{1r}^e)_r + \phi_{0zz}^e = 0, \tag{4.14}$$

with boundary conditions $\phi_1^e(r=d) = \phi_1^e(r=S) = 0$. Setting $\Phi(z) = \left(\frac{S_z}{S\ln^2(d/S)}\right)_z$ yields the following expression for ϕ_{0zz}^e

$$\phi_{0zz}^e = \ln(r/d)\Phi(z). \tag{4.15}$$

On substitution of (4.15) into (4.14) and integration with respect to r yields

$$\phi_1^e = -\frac{r^2}{4}\ln(r/d)\Phi + \frac{r^2}{4}\Phi + A\ln r + B, \tag{4.16}$$

where $A = A(z,t)$ and $B = B(z,t)$.

Applying the boundary conditions, it can be found that

$$\begin{aligned}
&\frac{d^2}{4}\Phi + A\ln d + B = 0,\\
&-\frac{S^2}{4}\ln(S/d)\Phi + \frac{S^2}{4}\Phi + A\ln S + B = 0,
\end{aligned}$$

which gives

$$A(z,t) = \left(\frac{S^2}{4} + \frac{d^2 - S^2}{4\ln(S/d)}\right)\Phi(z,t). \tag{4.17}$$

Since only the derivative with respect to r is required to leading order, $B(z,t)$ is not needed in the sequel. It follows from (4.16) that

$$\phi_{1r}^e = \left(-\frac{r}{2}\ln(r/d) + \frac{r}{4}\right)\Phi + \frac{A}{r}, \tag{4.18}$$

and on the interface

$$\begin{aligned}
\phi_{1r}^e|_{r=1+\delta\eta} &\sim \left(\frac{\ln d}{2} + \frac{1}{4}\right)\frac{\delta\eta_{zz}}{\ln^2 d} + \frac{\ln d - d^2 + 1}{4\ln^3 d}\delta\eta_{zz} + \cdots\\
&= \frac{2\ln^2 d + 2\ln d - d^2 + 1}{4\ln^3 d}\delta\eta_{zz} + O(\delta^2).
\end{aligned} \tag{4.19}$$

Substituting (4.13) and (4.19) into (4.10) yields

$$(\phi_n^e)^2 \sim \frac{1}{\ln^2 d}\left(1+2\frac{1-\ln d}{\ln d}\delta\eta+\frac{3-5\ln d+3\ln^2 d}{\ln^2 d}\delta^2\eta^2+\cdots\right)+$$
$$2\epsilon^2\frac{1}{\ln d}\left(1+\frac{1-\ln d}{\ln d}\delta\eta\right)\left(\frac{2\ln^2 d+2\ln d-d^2+1}{2\ln^3 d}\delta\eta_{zz}\right)+\cdots,$$

which simplifies to

$$(\phi_n^e)^2 = \frac{1}{\ln^2 d}+2\frac{1-\ln d}{\ln^3 d}\delta\eta+\frac{3-5\ln d+3\ln^2 d}{\ln^4 d}\delta^2\eta^2$$
$$+\frac{2\ln^2 d+2\ln d-d^2+1}{2\ln^4 d}\epsilon^2\delta\eta_{zz}+O(\epsilon^2\delta^2). \tag{4.20}$$

Having the information of the electric forces (4.20), we now turn to the fluid mechanics problem and assume that the velocity potential has the appropriate expansion

$$\phi \sim \delta(\phi_0+\epsilon^2\phi_1+\epsilon^4\phi_2+\cdots). \tag{4.21}$$

The solutions for the first few orders are obtained by inserting (4.21) into (4.4) and solving sequentially to find

$$\phi_0 = \phi_0(z,t), \tag{4.22}$$
$$\phi_1 = -\frac{r^2}{4}\phi_{0zz}+\theta_1(z,t), \tag{4.23}$$
$$\phi_2 = \frac{r^4}{48}\phi_{0zzzz}-\frac{r^2}{4}\theta_{1zz}+\theta_2(z,t), \tag{4.24}$$

where $\theta_1(z,t)$ and $\theta_2(z,t)$ are unknown functions.

Next the boundary conditions (kinematic and Bernoulli condition) are considered on the jet surface $S = 1+\delta\eta(z,t)$. The kinematic boundary condition (4.5) by substituting (4.22)-(4.24) becomes

$$\delta\left(\frac{-1}{2}(1+\delta\eta)\phi_{0zz}+\epsilon^2\left(\frac{1}{12}(1+\delta\eta)^3\phi_{0zzzz}-\frac{1}{2}(1+\delta\eta)\theta_{1zz}\right)+\cdots\right)$$
$$=\delta\eta_t+\delta^2\eta_z\left(\phi_{0z}+\epsilon^2\left(-\frac{1}{4}(1+\delta\eta)^2\phi_{0zzz}+\theta_{1z}\right)+\cdots\right). \tag{4.25}$$

The Bernoulli equation (4.6) becomes

$$\delta\phi_{0t}+\epsilon^2\delta\left(-\frac{1}{4}(1+\delta\eta)^2\phi_{0zzt}+\theta_{1t}\right)+\cdots+\frac{\epsilon^2\delta^2}{8}(1+\delta\eta)^2\phi_{0zz}^2+\cdots$$
$$+\frac{\delta^2}{2}\left(\phi_{0z}+\epsilon^2\left(-\frac{1}{4}(1+\delta\eta)^2\phi_{0zzz}+\theta_{1z}\right)+\cdots\right)^2+\cdots=$$
$$1-(1-\delta\eta)(1-\frac{\epsilon^2\delta^2}{2}\eta_z^2)+\epsilon^2\delta\eta_{zz}+\cdots+\frac{E_b}{2}\left((\phi_n^e)^2-\frac{1}{\ln^2 d}\right) \tag{4.26}$$

Balancing the leading order in (4.25) and (4.26) gives

$$-\frac{\phi_{0zz}}{2}\sim\eta_t, \tag{4.27}$$
$$\phi_{0t}\sim(1+\frac{E_b}{\ln^3 d}(1-\ln d))\eta, \tag{4.28}$$

which yields the following equation for η at the leading order

$$\eta_{tt}=-\frac{1}{2}(1+\frac{E_b}{\ln^3 d}(1-\ln d))\eta_{zz}. \tag{4.29}$$

Clearly, if the coefficient in front of η_{zz} in (4.29) is positive, a wave equation follows which is consistent with our analysis in section 4.1. Hereafter we consider this case and set

$$c^2=-\frac{1}{2}(1+\frac{E_b}{\ln^3 d}(1-\ln d)). \tag{4.30}$$

Next the kinematic and Bernoulli equations are rewritten by truncating terms up to $O(\delta\epsilon^2)$ and $O(\delta^2)$ in (4.25) and (4.26). Eliminating δ, equation (4.25) becomes

$$-\frac{1}{2}\phi_{0zz}-\frac{1}{2}\delta\eta\phi_{0zz}+\frac{\epsilon^2}{12}\phi_{0zzzz}-\frac{\epsilon^2}{2}\theta_{1zz}=\eta_t+\delta\eta_z\phi_{0z}. \tag{4.31}$$

Meanwhile, (4.26) gives

$$\phi_{0t}-\frac{\epsilon^2}{4}\phi_{0zzt}+\epsilon^2\theta_{1t}+\frac{\delta}{2}\phi_{0z}^2=\eta+\epsilon^2\eta_{zz}+$$
$$E_b\left(\frac{1-\ln d}{\ln^3 d}\eta+\frac{3\ln^2 d-5\ln d+3}{2\ln^4 d}\delta\eta^2+\frac{\epsilon^2}{4\ln^4 d}(2\ln^2 d+2\ln d+1-d^2)\eta_{zz}\right) \tag{4.32}$$

Let $x = z - ct$ and look for traveling wave solutions by applying the transformations

$$\frac{\partial}{\partial t} \to \frac{\partial}{\partial t} - c\frac{\partial}{\partial x}, \quad \frac{\partial}{\partial z} \to \frac{\partial}{\partial x}, \tag{4.33}$$

where c is given by (4.30). Then (4.31) becomes

$$-\frac{1}{2}\phi_{0xx} - \frac{1}{2}\delta\eta\phi_{0xx} + \frac{\epsilon^2}{12}\phi_{0xxxx} - \frac{\epsilon^2}{2}\theta_{1xx} = \eta_t - c\eta_x + \delta\eta_x\phi_{0x}, \tag{4.34}$$

and (4.32) becomes

$$\phi_{0t} - c\phi_{0x} - \frac{\epsilon^2}{4}(\phi_{0xxt} - c\phi_{0xxx}) + \epsilon^2(\theta_{1t} - c\theta_{1x}) + \frac{\delta}{2}\phi_{0x}^2 = \eta + \epsilon^2\eta_{xx} +$$
$$E_b\left(\frac{1-\ln d}{\ln^3 d}\eta + \frac{3\ln^2 d - 5\ln d + 3}{2\ln^4 d}\delta\eta^2 + \frac{\epsilon^2}{4\ln^4 d}(2\ln^2 d + 2\ln d + 1 - d^2)\eta_{xx}\right). \tag{4.35}$$

Differentiating (4.35) with respect to x and changing time scale by $\partial_t \to \triangle\partial_\tau$ yields

$$\triangle\phi_{0\tau x} - c\phi_{0xx} + \frac{\epsilon^2}{4}c\phi_{0xxxx} - \epsilon^2 c\theta_{1xx} + \delta\phi_{0x}\phi_{0xx} + \cdots \sim \eta_x + \epsilon^2\eta_{xxx} +$$
$$E_b\left(\frac{1-\ln d}{\ln^3 d}\eta_x + \frac{3\ln^2 d - 5\ln d + 3}{\ln^4 d}\delta\eta\eta_x + \frac{\epsilon^2}{4\ln^4 d}(2\ln^2 d + 2\ln d + 1 - d^2)\eta_{xxx}\right). \tag{4.36}$$

Next (4.34) is multiplied by $2c$ and becomes

$$-c\phi_{0xx} - c\delta\eta\phi_{0xx} + c\frac{\epsilon^2}{6}\phi_{0xxxx} - c\epsilon^2\theta_{1xx} = \triangle 2c\eta_\tau - 2c^2\eta_x + 2c\delta\eta_x\phi_{0x}. \tag{4.37}$$

Then the subtraction of (4.37) from (4.36) gives

$$\triangle\phi_{0\tau x} + \frac{\epsilon^2}{4}c\phi_{0xxxx} + \delta\phi_{0x}\phi_{0xx} + c\delta\eta\phi_{0xx} - c\frac{\epsilon^2}{6}\phi_{0xxxx} + \cdots$$
$$\sim \epsilon^2\eta_{xxx} - \triangle 2c\eta_\tau - 2c\delta\eta_x\phi_{0x} + \cdots +$$
$$E_b\left(\frac{3\ln^2 d - 5\ln d + 3}{\ln^4 d}\delta\eta\eta_x + \frac{\epsilon^2}{4\ln^4 d}(2\ln^2 d + 2\ln d + 1 - d^2)\eta_{xxx}\right). \tag{4.38}$$

Set $\triangle = \delta = \epsilon^2$ and notice that $\phi_{0x} \sim 2c\eta$ follows from the leading order balance $\phi_{0t} - c\phi_{0x} \sim -2c^2\eta$. On substitution of this relation into (4.38) yields a final evolution equation for surface elevation η

$$4c\eta_\tau + (10c^2 - P_1)\eta\eta_x + \left(\frac{c^2}{6} - 1 - P_2\right)\eta_{xxx} = 0, \tag{4.39}$$

where P_1 and P_2 are defined as

$$P_1 = \frac{3\ln^2 d - 5\ln d + 3}{\ln^4 d} E_b, \tag{4.40}$$

$$P_2 = \frac{2\ln^2 d + 2\ln d + 1 - d^2}{4\ln^4 d} E_b. \tag{4.41}$$

The properties of equation (4.39) are analogous to the classical Kortweg-de Vries equation. Existence of depression or and elevation traveling wave solutions depend on the sign of the second and third terms. For example, when $10c^2 - P_1 > 0$, $c^2/6 - 1 - P_2 > 0$ gives elevation waves while $c^2/6 - 1 - P_2 < 0$ gives depression waves.

Finally a large gap ($d \to \infty$) limit is considered. In order to maintain the electric field term, $\phi^e \sim \ln r$ at infinity and hence E_b can be expanded as

$$E_b \sim (\ln d)^2 E_0 + \cdots, \text{ as } d \to \infty. \tag{4.42}$$

It follows that

$$c^2 \sim -\frac{1}{2}(1 - E_0) + \cdots, \quad P_1 \sim 3 + \cdots, \quad P_2 \sim \frac{1}{2} + \cdots. \tag{4.43}$$

In this case the evolution equation of elevation traveling waves for an inviscid charged jet is obtained to leading order

$$4c_0\eta_\tau + (10c_0^2 - 3)\eta\eta_x + \left(\frac{c_0^2}{6} - \frac{3}{2}\right)\eta_{xxx} = 0, \tag{4.44}$$

where $c_0^2 = -\frac{1}{2}(1 - E_0)$ provided $E_0 > 1$.

CHAPTER 5

ELECTRIFIED CORE-ANNULAR FLOWS

In this section the core-annular flow inside a cylindrical tube is considered. For simplicity set $\chi = 1$ so that the densities of the two fluids are equal and buoyancy effects are negligible. The relevant physical quantities are discussed in Chapter 2 and in this chapter results in the low Reynolds number case are presented.

5.1 Governing Equations

The governing equations (nondimensionalized as in Chapter 2) for the fluids are then given by Stokes equations and the continuity equations in the core (fluid 1) and annular (fluid 2) regions respectively.

$$-\nabla p + \lambda_i \nabla^2 \boldsymbol{u} = 0, \quad \nabla \cdot \boldsymbol{u} = 0, \tag{5.1}$$

where $\boldsymbol{u} = (u_r, u_z)$ is the dimensionless fluid velocity field, p is the pressure and $\lambda_1 = 1, \lambda_2 = \lambda = \mu_2/\mu_1$ is the viscosity ratio of the two immiscible fluids. On the tube wall, the no-slip and no-penetration boundary conditions require that

$$u_r = 0, \quad u_z = 0. \tag{5.2}$$

In the annular region, the electric potential (denoted by ϕ) satisfies Laplace's equation,

$$\phi_{rr} + \frac{1}{r}\phi_r + \phi_{zz} = 0, \tag{5.3}$$

with boundary conditions $\phi(r = d) = 1$ on the wall and $\phi(r = S) = 0$ at the interface; as in previous chapters, the core fluid is taken to be a perfect conductor.

In addition, at the fluid interface, $r = S(z, t)$, the kinematic condition reads

$$u_r = S_t + u_z S_z, \tag{5.4}$$

and tangential and normal stress balances

$$[\boldsymbol{t} \cdot \boldsymbol{T} \cdot \boldsymbol{n}] = 0, \tag{5.5}$$

$$[\boldsymbol{n} \cdot \boldsymbol{T} \cdot \boldsymbol{n}] = \frac{E_b}{2}\phi_n^2 - \kappa, \tag{5.6}$$

where $\boldsymbol{t}$ and $\boldsymbol{n}$ are unit tangential and normal vector respectively on the surface, with $E_b = \frac{\epsilon_p V_0^2}{\gamma a}$ the electric Taylor number, κ the curvature at the interface, $\boldsymbol{T}$ the Newtonian stress tensor defined in Chapter 2.

5.2 Linear Stability

From the governing equations, it is easy to find the steady solutions for a perfectly cylindrical interface:

$$u_r = u_z = 0, \qquad p = 1 - \frac{E_b}{2(\ln d)^2}, \qquad S = 1, \qquad \phi = \frac{\ln r}{\ln d}. \tag{5.7}$$

Imposing a small perturbation to the unperturbed state, the radial position of the interface is described as

$$r = 1 + \epsilon\eta + c.c., \tag{5.8}$$

where ϵ is a small dimensionless coefficient, $\eta = A_1 \exp(ikz + \omega t)$ is the wave form of the perturbation and A_1 is the complex amplitude. Taking advantage of the axisymmetry of the flow, the velocities are expressed in terms of the Stokes stream function ψ_j, where $j = 1, 2$ for the inner and outer fluid respectively. The axial and radial components of the perturbation velocity are given by

$$u_{z,j} = \frac{1}{r}\frac{\partial \psi_j}{\partial r}, \quad u_{r,j} = -\frac{1}{r}\frac{\partial \psi_j}{\partial z}. \tag{5.9}$$

Using (5.9) and solving for the vorticity transport equation for the axisymmetric flow, the following equation for ψ is obtained

$$\boldsymbol{E}^2\boldsymbol{E}^2\psi_j = 0, \tag{5.10}$$

where $\boldsymbol{E}^2$ is a second order differential operator given as

$$\boldsymbol{E}^2 = \frac{\partial^2}{\partial z^2} + \frac{\partial^2}{\partial r^2} - \frac{1}{r}\frac{\partial}{\partial r}. \tag{5.11}$$

The general solution can then be written as

$$\begin{aligned}\psi_j(r,t) &= \phi_j(r)\exp(\mathrm{ikz} + \omega \mathrm{t}) \\ &= r(E_{1,j}I_1(kr) + F_{1,j}K_1(kr) + \\ &E_{2,j}rI_0(kr) + F_{2,j}rK_0(kr))\exp(\imath \mathrm{kz} + \omega \mathrm{t}),\end{aligned} \tag{5.12}$$

where $E_{l,j}$ and $F_{l,j}$ are unknown coefficients.

Next kinematic and dynamic boundary conditions at the interface are considered. Using (5.12), the continuity of velocities at the interface requires

$$\phi_1 = \phi_2, \quad \phi_1' = \phi_2', \quad \text{at } r = 1. \tag{5.13}$$

Meanwhile, the boundary conditions on the tube wall require that

$$\phi_2(d) = 0, \quad \phi_2'(d) = 0. \tag{5.14}$$

Finally, substituting (5.12) into the linearized version of the tangential stress balance

$$\left(\frac{\partial u_{z,1}}{\partial r} + \frac{\partial u_{r,1}}{\partial z}\right) - \lambda\left(\frac{\partial u_{z,2}}{\partial r} + \frac{\partial u_{r,2}}{\partial z}\right) = 0, \tag{5.15}$$

and normal stress balance

$$-p_1 + 2\frac{\partial u_{r,1}}{\partial r} + p_2 - 2\frac{\partial u_{r,2}}{\partial r} = \epsilon A_1(1 - k^2 - \triangle p^e)exp(ikz + \omega t), \tag{5.16}$$

where

$$\triangle p^e = \frac{E_b}{\ln^2(d)}\left(1 + k\frac{K_0(kd)I_1(k) + I_0(kd)K_1(k)}{I_0(k)K_0(kd) - I_0(kd)K_0(k)}\right), \tag{5.17}$$

yields a homogeneous system for the growth rate ω, with

$$\boldsymbol{M}\boldsymbol{w} = 0 \tag{5.18}$$

where $\boldsymbol{w}$ is a vector of unknown coefficients defined as

$$\boldsymbol{w}^T = [E_{1,1}, E_{2,1}, F_{1,1}, F_{2,1}, E_{1,2}, E_{2,2}, F_{1,2}, F_{2,2}] \tag{5.19}$$

and the coefficient matrix is given by

$$\mathbf{M} = \begin{bmatrix} I_1(k) & I_0(k) & -I_1(k) & -I_0(k) & -K_1(k) & -K_0(k) \\ kI_0(k) & L_1 & -kI_0(k) & L_2 & kK_0(k) & L_3 \\ 0 & 0 & I_1(kd) & dI_0(kd) & K_1(kd) & dK_0(kd) \\ 0 & 0 & kI_0(kd) & L_4 & -kK_0(kd) & L_5 \\ S_1 & S_2 & S_3 & S_4 & S_5 & S_6 \\ T_1 & T_2 & T_3 & T_4 & T_5 & T_6 \end{bmatrix} \tag{5.20}$$

The expressions for the components of matrix M are given out in Appendix A. Details of similar derivations can also be found in Tomotika [64] and Kwak & Pozrikidis [31].

5.2.1 Long-wave Expansion

In the limit $k \longrightarrow 0$ in (5.20), the following growth rate can be obtained explicitly

$$\omega = k^2(1-\alpha)F \tag{5.21}$$

with

$$\alpha = \frac{\ln d - 1}{(\ln d)^3} E_b, \tag{5.22}$$

$$F = \frac{1}{16\lambda}\left[(1-d^2)^2\left(1 - \frac{(1-d^2)^2}{(d^4+\lambda-1)}\right) - 4\ln(1/d) - 2d^2 + 2\right]. \tag{5.23}$$

Equation (5.21) is valid for λ away from extreme values. This result is consistent with the one in Georgiou *et al.* [19] for the uncharged case. Clearly it is seen from (5.21) that the way the electric fields affect the stability does not change much compared with the single jet case in Chapter 3 because of the assumption of the

perfect conductor which implies the coupling between the electrostatics and fluid dynamics only occurs through the normal stress balances.

5.2.2 Linear Stability of The Core-annular Flow

In the absence of electric fields, the core thread is subject to Rayleigh instability when the wavenumber of the perturbation is below a critical value $k = 1$ in dimensionless terms. The effect of external viscous fluids is shown in Figure 5.1 that the most unstable mode is shifted from $k = 0$ to a finite value. The dotted lines in panel (a)

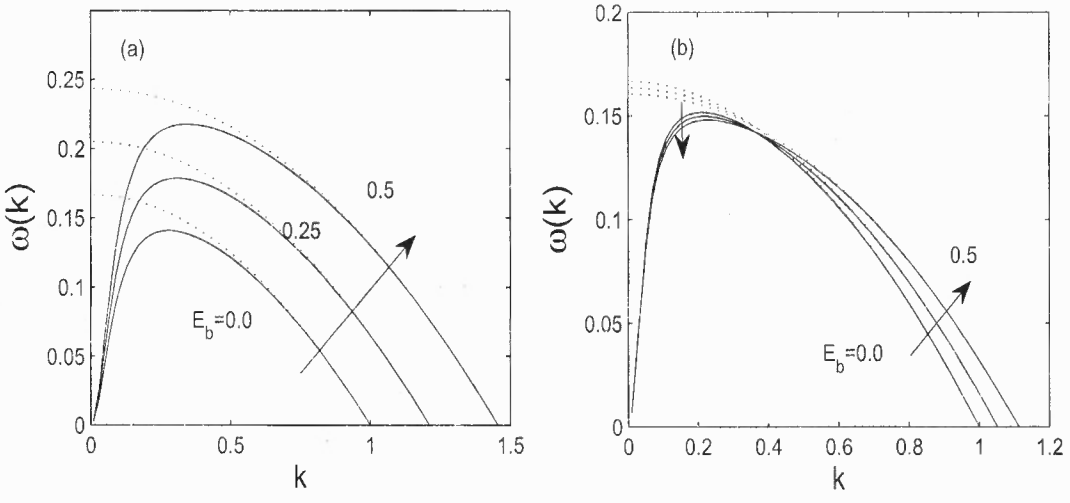

Figure 5.1 Growth rate for varying E_b from 0 to 0.5 indicated by the arrows in the figure with (a) d=2.5 and (b) d=3.0. Dotted lines represent the result for $\lambda = 0$ and solid lines for $\lambda = 0.001$.

and (b) in Figure 5.1 represent the results for a single Stokes jet which agree with the results in Wang *et al.* [66]. The parameter d is chosen to be $d = 2.5$ in panel (a) and $d = 3$ in panel (b) which is based on the linear results discussed in section 3.3 of Chapter 3. Namely, $d < e \approx 2.7183$ gives instability irrespective of E_b while stabilizing effect takes place when $d > e$ in the long wave limit. Therefore increasing E_b enhances instability for both $\lambda = 0$ and $\lambda = 0.001$ as observed in panel (a) in

Figure 5.1. Panel (b) shows that the long waves are stabilizing as E_b increases and at the same time the short waves tend to be unstable as indicated by the arrows.

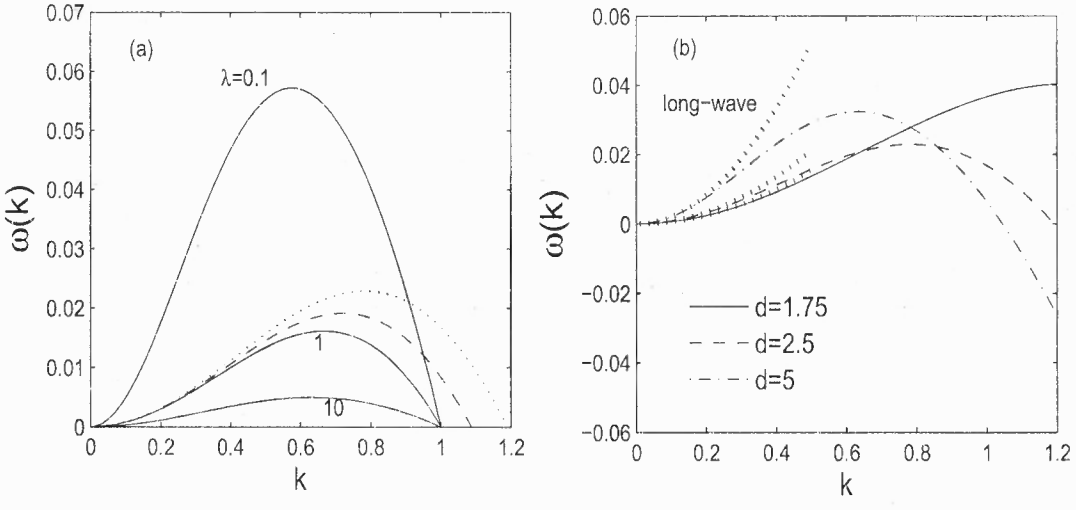

Figure 5.2 (a) Growth rate for $E_b = 0.0$, 0.25 and 0.5 shown by solid line, dashed line and dotted line respectively, for fixed $d = 2.5$ and $\lambda = 1$. In addition, the growth rate is also plotted for $\lambda = 0.1$ and 10 in the non-electrified case as indicated in the figure. Panel (b) shows for fixed $E_b = 0.5$ and $\lambda = 1$ the dependence of growth rate on the parameter d. Long wave predictions are shown in dotted lines in the small k portion.

Figure 5.2 investigates the effect of different parameters (λ, d and E_b) on the growth rate. In panel (a) of Figure 5.2 the solid lines represent the growth rate for $d = 2.5$ and $E_b = 0$ with varying λ, which shows that the presence of a more viscous annular fluid reduces the growth rate significantly. As shown later, λ also significantly affects satellite formation in the nonlinear regime. By increasing E_b, the same panel shows that the range of unstable wavenumbers is extended. Dashed and dotted lines correspond to $E_b = 0.25$ and $E_b = 0.5$ respectively. Panel (b) in Figure 5.2 shows the dependence of the growth rate on d for fixed $E_b = 0.5$ and $\lambda = 1$; $d = 1.75$ gives a wide range of unstable modes in which case the electrode tube wall is relatively close to the fluid interface. Physically, the small annulus ensures an intense field that gives a fairly big electric force on the interface. The surface charge accumulates there and

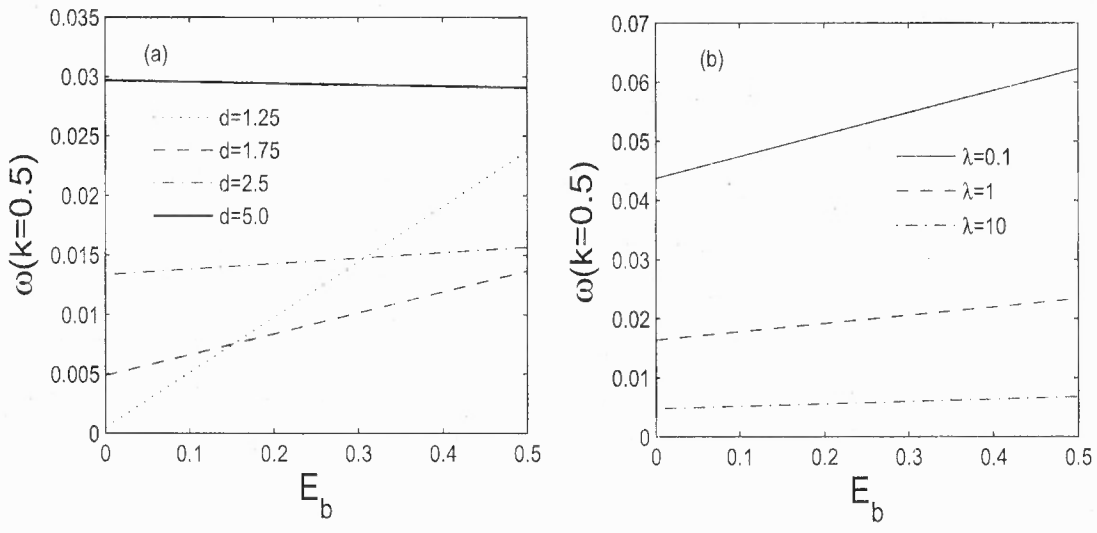

Figure 5.3 Effect of the electric fields on the growth rate of a wave with $k = 0.5$ for (a) varying d and fixed $\lambda = 1$ and (b) varying λ and fixed $d = 2.8$.

affects the fluid flow actively. In addition, long wave results obtained from (5.21) are also verified in panel (b) and shown as dotted lines with the same parameters. For the small wavenumber portion the agreement is excellent. A typical example showing detail in the effect of tube radius and viscosity ratio is plotted in Figure 5.3 for $\lambda = 1$. Wavenumber $k = 0.5$ is picked and panel (a) shows that the growth rate is increasing by increasing electric field strength for $d = 1.25$, 1.75 and 2.5, while a stabilizing effect for $d = 5$ is observed by the decreasing curve for the growth rate. Panel (b) in Figure 5.3 shows that growth rate is increasing faster when a less viscous fluid is present in the annulus. This agrees with the results in panel (a) of Figure 5.2.

5.3 Thin Annulus Limit

When the thickness of an annular layer is sufficiently small, the motion may be described under the approximation of local flow irrespective of the effect of core fluid, as long as the viscosity ratio is comparable (see Hammond [22]). Again we will assume the core fluid (U, W, P) is perfectly conducting and the annulus (u, w, p) is a dielectric.

Following Hammond [22], set $\epsilon = (d-1)/d$ and assume $\epsilon \ll 1$ and $\epsilon\lambda \ll 1$. In this limit the variable $y = (d-r)/\epsilon$ is used so that the interface may be described by

$$y = \frac{d - S(z,t)}{\epsilon} = h(z,t), \tag{5.24}$$

with $h = O(1)$. The velocity and pressure fields in the film region are written as

$$w = \epsilon^3 w'(y,z), \quad u = \epsilon^4 u'(y,z), \quad p = -1 + \epsilon p'(y,z), \tag{5.25}$$

and in the core

$$W = \epsilon^3 W', \quad U = \epsilon^3 U', \quad P = \epsilon^3 P'. \tag{5.26}$$

Substituting (5.25) into the Stokes equations in the film region yields

$$u_{rr} + \frac{1}{r}u_r - \frac{1}{r^2}u = p_r \quad \Rightarrow \quad p'_y = O(\epsilon^2), \tag{5.27}$$

$$\frac{1}{r}(rw_r)_r + w_{zz} = 0 \quad \Rightarrow \quad p'_z - w_{yy} = O(\epsilon), \tag{5.28}$$

$$\frac{1}{r}(ru)_r + w_z = 0 \quad \Rightarrow \quad w'_z - u'_y = O(\epsilon). \tag{5.29}$$

No slip on the tube wall requires that

$$w'(0,z) = u'(0,z) = 0, \tag{5.30}$$

and the continuity of velocities at the interface requires

$$W'(d - \epsilon h(z,t), z) - w'(h(z,t),z) = 0, \quad U'(d - \epsilon h(z,t), z) = \epsilon u'(h(z,t),z), \tag{5.31}$$

which approximately are

$$W'(1,z) - w'(h(z,t),z) = O(\epsilon), \quad U'(1,z) = O(\epsilon). \tag{5.32}$$

The tangential stress balance at the interface reads

$$(1-\epsilon^2 h_z^2)(-\epsilon^2 w_y' + \epsilon^4 u_z') + 2\epsilon h_z(\epsilon^3 u_y' - \epsilon^3 w_z') \\ = \lambda\epsilon^3\left[(1-\epsilon^2 h_z^2)(W_r' + U_z') + 2\epsilon(U_r' - W_z')\right], \tag{5.33}$$

from which the equation for w' becomes

$$w_y'(h,z) = O(\epsilon\lambda). \tag{5.34}$$

The normal stress balance becomes

$$\epsilon^3\lambda(-(1+\epsilon^2 h_z^2)P' + 2(U_r' + \epsilon h_z(U_z + W_r) + \epsilon^2 h_z^2 W_z')) \\ -(1+\epsilon^2 h_z^2)(1-\epsilon p' + \triangle p^e) - (-2\epsilon^3 u_y' + 2\epsilon^5 h_z(u_z' - w_y') + 2\epsilon^5 h_z^2 w_z') \\ = -(1+\epsilon^2 h_z^2)^{1/2}((1-\epsilon h)^{-1} + (1+\epsilon^2 h_z^2)^{-1} h_{zz}) \tag{5.35}$$

from which we obtain

$$p'(h(z,t),z) = -(h + h_{zz} - \frac{\triangle p^e}{\epsilon}) + O(\epsilon^2, \epsilon^2\lambda), \tag{5.36}$$

where $\triangle p^e$ is the electric force that is fixed later. The set of equations and boundary conditions suggest that we pose asymptotic expansions $\varphi \sim \varphi_0 + \epsilon\varphi_{10} + \epsilon\lambda\varphi_{01}$, where φ is some function (h, w, p), even though only the zeroth-order terms will be considered here. Dropping primes, using (5.27), (5.28) subject to (5.30) and (5.34) the solution for w at leading order is obtained as

$$w_0 = \frac{p_{0z}}{2}(y^2 - 2hy). \tag{5.37}$$

Similarly equation (5.29) implies

$$u_0 = \frac{p_{0zz}}{2}(\frac{y^3}{3} - hy^2) - \frac{y^2}{2} p_{0z} h_z. \tag{5.38}$$

Formally it is seen that the core fluid does not enter into the leading order balances in this case. In addition, combining the kinematic condition

$$h_t = -w_0 h_z - u_0, \tag{5.39}$$

with the solutions (5.37), (5.38), yields

$$h_t = \frac{1}{3}(p_{0z} h^3)_z. \tag{5.40}$$

The $\triangle p^e$ in (5.36) is obtained by solving Laplace's equation for the electric potential in the film region

$$\phi_{rr} + \frac{\phi_r}{r} + \phi_{zz} = 0, \quad \Rightarrow \phi_{yy} = O(\epsilon), \tag{5.41}$$

which at the leading order gives

$$\phi = \frac{h - y}{h}. \tag{5.42}$$

Then

$$\triangle p^e \approx \frac{E_b}{2}\phi_r^2 = \frac{E_b}{2\epsilon^2}\phi_y^2 = \frac{E_b}{2\epsilon^2 h^2}. \tag{5.43}$$

In order to retain electrostatic effects the canonical limit $E_b = \epsilon^3 \beta$, with $\beta = O(1)$, so that (5.36) becomes

$$p_0 = -h - h_{zz} + \frac{\beta}{2h^2}, \tag{5.44}$$

which on substitution into (5.40) yields the thin-film type equation

$$h_t = -\frac{1}{3}\left(h^3(h_z + h_{zzz}) + \beta h_z\right)_z. \tag{5.45}$$

When $\beta = 0$ electric fields are absent and the resulting equation has been studied by Hammond [22], Lister *et al.* [35], who find that touchdown does not occur in finite time. Our results show next, however, that the inclusion of electrostatic effects induces finite time touchdown.

5.3.1 A Note on Non-axisymmetric Modes

Here consider non-axisymmetric modes and the θ dependence is assumed $g(r,\theta,z,t) = \hat{g}(r)e^{\omega t+i(m\theta+kz)}$, where g denotes a function under consideration at least in linear theory. Due to the assumption of perfect conductor-core, it has already been mentioned that the electric force term will only enter into the normal stress balances, since the interface has uniform potential. The full curvature now has the form

$$\kappa = \frac{1}{\sqrt{1+S_z^2+S_\theta^2/S^2}}\frac{1}{S} - \left(\frac{S_z}{\sqrt{1+S_z^2+S_\theta^2/S^2}}\right)_z - \left(\frac{S_\theta}{S\sqrt{1+S_z^2+S_\theta^2/S^2}}\right)_\theta \frac{1}{S}. \tag{5.46}$$

Again for the thin annulus case, $d = 1+\epsilon$, and in the leading order, the following equation can be obtained in a similar way as described above

$$h_t = -\frac{1}{3}\left(h^3(h_z + h_{zzz} + h_{z\theta\theta}) + \beta h_z\right)_z. \tag{5.47}$$

The growth rate follows immediately

$$\omega(k) = -\frac{k^2}{3}(k^2+m^2-1-\beta), \tag{5.48}$$

compared with the one from the axisymmetric case

$$\omega(k) = -\frac{k^2}{3}(k^2-1-\beta). \tag{5.49}$$

Therefore it is seen that the growth rate from (5.48) is smaller than the one from (5.49) for $m > 0$ which means the axisymmetric perturbation in thin annulus limit is dominant over the non-axisymmetric perturbation. Hence attention will only be paid to the axisymmetric case for the rest of this thesis.

5.3.2 Self-similar Solution

When $\beta \neq 0$, it is interesting to find that the thin film equation assumes a solution of the following form

$$h(z,t) = (t_s - t)^{1/3} f\left(\frac{z}{(t_s - t)^{1/2}}\right), \tag{5.50}$$

where t_s is the breakup time. The scalings can be obtained by balancing $h_t \sim (h^3 h_{zzz})_z \sim \beta h_{zz}$. Notice that without the electric force term, Hammond [22] shows numerical evidence of an infinite time singularity. More resolved and extensive numerical work by Lister *et al.* [35] reveal that touchdown does not occur but instead a multiscale in time drop sliding and thinning takes place. In the electrified problem, however, we have a finite-time singularity which will be confirmed by the numerical simulations showed later.

5.3.3 Numerical Results

In order to solve equation (5.45), EPDCOL is used here, which utilizes finite element collocation in space and Gear's method in time (see also section 3.4.5 in Chapter 3). A typical run is presented in Figure 5.4. Panel (a) shows the shape of the film at the breakup time with an initial condition $h(z,0) = 1 + 0.5\cos(2\pi/Lz)$. To verify the self-similar behavior close to breakup, panel (b) illustrates that the evolution of h_{min} follows the self-similar scaling through a log-log plot, where t_s is estimated from simulation and the solid line has slope $-1/3$. Additional evidence is shown in panel (c) of Figure 5.4, which indicates $h_{zz} \sim h_z^4$ (solid line is of slope one) since $h_z \sim \tau^{-1/6}$ and $h_{zz} \sim \tau^{-2/3}$. It can be seen from the figure that the simulation struggles when the spike forms since only equal-spacing grids are used here. An adaptive-grid code may resolve the singular solution better, but we do not pursue this in the present study.

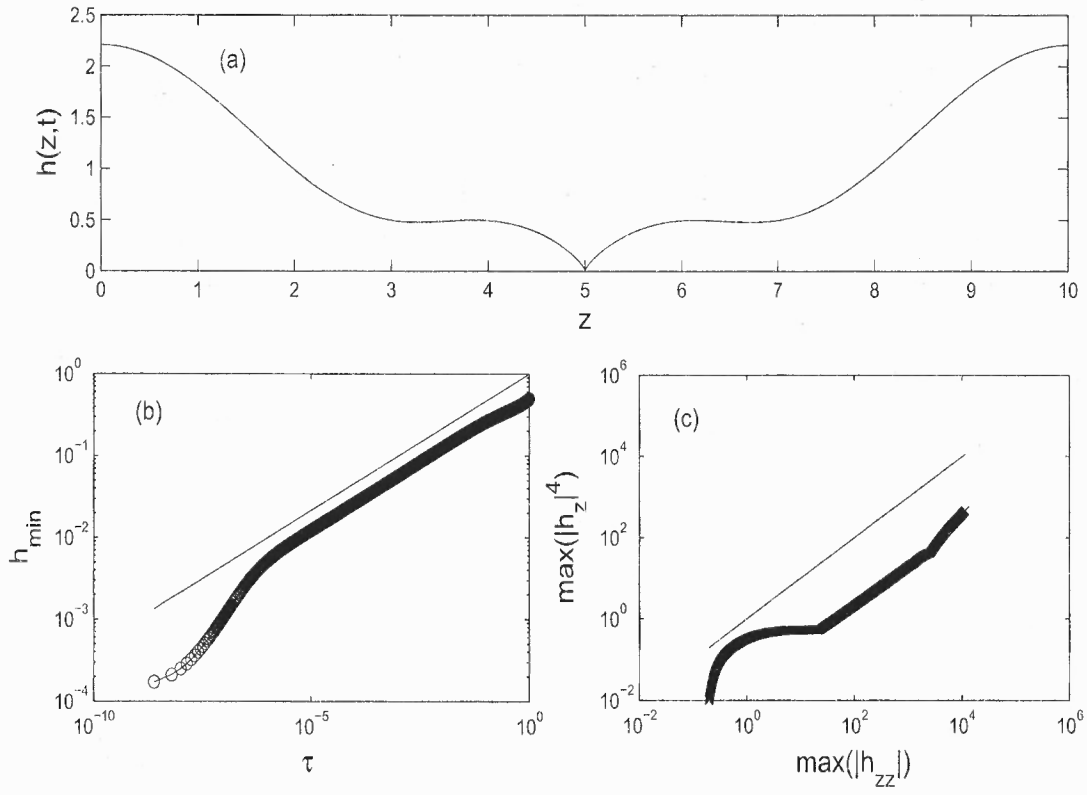

Figure 5.4 (a) Solution of (5.45) at $t_s = 1.027884435$ with $L = 10$ and $\beta = 1$. (b) Log-log plot of h_{min} versus $\tau = t_s - t$. (c) Log-log plot of $\max|h_{zz}|$ versus $\max|h_z|^4$.

In addition, as discussed in Lister *et al.* [35], the length of the film affects the final shape of the solution when $\beta \neq 0$ as well. Wavy structures appear and the breakup tends to be asymmetric. Figure 5.5 outlines the final shapes of the almost-ruptured films for (a) $L = 15$, (b)$L = 20$ and (c)$L = 30$.

5.4 Boundary-integral Method

In this section we solve the Stokes equations coupled with the electrostatic problem numerically, without assuming thin films. A comparison between asymptotic solutions and the simulations is also carried out.

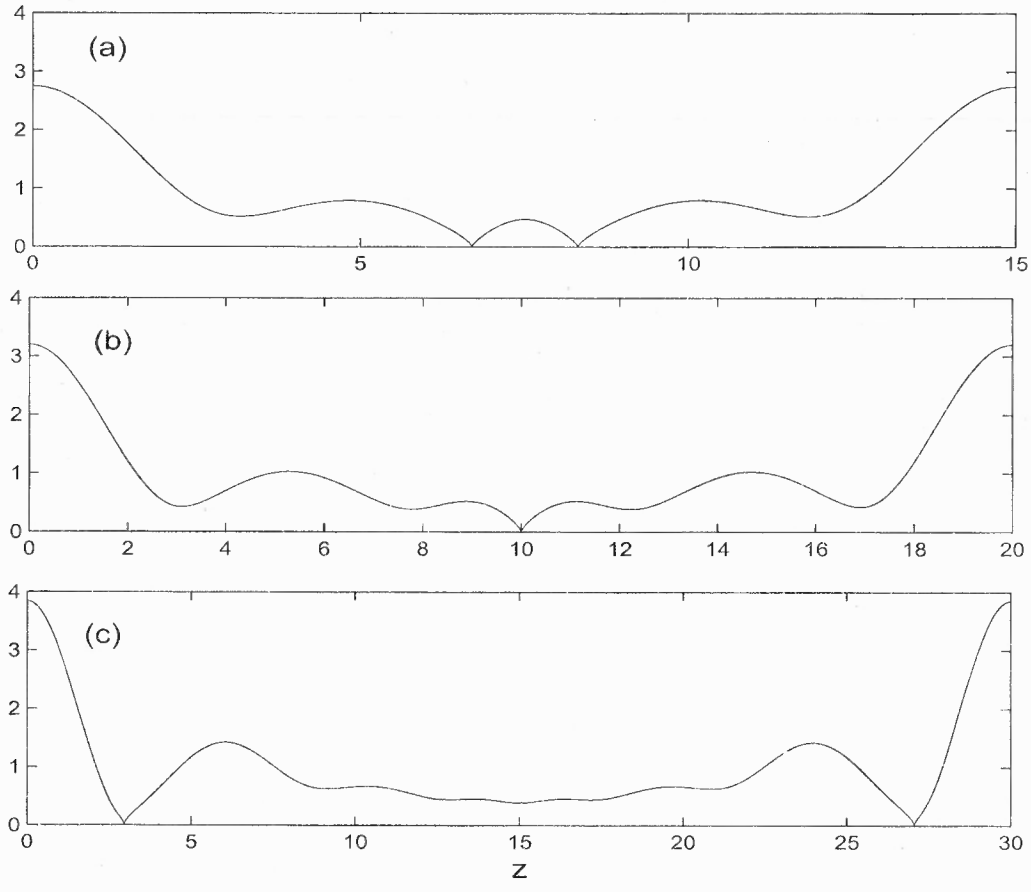

Figure 5.5 Solutions of (5.45) for various axial lengths with $\beta = 1$. (a) $L = 15$, (b)$L = 20$, (c)$L = 30$.

5.4.1 Formulation

The boundary integral method has been used widely to study physical and mathematical problems for decades and the reader can be referred to, to name a few, Acrivos & Rallison [1], Pozrikidis [43] and recently Dubash & Mestel [14] for example. The derivation and theory regarding the method for Stokes flow are well documented in Pozrikidis [48]. Here we start with the equation in axisymmetric form (see Pozrikidis [49])

$$\begin{aligned} u_\alpha(\mathbf{x}_0) \quad + \quad & \frac{\lambda - 1}{4\pi(\lambda + 1)} \int_I^{PV} Q_{\alpha\beta\gamma}(\mathbf{x}, \mathbf{x}_0) u_\beta(\mathbf{x}) n_\gamma(\mathbf{x}) dl(\mathbf{x}) \\ = \quad & -\frac{1}{4\pi(\lambda + 1)} \int_I M_{\alpha\beta}(\mathbf{x}, \mathbf{x}_0) \triangle f_\beta(\mathbf{x}) dl(\mathbf{x}), \end{aligned} \tag{5.51}$$

where the subscripts run over cylindrical coordinates z or r, PV denotes the principal value of the double-layer integral, I is the interface over one period, $\mathbf{x}_0$ lies on the interface and $\boldsymbol{n}$ is the unit outward normal vector along the interface. The kernels M and Q are the periodic Green's functions of axisymmetric Stokes flow for the velocity and stress inside the tube. $\triangle f$ is the force jump across the thread surface and is given by

$$\triangle \mathbf{f} = [\kappa - \frac{E_b}{2}\left(\frac{\partial \phi}{\partial n}\right)^2]\mathbf{n}, \tag{5.52}$$

where κ is the curvature and E_b is the electric parameter defined in section 5.1 (see also Dubash & Mestel [14]); ϕ_n will be calculated from the electrostatic problem which is discussed later in this section.

The velocity field will be determined by the single layer potential only for the simplest case $\lambda = 1$. In that case only the Green's function inside the tube is needed and the no-slip boundary condition requires that the Stokeslets should vanish at the wall. The details of the construction of the Stokeslets can be found in Pozrikidis [48]. Meanwhile, it is found that the double layer potential term will disappear along the tube wall automatically. So the axisymmetric free space Stresslets is used directly in our computation for $\lambda \neq 1$.

Next the boundary integral equation for electric potential ϕ is given. From Dubash & Mestel [14], the equation can be written as

$$-\frac{1}{2}\phi(\mathbf{x}_0) + \int_I^{PV} \frac{\partial P(\mathbf{x}, \mathbf{x}_0)}{\partial n}\phi(\mathbf{x})r(\mathbf{x})dl = \int_I P(\mathbf{x}, \mathbf{x}_0)\phi_n(\mathbf{x})r(\mathbf{x})dl, \tag{5.53}$$

where P is the periodic Green's function for the potential problem. Knowing $\phi = 1$ at the wall, it also requires P vanishes on the wall. In addition, no flux condition due to the periodic structure is required along $z = 0$ and $z = L$, i.e. $\phi_n(z = 0, r) = \phi_n(z = L, r) = 0$. Hence, axial images are chosen so that $P_n(z = 0, r) = P_n(z = L, r) = 0$ is satisfied.

Before constructing P we first show how to choose axial images. We denote the axisymmetric Green's function by G and express it in cylindrical coordinates (r, z),

$$G(r, z, r_0, z_0) = \sum_{k=-\infty}^{+\infty} (G^R(r, z, r_0, z_0 + 2kL) + G^R(r, z, r_0, -z_0 + 2kL)), \tag{5.54}$$

where G^R is the axisymmetric free space Green's function given in Appendix B and L is the period. Therefore, a simple calculation confirms $G_z(z = 0) = G_z(z = L) = 0$. We show the calculation of G_z at $z = 0$ for completeness and start from the 3-D free space Green's function $G_0(\mathbf{x}, \mathbf{x}_0)$ of the periodic version,

$$\begin{aligned} G^P(x, y, z, x_0, y_0, z_0) &= \sum_{k=-\infty}^{+\infty} G_0(x, y, z, x_0, y_0, z_0 + 2kL) + G_0(x, y, x, x_0, y_0, -z_0 + 2kL) \\ &= \sum_{k=-\infty}^{+\infty} \frac{1}{4\pi((x - x_0)^2 + (y - y_0)^2 + (z - z_0 - 2kL)^2)^{1/2}} \\ &+ \frac{1}{4\pi((x - x_0)^2 + (y - y_0)^2 + (z + z_0 - 2kL)^2)^{1/2}}. \end{aligned} \tag{5.55}$$

Notice that the complementary part of the Green's functions has not been added yet which aids to satisfy the boundary conditions at the wall. However the idea and calculations are similar (not shown here). Taking a derivative with respect to z in expression (5.55) gives

$$\begin{aligned} \frac{\partial G^P}{\partial z}(x, y, z, x_0, y_0, z_0) = \sum_{k=-\infty}^{+\infty} &- \frac{z - z_0 - 2kL}{4\pi((x - x_0)^2 + (y - y_0)^2 + (z - z_0 - 2kL)^2)^{3/2}} \\ &- \frac{z + z_0 - 2kL}{4\pi((x - x_0)^2 + (y - y_0)^2 + (z + z_0 - 2kL)^2)^{3/2}}. \end{aligned} \tag{5.56}$$

Evaluating (5.56) at $z = 0$ yields

$$\begin{aligned}\frac{\partial G^P}{\partial z}(x, y, z = 0, x_0, y_0, z_0) &= \sum_{k=-\infty}^{+\infty} \frac{z_0 + 2kL}{4\pi((x-x_0)^2 + (y-y_0)^2 + (z_0+2kL)^2)^{3/2}} \\ &+ \frac{-z_0 + 2kL}{4\pi((x-x_0)^2 + (y-y_0)^2 + (z_0-2kL)^2)^{3/2}} \\ &= \sum_{k=-\infty}^{+\infty} \frac{z_0 + 2kL}{4\pi((x-x_0)^2 + (y-y_0)^2 + (z_0+2kL)^2)^{3/2}} \\ &+ \sum_{k=-\infty}^{+\infty} \frac{-z_0 - 2kL}{4\pi((x-x_0)^2 + (y-y_0)^2 + (z_0+2kL)^2)^{3/2}} \\ &= 0. \end{aligned} \tag{5.57}$$

Also noting that the z direction (axial direction) is independent of θ, G_z at $z = 0$ becomes

$$\begin{aligned} G_z(z=0) &= \left(\frac{\partial}{\partial z}\int_0^{2\pi} G^P d\theta\right)|_{z=0} \\ &= \int_0^{2\pi} (G_z^P(z=0))d\theta \\ &= 0. \end{aligned} \tag{5.58}$$

A similar procedure works for $z = L$.

After manipulating the images in the axial direction, a simpler expression for ϕ is obtained

$$\phi(\mathbf{x}_0) = 1 + \int_I P(\mathbf{x}, \mathbf{x}_0)\phi_n(\mathbf{x})r(\mathbf{x})dl(\mathbf{x}). \tag{5.59}$$

The derivation of P is similar to Stokeslets and is simpler. Starting from the ring of point forces, G^R in free space, the Green's function inside a tube can be written as

$$G^T = G^R + G^C, \tag{5.60}$$

the superscripts T and C stand for 'tube' and 'complementary' respectively. $G^T(z, z_0, r = d, r_0) = 0$ is required, where d is the tube radius. After some algebra and manipulating identities (see Duffy [15] and Pozirikidis [48]), the Green's function reads

$$\begin{aligned} G^R &= \frac{1}{4\pi}\int_0^{2\pi} \frac{1}{|\mathbf{x}-\mathbf{x}_0|} d\theta \\ &= \frac{F(m)}{\pi\sqrt{(z-z_0)^2+(r+r_0)^2}} \\ &= \frac{1}{\pi}\int_0^{\infty} I_0(kr_0)K_0(kr)\cos(k(z-z_0))dk, \qquad (5.61) \\ G^C &= -\frac{1}{\pi}\int_0^{\infty} \frac{K_0(kd)}{I_0(kd)} I_0(kr)I_0(kr_0)\cos(k(z-z_0))dk, \qquad (5.62) \end{aligned}$$

where $m = 4rr_0/((z-z_0)^2+(r+r_0)^2)$ and F is the complete elliptic integrals of the first kind. Letting

$$G^C = \int_0^{\infty} g(k)\cos(k(z-z_0))dk, \qquad (5.63)$$

the singular behavior of the integrand is observed when k tends to zero, namely, $g = \frac{1}{\pi}\ln k + \ldots$. Because this is just logarithmic, the corresponding integral still exists. For a computation convenience, we regularize the integral representation by using the identity (e.g. see Pozrikidis [48])

$$\frac{\pi}{2((z-z_0)^2+(2d-r-r_0)^2)^{1/2}} = \int_0^{\infty} K_0(k(2d-r-r_0))\cos(k(z-z_0))dk \qquad (5.64)$$

and write

$$\begin{aligned} G^C &= \int_0^{\infty} (g(k) + \frac{1}{\pi}K_0(k(2d-r-r_0)))\cos(k(z-z_0))dk, \\ &- \frac{1}{2((z-z_0)^2+(2d-r-r_0)^2)^{1/2}}. \qquad (5.65) \end{aligned}$$

As k tends to zero, $K_0(k(2d-r-r_0))$ behaves as $-\ln(k(2d-r-r_0))$ and the modified integrand

$$g' = g + \frac{1}{\pi}K_0 \qquad (5.66)$$

tends to a finite value. Then the periodic version the Green's function can be obtained immediately by summing over the index,

$$\begin{aligned} P(z,r,z_0,r_0) &= \sum_{n=-\infty}^{\infty} (G^R(z+nL,z_0,r,r_0)+G^C(z+nL,z_0,r,r_0)), \\ &= \frac{2\pi}{L}\left[\frac{1}{2}g'(k=0)+\sum_{m=1}^{\infty} g'(k_m)\cos(k_m\hat{z})\right] \\ &+ \sum_{n=-\infty}^{\infty}\left[G^R(\hat{z}+nL)-\frac{1}{2((\hat{z}+nL)^2+(2d-r-r_0)^2)^{1/2}}\right] \end{aligned} \quad (5.67)$$

where L is the period, $k_m = 2\pi m/L$ and $\hat{z} = z - z_0$. The first sum in (5.67) converges exponentially, while the second one converges algebraically. The convergence of the sum is discussed in detail in Pozrikidis [48].

5.4.2 Numerical Method

In this section the numerical implementation of the boundary-integral method is briefly described. Because of the nature of the electric fields, we can compute ϕ_n by only knowing the surface position and independently of the flow. Then substitute it into (5.52) and solve for (5.51). After obtaining the velocities, the interface is advanced by the kinematic condition. In the simulations presented in this chapter, the time integration is carried out by an Euler method or second order Runge-Kutta method. The weak singularities in the kernels in the single-layer potential terms are handled by Gauss-log quadrature and the regular integrals are computed by standard 8-point or 16-point Gauss-Legendre quadratures. Another way to tame the singularity in (5.51) is to take advantage of the result with $\mathbf{x}_0$ on the interface I

$$\int_I M_{\alpha\beta}(\mathbf{x},\mathbf{x}_0)n_\beta(\mathbf{x})dl(\mathbf{x}) = 0. \quad (5.68)$$

So the single-layer term in (5.51) can be rewritten as

$$\int_I M_{\alpha\beta}(\mathbf{x},\mathbf{x}_0)(\triangle f_\beta(\mathbf{x}) - \triangle f_\beta(\mathbf{x}_0))dl(\mathbf{x}), \quad (5.69)$$

whose kernel now is regular, hence Gauss-Legendre quadrature can be applied directly. The curvature of the interface is calculated by using cubic-splines which is also used to redistribute the nodal points along the interface at each time step in order to maintain good resolution. The linear system after discretization of the integral equations is solved by fortran package LAPACK. Also, in our computations, the for-aft symmetry is forced, hence only half the period of the thread needs to be computed.

Introducing $\mathbf{u} = (u_z, u_r)$ and $\mathbf{F} = (F_z, F_r)$, (5.51) may be written as

$$\begin{pmatrix} u_z \\ u_r \end{pmatrix} + \frac{\lambda - 1}{4\pi(\lambda + 1)} \int_{S_1} \begin{pmatrix} S_{zz} & S_{zr} \\ S_{rz} & S_{rr} \end{pmatrix} \begin{pmatrix} u_z \\ u_r \end{pmatrix} dl = \begin{pmatrix} F_z \\ F_r \end{pmatrix}, \tag{5.70}$$

where $S_{\alpha\beta} = Q_{\alpha\beta\gamma} n_\gamma$. In addition,

$$\begin{pmatrix} F_z \\ F_r \end{pmatrix} = -\frac{1}{8\pi} \int_{S_1} \begin{pmatrix} M_{zz} & M_{zr} \\ M_{rz} & M_{rr} \end{pmatrix} \begin{pmatrix} \triangle f_z \\ \triangle f_r \end{pmatrix} dl, \tag{5.71}$$

where $\triangle f$ is given in (5.52). Therefore, a linear system with unknown $\mathbf{u} = (u_z, u_r)$ is obtained.

Before presenting numerical results of electrified threads we test the numerical results against the linear theory. Figure 5.6 shows the evolving amplitude from a nonlinear computation for a set of particular parameters, $d = 2.5$, $E_b = 0.47$, $ka = 2/3$ and $\lambda = 1$. The dimensionless amplitude of the perturbation is taken to be 0.01 which is small. Clearly the solid line that corresponds to the nonlinear computation evolves with the dashed line that is predicted by linear result from section 5.2 and the agreement is excellent. Further validations of the code are presented later.

5.5 Results and Discussion

5.5.1 Nonlinear Evolution of Unbounded Liquid Threads

We begin by considering an unbounded thread ($d = \infty$) with the electric field absent. Figure 5.7 shows the nonlinear evolution in this case with differing viscosity ratios.

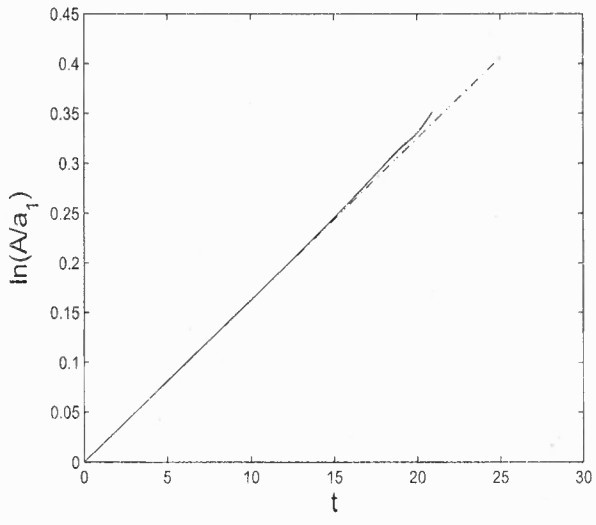

Figure 5.6 A is defined as half the difference between the maximum and minimum location of the interface. Solid line is for numerical simulation, while the dashed line is from linear theory. $\lambda = 1, \quad E_b = 0.47, \quad d = 2.5.$

The initial condition used is

$$S(z,0) = a + a_1 \cos(kz), \tag{5.72}$$

where $a_1 = 0.5a$ is the amplitude of perturbation and a is the unperturbed thread radius. In Figure 5.7, $k = 2\pi/L$ is set to be 0.5, i.e. the wavenumber $ka = 0.5$ where L is the wave length (period). Panel (a) shows a single Stokes jet evolving in air or vacuum, namely, $\lambda = 0$. Symmetric pinching is observed and no satellite drops are formed in between as shown through a long-wave theory by Papageorgiou [45]. This full simulation also agrees with the results in Pozrikidis [49]. Panel (b)-(d) in Figure 5.7 illustrate the evolutions of jets for $\lambda = 0.1$, 1 and 10 respectively. Under the external viscous drag ($0 < \lambda < \infty$), the breakup is always asymmetric and different satellite structures are obtained through numerical simulation. Clearly, the viscous effect of the surrounding fluid plays an important role in determining the dynamics and the thinning process, as well as the breakup location. For $\lambda = 10$, the breakup point tends to move further to the right compared to the case $\lambda = 1$. When $\lambda = 0.1$,

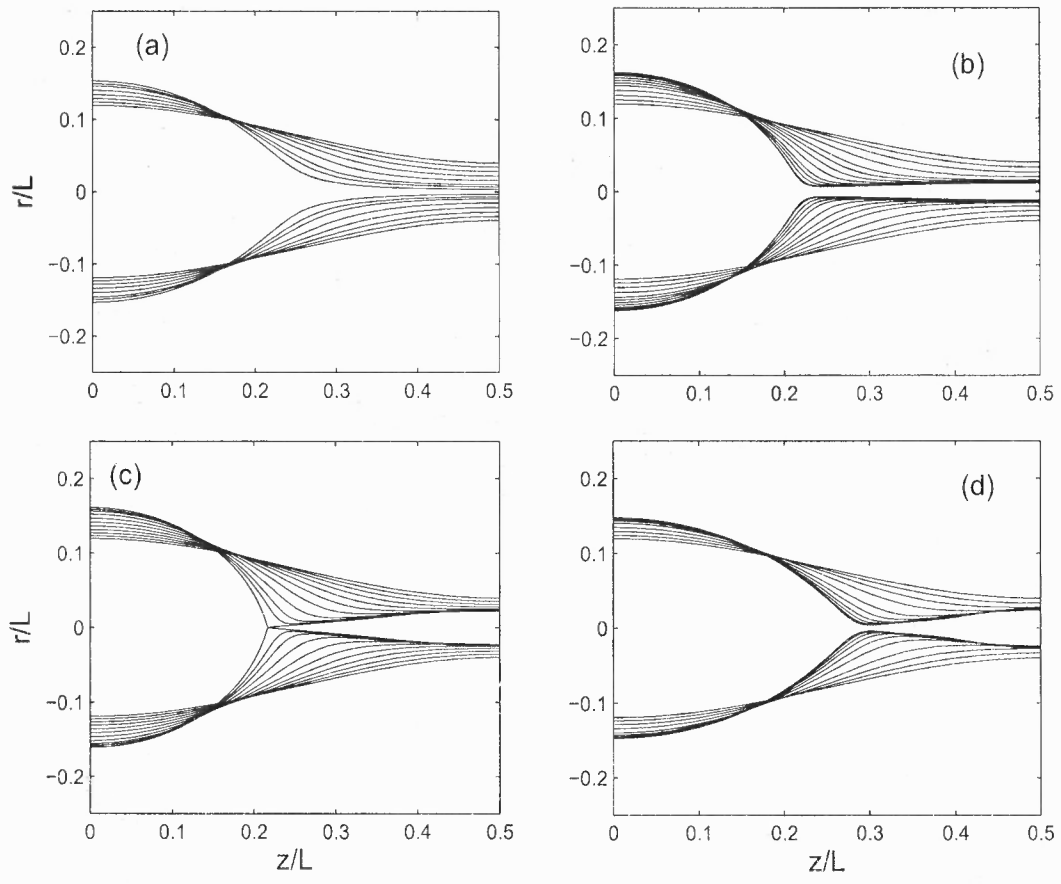

Figure 5.7 Evolutions of jet profile over half period for differing viscosity ratios: (a) $\lambda = 0$, (b) $\lambda = 0.1$, (c) $\lambda = 1$ and (d) $\lambda = 10$.

a nearly cylindrical thin thread is formed between main drops and the breakup point is expected to occur away from the middle of the one period domain. In fact the minimum neck point moves slightly to the left when $\lambda < 1$ compared with the one in $\lambda = 1$ as can be seen from Figure 5.8. The differences regarding the location of the breakup point is due to the competition of internal and external viscous forces as described in Lister & Stone [36]. In Figure 5.8, accurately computed jet profiles in the pinching stage are plotted for $\lambda = 0.03$ in panel (a), $\lambda = 1$ in panel (b) and $\lambda = 20$ in panel (c). The code stopped when the dimensionless minimum radius is approximately equal to $3 \sim 6 \times 10^{-3}$. Up to 500 points over half period are used near

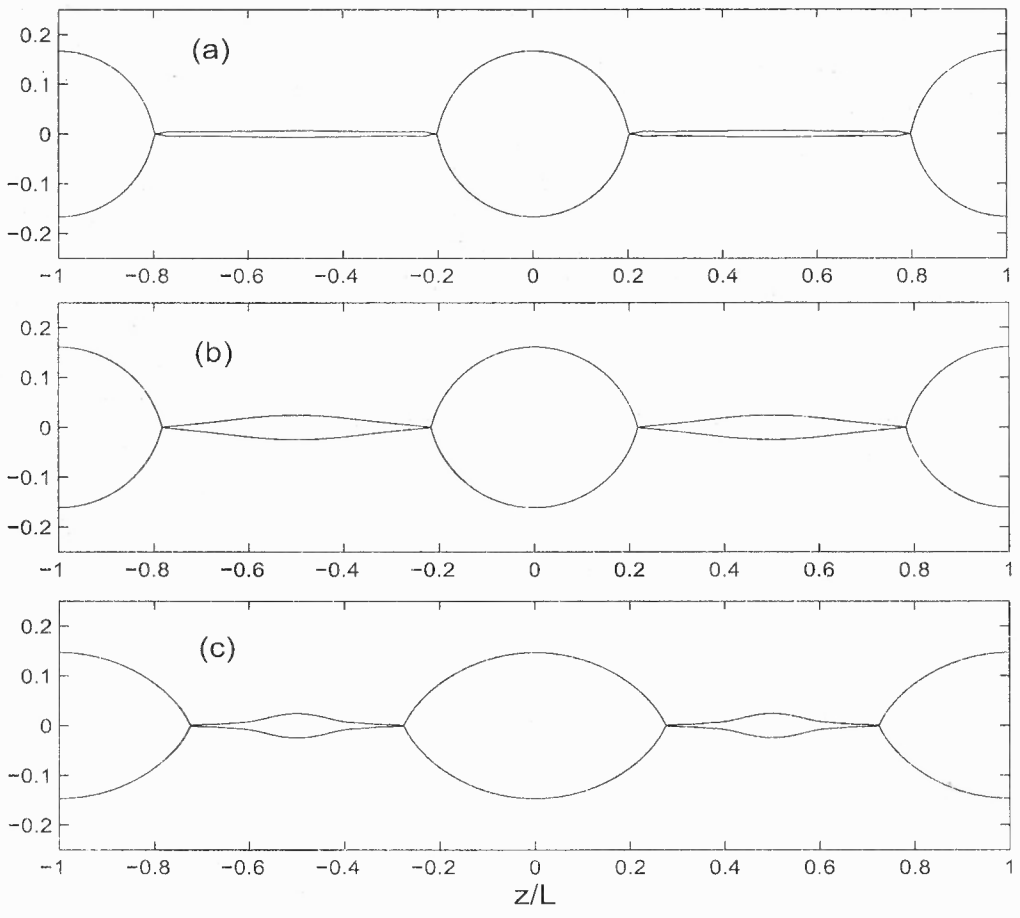

Figure 5.8 Final computed stage of thread pinching in left panel for different viscosity ratios, (a) $\lambda = 0.03$, (b) $\lambda = 1$ and (c) $\lambda = 20$.

breakup. The evolution of S_{min} against time and the corresponding axial velocities are shown in panel (a) and (b) in Figure 5.9 respectively. As seen from the linear theory, the perturbation grows very slowly when the thread is less viscous than the ambient fluid. It takes over 100 dimensionless time units to approach the breakup for $\lambda = 20$ seen in panel (a) in Figure 5.9. In addition it is seen from panel (b) that the shifting of the pinching point is evident by inspecting the blowup of axial velocities close to pinching.

As discussed by Lister & Stone [36] the local dynamics follows the scalings $S \sim z \sim \tau$ near breakup provided the internal viscosity is comparable or much bigger

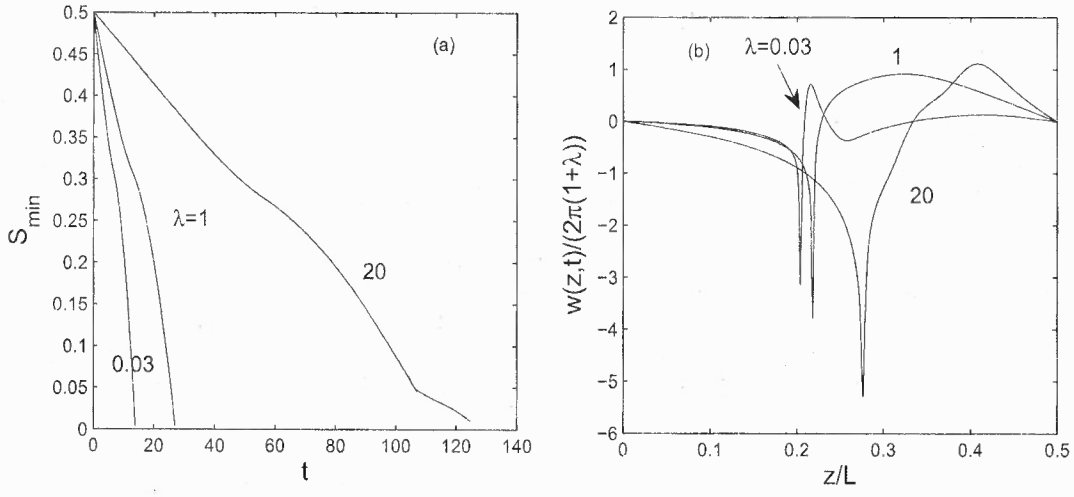

Figure 5.9 (a) Evolution of S_{min} for viscosity ratios $\lambda = 0.03$, 1 and 20 at final computed stage. (b) Corresponding axial velocities close to breakup.

than the external one. The axial velocity increases slowly as a logarithmic function of S_{min} for the equal viscosity case. Similar results are expected when $\lambda \neq 1$ since the single layer potential is always present and the double layer potential does not contribute much as the geometry is slender. Yet the full numerical simulation has not been carried out and questions still remain open.

5.5.2 Nonlinear Evolution of Electrified Liquid Threads

When a long cylindrical tube is present and a core-annular arrangement enters, the nonlinear dynamics are affected and are quite different from the unbounded thread case. To investigate the effect of external electric fields, the behavior of the flow with the field absent, i.e $E_b = 0$, is considered. Figure 5.10 shows the nonlinear deformations of non-electrified thread profiles under axisymmetric perturbation, for the tube wall $d = 2$ and viscosity ratio $\lambda = 1$. Panel (a) and (b) take different wavenumbers in the initial perturbation. For example, $ka = 0.3$ in panel (a) means the perturbation is a long wave one and the period is long, namely, $L/a = 2\pi/0.3 =$

$20\pi/3$, where a is the unperturbed thread radius in (5.72). Panel (b) in Figure 5.10 illustrates the evolution subject to a perturbation of period $L/a = 3\pi$. In both cases, a fairly large main drop which is elongated in the axial direction (prolate) is observed. In panels (c) and (d) in the same figure, the evolutions of axial velocities reveal the approach to breakup as the interface deforms, and demonstrate the blowup of the axial velocity near pinch-off. Figure 5.11 outlines the pinch-off solutions for fixed $\lambda = 1$ but

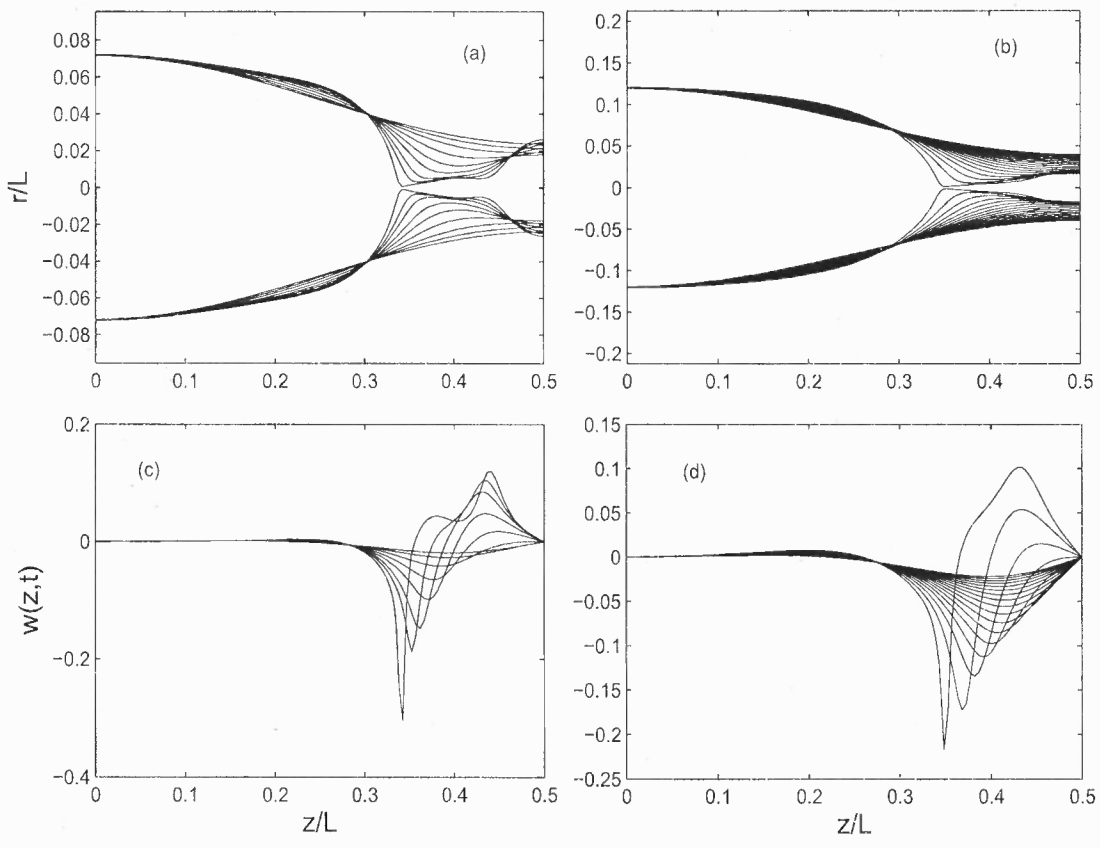

Figure 5.10 Evolution of thread profiles over half period for $d = 2$ fixed with (a) $ka = 0.3$ and (b) $ka = 0.6667$. The corresponding evolutions of axial velocities are illustrated in panel (c) and (d).

different radii. Panels (a)-(c) show the results for $d = 5$, 2 and 1.5 respectively and the upper and lower bound of the figure stand for the position of the outer cylindrical wall. As the fluid interface approaches the wall, i.e. d becomes small, the drop

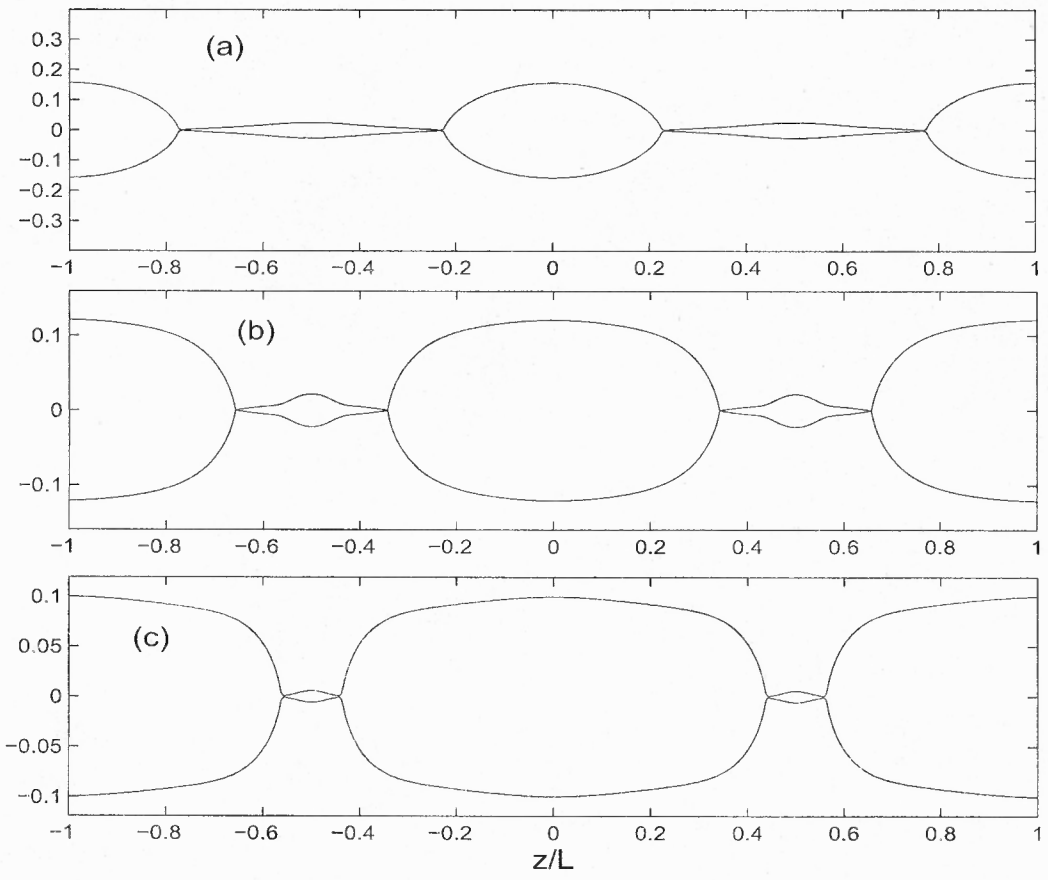

Figure 5.11 Final computed stage of thread pinching in left panel for different tube radius, (a) $d = 5$, (b) $d = 2$ and (c) $d = 1.5$.

structure changes significantly. Relatively big main drops and small satellite drops are obtained when the wall is close to the interface initially (e.g. $d = 1.5$), compared with relatively big d cases (e.g. $d = 5$). Also the geometry of the main drops tends to have a flat portion close to the wall which agrees with laboratory observation (e.g. Bai *et al.* [5]). Meanwhile the presence of the wall slows down the motion which makes the thread take much longer time to break than in the unbounded thread. For instance, the breakup times $t_s = 26.96$ for unbounded threads with $\lambda = 1$ and with the same viscosity ratio, $t_s = 32.96$ for $d = 2$ and $t_s = 112.91$ for $d = 1.5$ are obtained from our calculations.

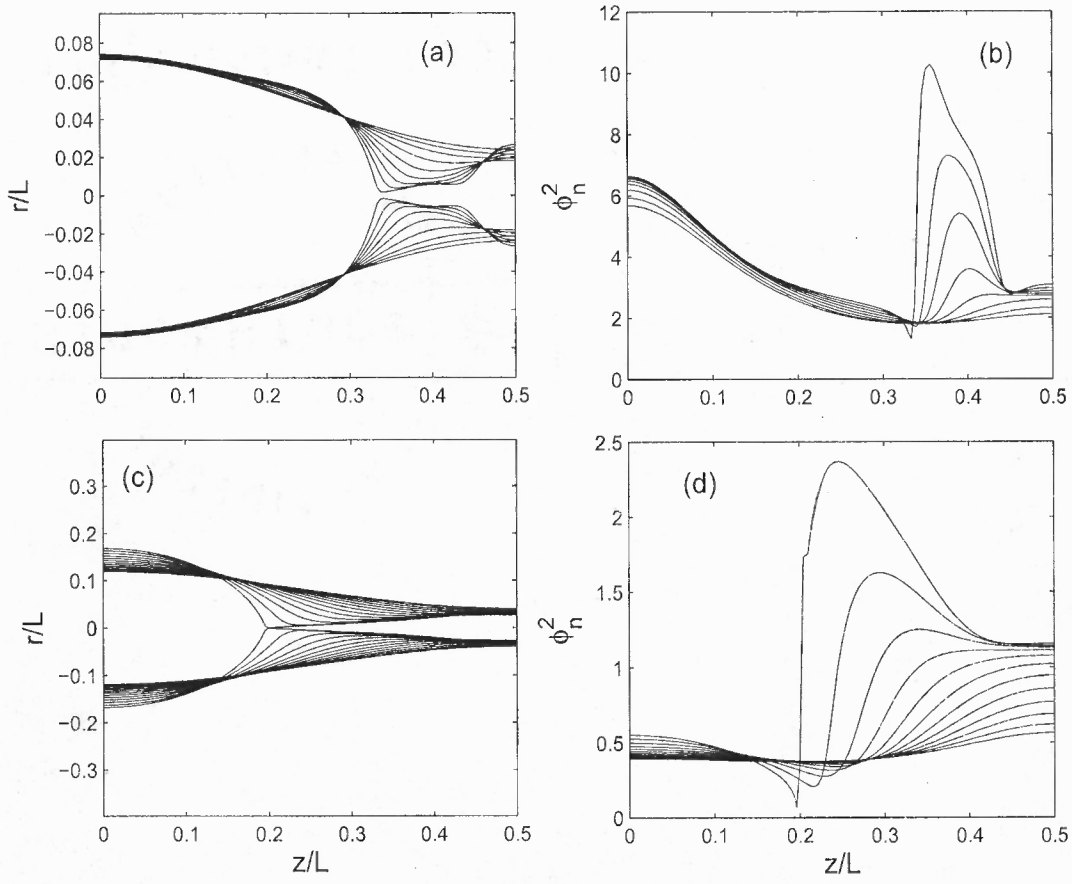

Figure 5.12 Evolutions of core-annular flow profiles ($\lambda = 1$) over half period for (a) $ka = 0.3$, $d = 2$ and $E_b = 0.1047$ and (c) $ka = 0.5$, $d = 5$ and $E_b = 2.513$. Corresponding evolutions of ϕ_n^2 are plotted in panel (b) and (d) respectively.

In the presence of an electric field, Figure 5.12 shows the nonlinear evolution of core-annular flows as well as the corresponding evolution of the electric force ϕ_n^2 with $ka = 0.3$, $d = 2$ in panels (a), (b) and $ka = 0.5$, $d = 5$ in panels (c), (d). As the interface deforms, surface charge tends to accumulate on the satellite drops, through which the electric force acts as an additional driving force to break the thread. A large value of ϕ_n^2 is observed in the vicinity of the breakup point but not at the breakup point itself (we will discuss this later). Instead, the electric force tends to zero at the very breakup point, because no charge exists there at pinch-off. Figure 5.13 compares the final pinch-off solutions for varying electric field strength with

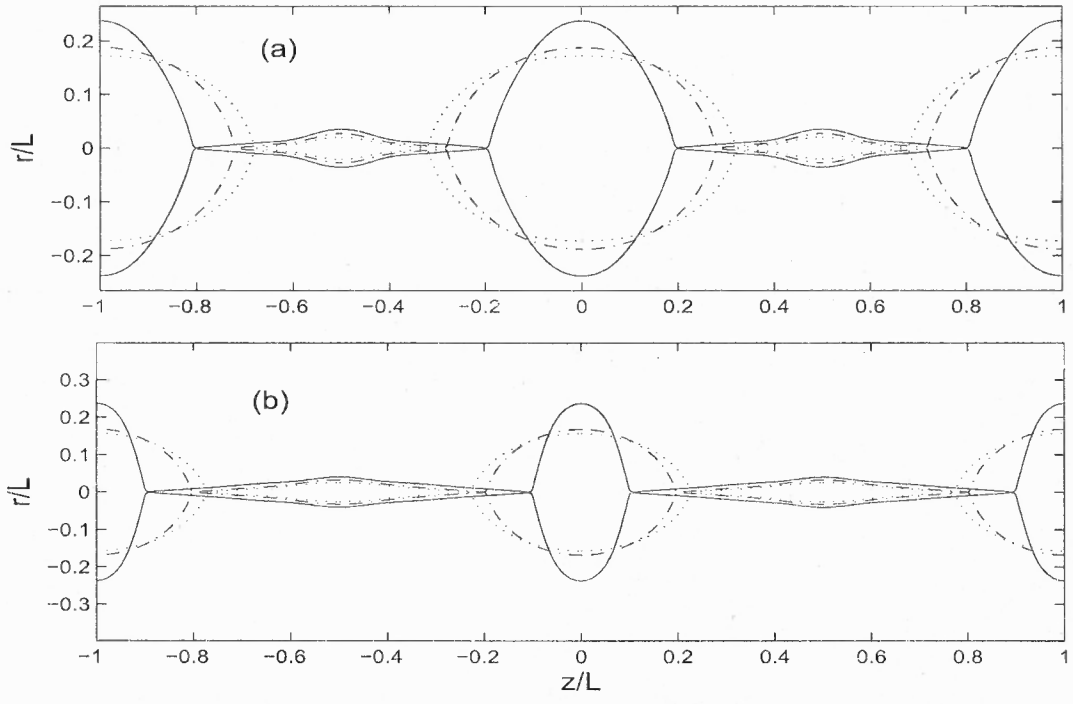

Figure 5.13 Pinching solution of the core-annular flows for the equal viscosity case (a) $ka = 0.6667$, $d = 2.5$, $E_b = 0.0$, 0.4712, 0.9425 correspond to dotted, long-short dashed and solid lines respectively; (b) $ka = 0.5$, $d = 5$,$E_b = 0.0$, 2.5133, 5.0625 correspond to dotted, long-short dashed and solid lines respectively. The upper and lower bounds of the figures stand for position of the tube wall.

$d = 2.5$, $ka = 0.6667$ in panel (a) and $d = 5$, $ka = 0.5$ in panel (b). It can be seen that the effect of electric field is to elongate the main drops radially in the direction of the electric field, and hence change their shapes. Meanwhile the volume of the satellite drops is also changed. Due to the accumulation of charge at the interface the satellite drops become bigger than in the non-electrified case. This phenomenon is also observed by Satiawan & Heister [59], Lopez-Herrera et al. [38] and Collins *et al.* [11] which implies its universality and that it is independent of fluid properties. Following Lopez-Herrera et al. [38], we can assess the stability of the main and satellite drops by calculating the charge Q that they carry at pinch-off and compare with the Rayleigh charge limit (hereinafter referred to Q_R), which shows the upper bound of the amount of charge that a spherical drop can bear (see Rayleigh [53]).

In terms of dimensionless groups, in the present work, $Q_R^2 = 48\pi E_b V$, where V is

Table 5.1 Some Characteristics Of Main And Satellite Drops After Pinch-off For The Case $d = 2.5$ & $ka = 0.6667$

$E_b a$	R_s/R_{s0}	R_m/R_{m0}	Q_{Rs}	Q_s/Q_{Rs}	Q_{Rm}	Q_m/Q_{Rm}
0.005	1.0214	0.9999	1.0057	4.6604	15.3487	4.6084
0.01	1.0429	0.9999	1.4667	3.2181	21.7063	3.2610
0.05	1.2403	0.9991	4.2554	1.1577	48.4754	2.0429
0.1	1.5613	0.9965	8.4990	1.1663	68.2937	1.4934

Table 5.2 Some Characteristics Of Main And Satellite Drops After Pinch-off For The Case $d = 5$ & $ka = 0.5$

$E_b a$	R_s/R_{s0}	R_m/R_{m0}	Q_{Rs}	Q_s/Q_{Rs}	Q_{Rm}	Q_m/Q_{Rm}
0.1	1.0726	0.9985	13.88	0.7167	90.75	0.4423
0.2	1.1634	0.9955	22.17	0.4991	127.83	0.311
0.4	1.4631	0.9862	44.22	0.2217	178.15	0.3716
0.43	1.5347	0.9831	49.25	0.2097	183.83	0.4344

the dimensionless volume of a drop. Since many drops formed at breakup are highly deformed, the ratio $Q/Q_R < 1$ does not guarantee the stability of the drops after pinch-off. On the other hand, the case $Q/Q_R > 1$ usually implies instability and the drop will breakup further into more droplets to redistribute the amount of charge it carries. Table 5.1 outlines the change of surface charge and effective drop radius in the case $d = 2.5$ and $ka = 0.6667$, where the subscript s and m represent the satellite and main drops, respectively. The effective drop radius is defined as

$$R = \left(\frac{3V}{4\pi}\right)^{1/3}, \tag{5.73}$$

and R_0 corresponds to the effective radius in the non-electrified case. Table 5.1 shows that the effective radius of satellite drops increases as E_b increases, which provides evidence of bigger satellite drops with increasing electric field. At the same time the size of the main drop decreases as expected. It is interesting to notice that in the case $d = 2.5 < e$ the ratio Q/Q_R is always bigger than one for both main and satellite drops. Thus further breakup is expected to follow. In addition, Q/Q_R decreases as E_b increases which shows a certain stabilizing effect of the electric field but we also notice that the change of the charge ratio is not monotonic which differs from the results shown for most cases in Collins *et al.* [11]. For example, Q_s/Q_{Rs} for $E_b a = 0.1$ is slightly bigger than the value for $E_b a = 0.05$. As will be shown later this is due to a transition between different breakup scenarios. In Table 5.2 analogous results are presented for the case $d = 5$ and $ka = 0.5$. Again bigger satellite and smaller main drops are found. For this case $d = 5 > e$, and the charge ratios are all below unity, which indicates that an electrode located far away leads to relatively stable drops after pinch-off.

Figures 5.14 and 5.15 illustrate further the fluid motion ($d = 2$ and $d = 5$ as in Figure 5.12) approaching breakup for the core-annular flow with and without electric field. In Figure 5.14, $d = 2$, and, the electrode is relatively close to the fluid interface compared with $d = 5$ in Figure 5.15. A pinch-off solution is still obtained and the flow pattern is almost the same when an electric field is present as in the non-electrified case near the break point. However the far field flow on the main drop is quite different as seen from the results. Based on previous linear theory it is shown that when $d < e$ always leads to linear instability. Physically this is due to the small gap between the electrode and the S_{max}, so that the electric stress is bigger along the interface of the big drop where more charge accumulates. This can also be discovered from Figure 5.12 (b) which shows ϕ_n^2 along $0 < z/L < 0.1$ is bigger than the value near $z/L = 0.5$. Therefore after pinch-off, the main drops will tend to be unstable

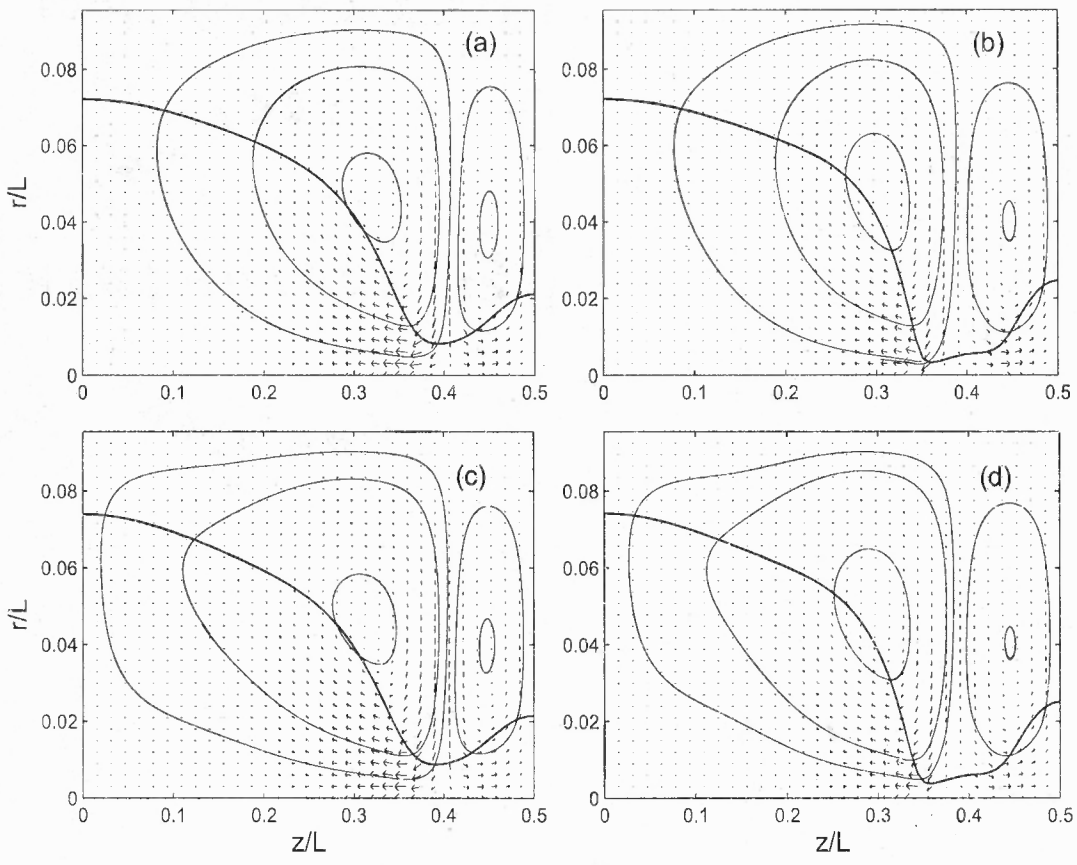

Figure 5.14 The disturbance velocity field and instantaneous streamline patterns with $\lambda = 1$, $d = 2$, $ka = 0.3$. Panel (a) and (b) outline the results for $E_b = 0$ at $t = 52.005$ and 57.017 respectively. Panel (c) and (d) outline the results for $E_b = 0.1047$ at $t = 53.506$ and 60.534 respectively.

and be elongated further in the direction of the electric field. Interestingly the result is actually opposite when $d = 5 > e$ (see Figure 5.12 (d)), in which case the satellite carries a higher concentration of surface charges, hence is potentially unstable after pinch-off. The instantaneous velocity field together with streamline patterns before pinch-off are presented in Figure 5.15, which shows that the presence of the electric field allows the small eddy on the satellite drop to grow bigger. Hence more fluid flows back and a longer (bigger) satellite drop is formed than in the non-electrified case. As a result, the flow field is distorted further by adding the electric field.

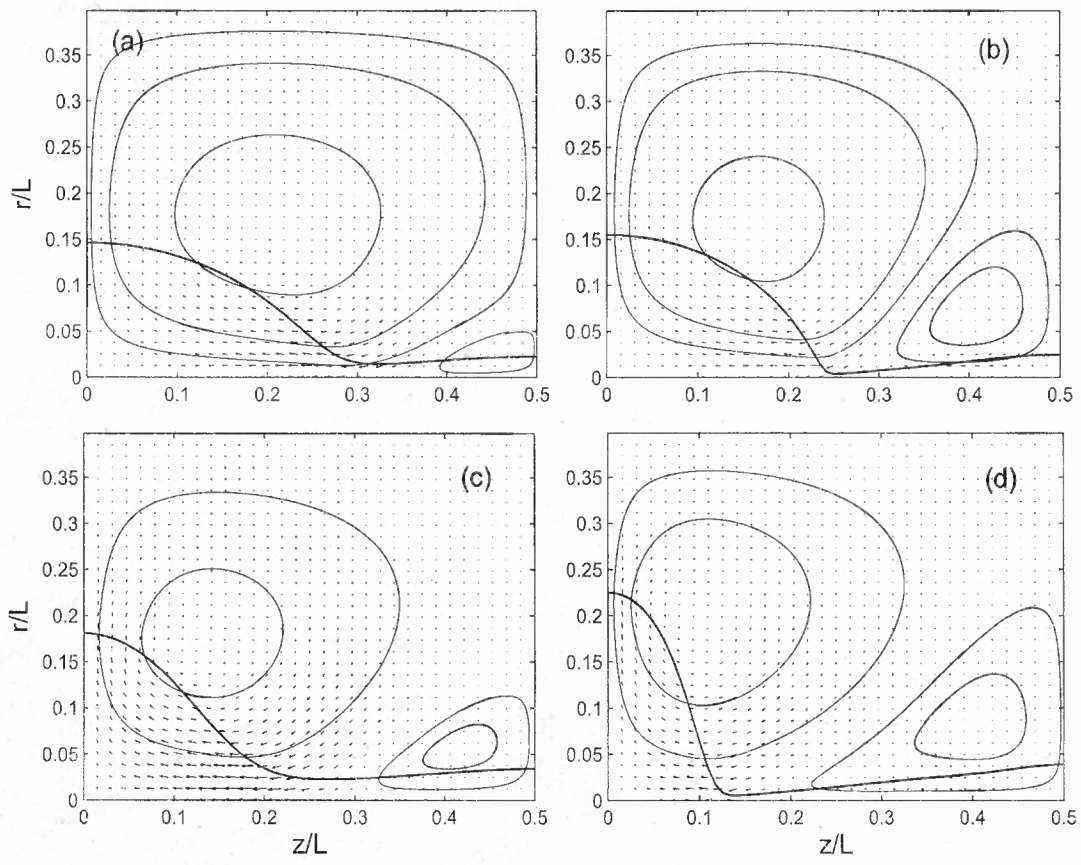

Figure 5.15 The disturbance velocity field and instantaneous streamline patterns with $\lambda = 1$, $d = 5$, $ka = 0.5$. Panel (a) and (b) outline the results for $E_b = 0$ at $t = 21.49$ and 26.41 respectively. Panel (c) and (d) outline the results for $E_b = 5.03$ at $t = 34.54$ and 37.74 respectively.

For a longer period $L/a = 10\pi$, i.e. $ka = 0.2$, with $d = 5$, Figure 5.16(a) illustrates a complex formation of satellite drops under the electric stresses. In this case, the axial length of the satellites is bigger than in the previous cases that we considered, and even before the pinch-off, the drops tend to be unstable due to a high concentration of surface charge. Similar undulation along the jet surface was also observed in the calculations of Setiawan & Heister [59] for inviscid electrified jets subject to long wave length perturbation ($ka = 0.4$ in their paper). The instantaneous velocity field and streamline patterns over half period are shown in Figure 5.16 in

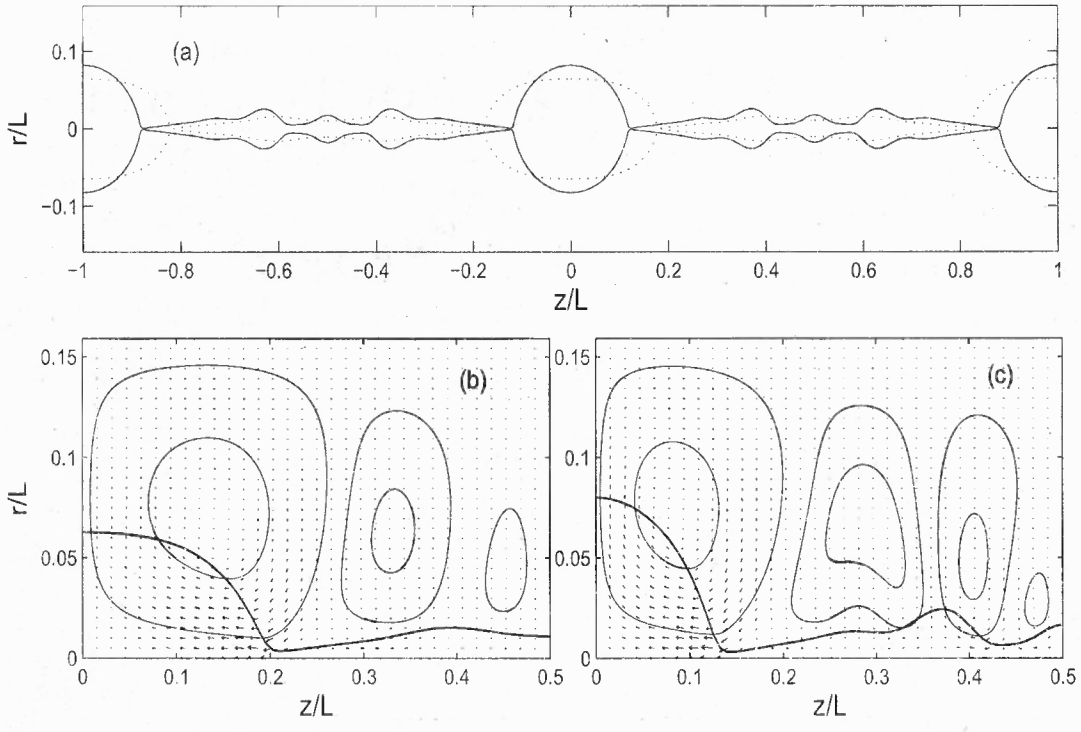

Figure 5.16 (a) Complex satellite formation for electrified core-annular thread with $ka = 0.2$, $d = 5$ and $E_b = 3.142$. Dotted line represent the non-electrified solution. Panel (b) and (c) show the instantaneous velocity field and flow patterns before breakup for $E_b = 0$ and $E_b = 3.142$ respectively.

panel (b) (at $t = 73.51$ with $E_b = 0$) and panel (c) (at $t = 122.74$ with $E_b = 3.142$) which suggests that the electric field increases the mobility of the thread significantly (four eddies in the electrified case compared to three in non-electrified case). Complex motion occurs along the interface which may lead to multiple-subsatellite formation after the first pinch-off (see Tjahjadi *et al.* [63] for the uncharged problem but under a different mechanism, caused by shear).

Finally, we show that the pinch-off solution is not always possible. When the electric field strength is strong enough, the fluid interface tends to form a sharp tip that is analogous to the Taylor cone. A small amount fluid tends to be ejected from the thread due to high charge density around that point, or the fluid is simply pulled

up by the electric force then moves towards the electrode. Figure 5.17 illustrates different breakup behaviors for the threads under the electric field. The breakup times are presented by the vertical coordinates in the figure. The upper panel shows the behavior for $d = 2$ and $ka = 0.3$, while in the lower panel corresponds to $d = 5$ and $ka = 0.5$. If a pinch-off solution is obtained, the results show that the breakup is retarded and the shape of the droplets is changed as we discussed earlier. As the electric field increases further, the pinch-off solution is suppressed as we showed in Chapter 3 in the long wave model, and a transition to a touchdown solution takes place. A spiky solution is found for the case $d = 2$ (see the upper panel) around $E_b = 0.25$. If E_b increases further, e.g. $E_b = 0.5027$ in the figure, the shape is completely different and the singular time is smaller than in the previous cases; the fluid spikes up and shoots toward the electrode. For a case that has the electrode is far away, $d = 5$ (lower panel), similar behavior is found. In addition, between the pinch-off and spike solution, a 'transition' solution has also been found. In the lower panel of Figure 5.17 at $E_b = 7.54$, a small droplet tends to be ejected from the top tip of the interface. In Collins *et al.* [11] a similar solution was presented but they claimed that pinch-off still occurs. The difference is due to the choice of d. In their paper, $d = 10$ is taken and this large distance value allows pinching to happen first.

5.5.3 Local Dynamics

As discussed in Lister & Stone [36], near pinch-off the local scaling analysis shows a linear dependence of S_{min} with $\tau = t_s - t$ for the non-electrified problem and the aspect ratio is proportional to $O(\mu_{ext}/\mu_{int})^{1/2}$ which is constant instead of asymptotically small. This implies that for Stokes flow, directly solving the problem may do a better job than the long-wave approximation. It is pointed out in Cohen *et al.* [10] that the slope of the decrease is around -0.0335 (compared with -0.0304 for single

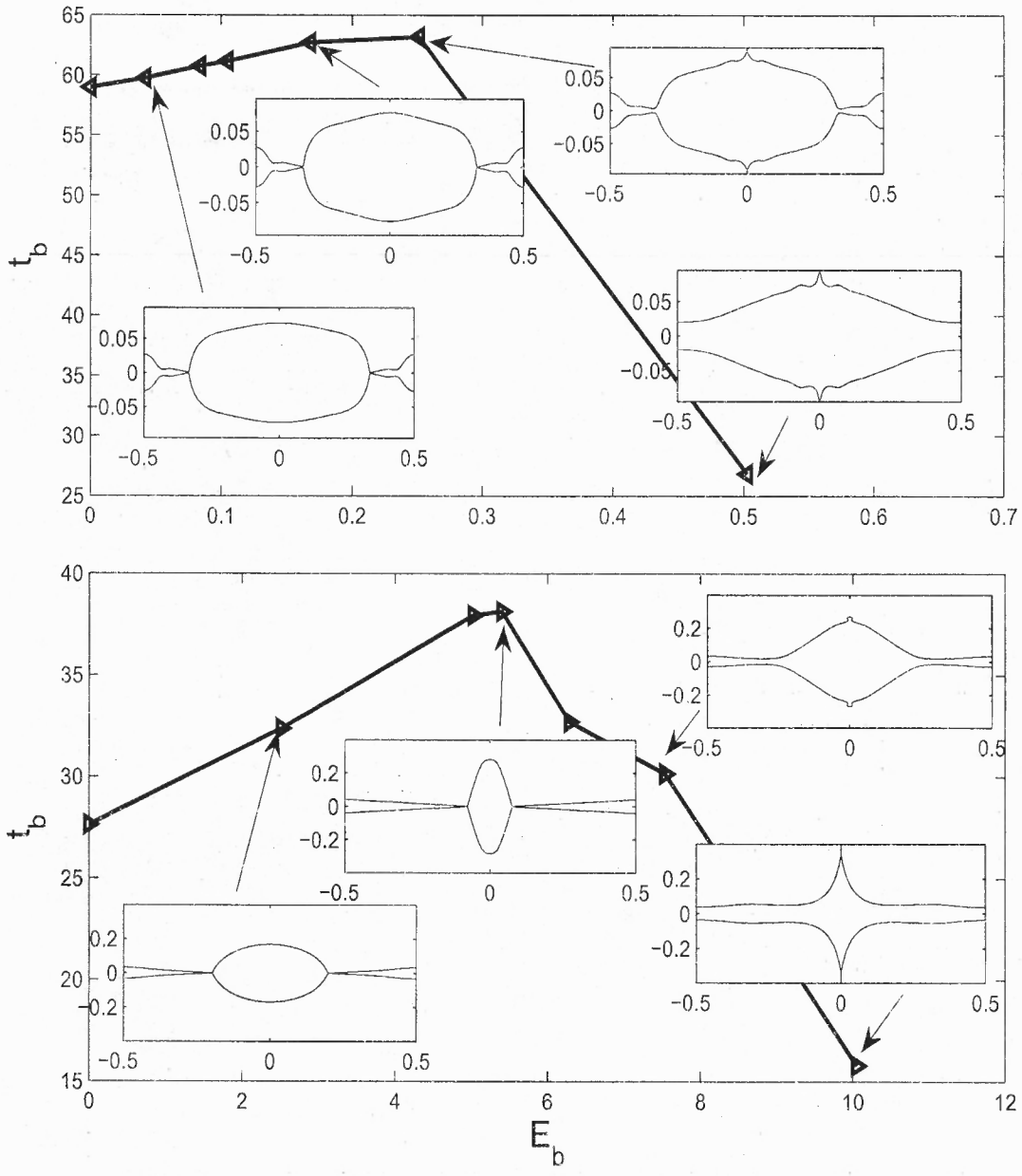

Figure 5.17 Influence of electric parameter E_b on the breakup time for the case (above) $ka = 0.3$, $d = 2$ and (below) $ka = 0.5$, $d = 5$. In addition, different breakup behaviors are identified for different E_b.

Navier-Stokes jet [17] and -0.0709 for single Stokes jet [45]). Similar results are expected for the electrified problem here as discussed next.

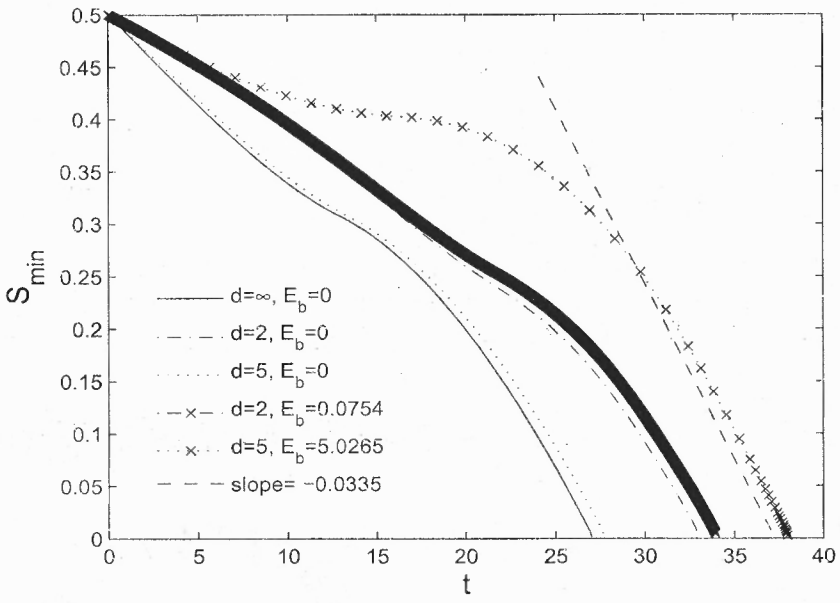

Figure 5.18 Evolution of S_{min} versus time for various d and E_b indicated in the figure.

From previous results (e.g. Figure 5.12), we see that close to pinch-off $\phi_n^2 \to 0$ at the minimum neck position while it takes large values in its vicinity. This can be understood by considering (5.59)

$$\phi(\mathbf{x}_0) = 1 + \int_I P(\mathbf{x}, \mathbf{x}_0)\phi_n(\mathbf{x})r(\mathbf{x})dl(\mathbf{x}),$$

and following Hinch [23] to obtain

$$0 = 1 + \int \frac{\phi_n \epsilon R}{\sqrt{(z - z_0)^2 + \epsilon^2 R^2}} dz + \cdots$$

(for $\mathbf{x}_0$ on the interface) at leading order where $r = \epsilon R(z)$ is assumed. Hence

$$\phi_n \sim O\left(\frac{1}{\epsilon \ln \epsilon^{-1}}\right). \tag{5.74}$$

This is the contribution from the intermediate region of breakup ($\epsilon \ll |z - z_0| \ll L$). Notice that in our long-wave model in Chapter 3, $\phi_n \approx 1/(S \ln S)$ which is consistent with the estimate here. We argued in that chapter that pinching is suppressed by

adding an electric field when the slender geometry is assumed. In fact the gradient of the electric force becomes comparable to the gradient of curvature in the long wave model and hence the pinch-off solution can not be obtained. In contrast, the scaling analysis in the full problem suggests the use of the full curvature and the pinch-off solution is obtained. This indicates that the long-wave model overestimates the electric force and exaggerates it when the neck is small. However, some useful information is still obtained by considering the shallow cone of the pinching solution. Locally it is still a slender thread so we see that the electric effect (balancing the leading order of curvature effect) stops the thread to break at the point where it would have done so in the non-electrified problem. Thus the breakup is retarded and the thin thread keeps extending until the capillary effect dominates over electric effect near the minimum neck region. This explains the formation of a bigger satellite drop in the electrified problem compared to the non-electrified one. In addition, this does not depend on the viscous effects, so big satellite formation is always observed (see Satiawan & Heister [59] and Collins *et al.* [11]). Consistently, Huebner [26] shows the size of main droplets decreases as the voltage increases.

Next we show that the electric field does not affect the local dynamics near pinching. In Figure 5.18 the evolution of S_{min} is plotted against time, showing the numerical evidence of the predicted slope (dashed line in figure) for infinite and core-annular threads irrespective of the electric field. This is consistent with the observation that $\phi_n \to 0$ at the minimum neck. Additional evidence can be seen from Figure 5.19 where the rescaled function $H(\xi) = S/S_{min}$ is plotted for various cases. Panel (a) shows the collapse of the infinite jet profiles (three profiles) near breakup, $S_{min} \approx 0.005$, and suggests self-similarity. This agrees with the result in Lister & Stone [36] where simulations of a finite viscous drop was carried out. Panel (b) in Figure 5.19 illustrates several jet profiles at the final computed stage for the wide range of parameters of Figure 5.18 and again we see that they almost have the same

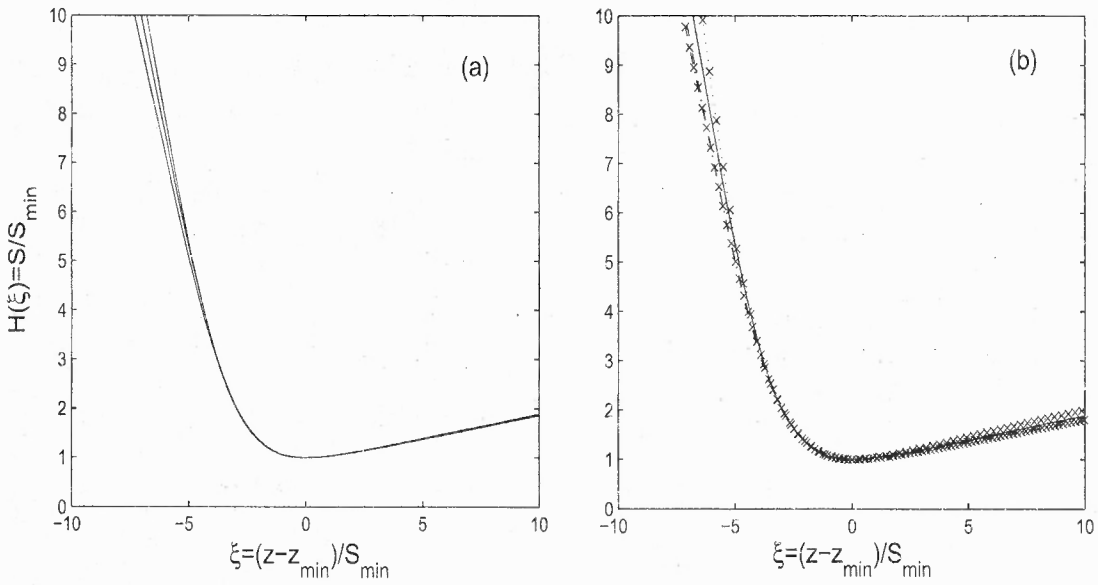

Figure 5.19 Panel (a) shows three profiles from the simulation (rescaled according to $H = S/S_{min}$ and $\xi = (z - z_{min})/S_{min}$) of the infinite jet ($\lambda = 1$), where the collapse suggest self-similarity. Panel (b) outlines local shapes for various parameters that are the same as in Figure 5.18.

shape. The solid line in panel (b) represents the profile for the infinite thread ($d = \infty$ and $E_b = 0$). The other lines have the same parameters as shown in Figure 5.18. Again excellent agreement is observed for both core-annular breakup and electrified breakup. Therefore the angles of the shallow and deep cones take roughly 6.0^o and 78.2^o respectively as described in Lister & Stone [36].

The axial velocity in the case of a radially unbounded thread ($d = \infty$) and core-annular thread still increases slowly. It turns out that the scaling law derived by Lister & Stone [36] still applies for the problems here,

$$w = -0.0243 \ln S_{min} + \text{lower order terms.} \tag{5.75}$$

Figure 5.20 shows that as $S_{min} \to 0$ the curves start converging to the predicted line (dark dotted line) which provides additional evidence of the same local dynamics. Solid line represents the solution of infinite thread which shows a relatively quick

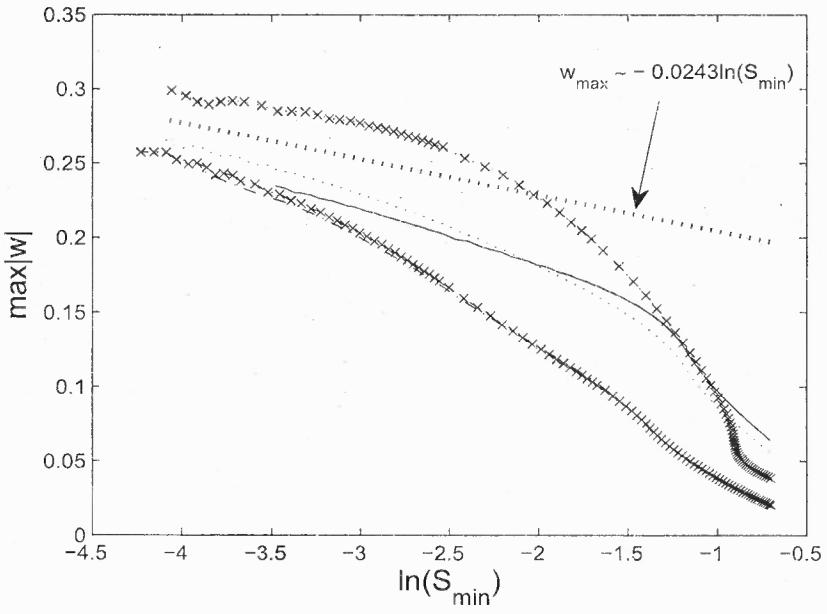

Figure 5.20 Linear increase of $\max|w|$ with $\ln(S_{min})$ for several simulations with the same lines as in Figure 5.18.

convergence than other cases. Again the different lines correspond to the cases shown in Figure 5.18. Intuitively it is suspected that the presence of a tube wall or electric field only reduces the rate of convergence, but eventually the local dynamics follow the non-electrified problem.

5.5.4 Nonlinear Evolution of Annular Layers

In the limit of a thin annulus, even without an electric field the pinch-off in the core thread can be suppressed. A lubrication model was derived and solved by Hammond [22] where an infinite-time singularity is predicted. The capillary drainage and details about the long-time behavior of the thin film was revisited and explored recently by Lister *et al.* [35], who show that the lobe and collar formation depends on the axial length of the film and at large times, they may interact and merge to minimize the surface energy. Figure 5.21 presents a solution calculated with the boundary-integral method developed here for the full Stokes problem, with $\lambda = 1$, $L/a = 20$ and

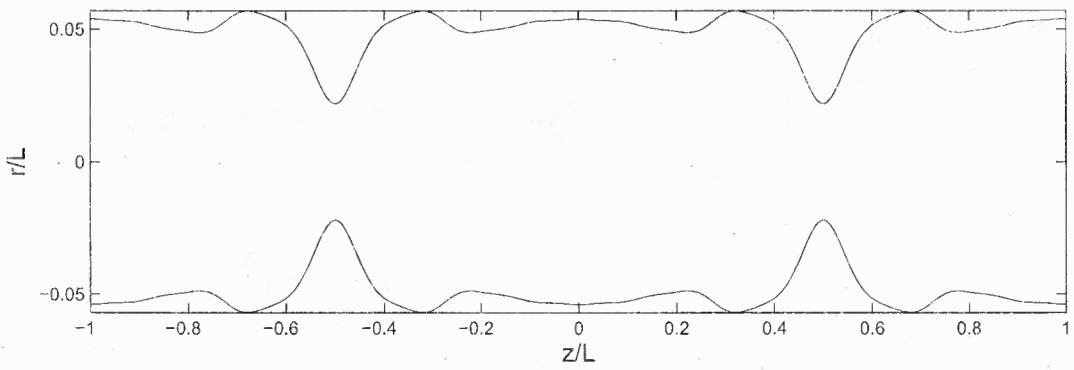

Figure 5.21 Formation of lobes and collars of the annular layer for $E_b = 0$, $ka = \pi/10$ and $d = 1.14$ at $t = 9666.1$.

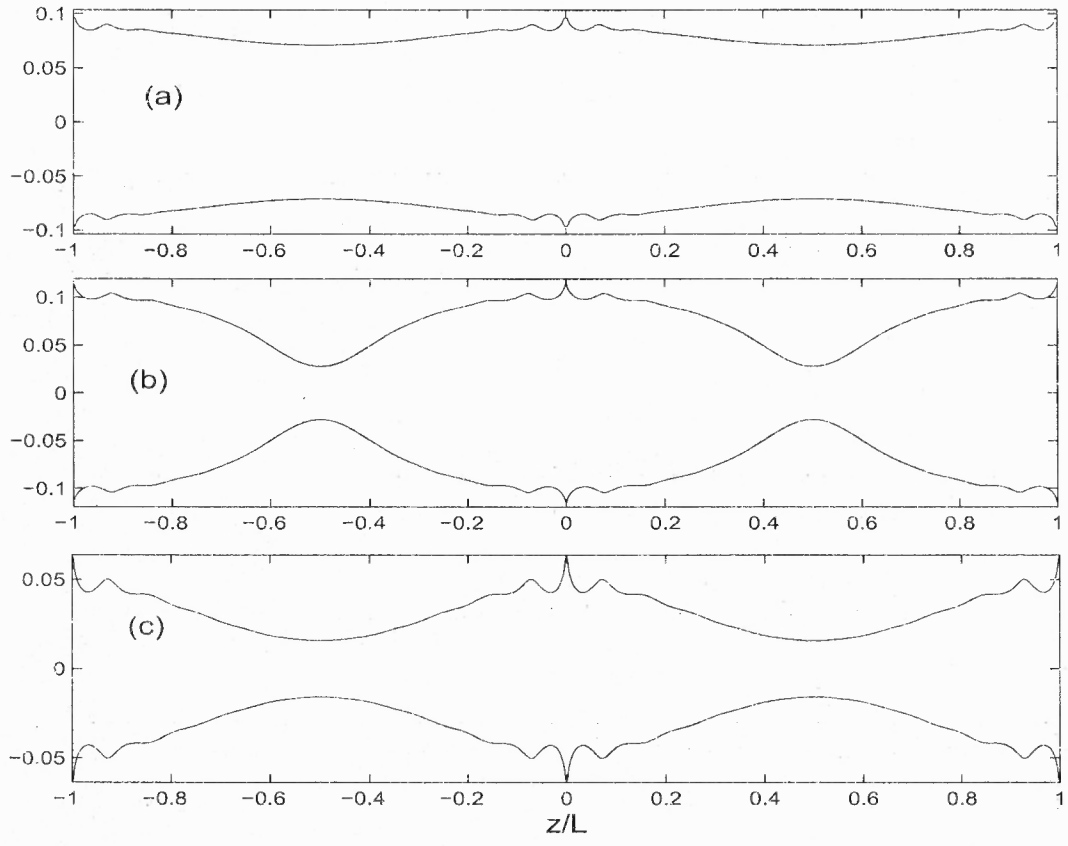

Figure 5.22 Touchdown solutions of the annular layers under radial electric fields for (a) $ka = 0.5$, $d = 1.3$, $E_b = 0.1005$, (b) $ka = 0.5$, $d = 1.5$, $E_b = 0.1257$ and (c) $ka = 0.2$, $d = 2.0$, $E_b = 1.5708$.

$d = 1.14$. The simulation stopped at time (dimensionless) $t = 9666.1$ when the gap (dimensionless) between the tube wall and the interface is about 0.002. The corresponding axial velocity near the minimum gap does not show blowup (not shown here) which implies further fluid motion that may follow the results in Lister *et al.* [35]. However due to the numerical cost we do not pursue this further. Instead the electrified problem is of our interest where, as we discussed previously, a finite-time singularity occurs.

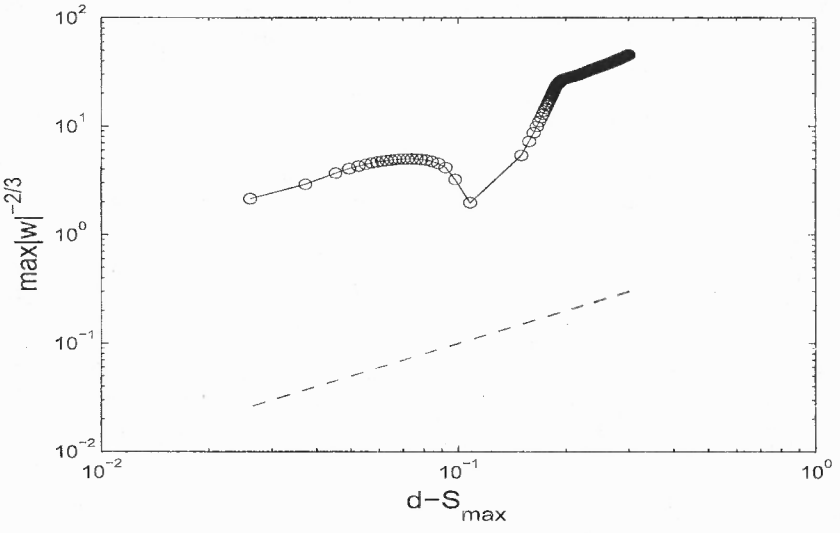

Figure 5.23 Log-log plot of $d - S_{max}$ versus $w_{max}^{-2/3}$ for the case $ka = 0.5$, $d = 1.5$, $E_b = 0.1257$. Dashed line has slope one.

Figure 5.22 outlines a few spike formations for different parameters. Panel (a) shows a solution for small gap $d = 1.3$. For a bigger gap, increasing E_b, i.e. increasing the electric field strength can still produce similar breakup solution ($d = 1.5$ in panel (b) and $d = 2$ in panel (c)). From linear theory it has been found that short waves tend to be unstable. In our simulation, small wavy structures are observed and these are unstable as expected. Additionally the scalings predicted by the lubrication model are also observed in our boundary-integral simulation. Figure 5.23 shows the scalings, $d - S \sim w^{-2/3} \sim \tau^{1/3}$ in the case $d = 1.5$, $E_b = 0.1257$,

which implies that the lubrication model is appropriate and useful near the film rupture. Unfortunately, direct comparison between the boundary-integral simulation and the lubrication results does not show good agreement. Higher order model may be required and meanwhile in the full simulation a sufficiently small gap $(d-1)$ might be necessary in order to apply the lubrication model. But due to the expensive cost these are left for future work.

CHAPTER 6

CONCLUSION

The nonlinear dynamics of perfectly conducting liquid jets or threads subject to a radial electric field has been studied here. In the single jet case (the annular region is passive), we have addressed the effect of the electric field by initially investigating a long-wave model by adopting a local approximation of the electric potential. Pinching is eventually suppressed and stable quasi-static microthreads connected to large drops are found for relatively large outer electrode radii, that is, relatively weak fields. The jet can also be attracted to touch the outer electrode in finite time for different parameter settings, in which case, the touchdown singularities are examined and similarity solutions are constructed analytically. Those results are supported by numerical simulations of the nonlinear partial differential equations with excellent agreement. When the viscosity of the jet is negligible, a Korteweg-de Vries equation is derived in the weakly nonlinear regime in the long wave limit which corresponds to the stabilizing effect of the electric field.

A boundary-integral method has also been implemented to solve the full problem (Stokes equations) when the external viscous drag is reintroduced. The construction of the Green's function for the electrostatic problem was presented in detail. From the numerical results, different breakup scenarios are identified with different parameters. Pinch-off solution is still obtained and a local dynamics analysis reveals the mechanism of bigger satellite drop formation based on the slender-jet approximation. Our results also showed that the local dynamics at pinching is not changed to leading order, by a adding radial electric field; this was shown by illustrating the computed thread profiles in a self-similar frame. Additionally, the instantaneous flow patterns were presented to obtain the nonlinear evolution and fluid motion. As the electric field

strength increases, or the gap between the electrode and fluid interface decreases, a 'spike' solution appears as described in our previous long wave model. In particular, when the annulus is thin enough a lubrication model was derived to describe the touchdown and self-similar scalings are verified through numerical simulations.

Our formulation assumed that the core-thread is a prefect conductor while the surrounding fluid is insulating. Recent research implies that the leaky-dielectric model, which allows for the accumulation of free charge along the interface, may be better suited to describe the electric problem. At this point the finite permittivities and conductivities become important, and this constitutes a wide field for future research.

APPENDIX A

THE COMPONENTS OF MATRIX

In this Appendix, the expressions of the components of the matrix M defined in equation (5.20) are presented.

$$L_1 = 2I_0(k) + kI_1(k), \quad L_2 = -2I_0(k) - kI_1(k),$$

$$L_3 = -2K_0(k) + kK_1(k), \quad L_4 = 2I_0(kd) + kdI_1(kd),$$

$$L_5 = 2K_0(kd) - kdK_1(kd),$$

$$S_1 = 2kI_1(k), \quad S_2 = 2(I_1(k) + kI_0(k)),$$

$$S_3 = -2\lambda kI_1(k), \quad S_4 = -2\lambda(I_1(k) + kI_0(k)),$$

$$S_5 = -2\lambda kK_1(k), \quad S_6 = -2\lambda(kK_0(k) - K_1(k)),$$

$$T_1 = 2k(kI_0(k) - I_1(k)) - \frac{(1 - k^2 - \frac{E_b}{\ln^2(d)}(1 + k\frac{K_0(kd)I_1(k)+I_0(kd)K_1(k)}{I_0(k)K_0(kd)-I_0(kd)K_0(k)}))k}{\omega} I_1(k),$$

$$T_2 = 2kI_1(k)k - \frac{(1 - k^2 - \frac{E_b}{\ln^2(d)}(1 + k\frac{K_0(kd)I_1(k)+I_0(kd)K_1(k)}{I_0(k)K_0(kd)-I_0(kd)K_0(k)}))k}{\omega} I_0(k),$$

$$T_3 = -2\lambda k(kI_0(k) - I_1(k)), \quad T_4 = -2\lambda k^2 I_1(k),$$

$$T_5 = 2\lambda k(kK_0(k) + K_1(k)), \quad T_6 = 2\lambda kK_1(k)k.$$

APPENDIX B

GREEN'S FUNCTIONS

Green's function for potential flow problem:

$$G^R = \frac{F(k)}{\pi\sqrt{(r+r_0)^2+(z-z_0)^2}}, \tag{B.1}$$

$$\frac{\partial G^R}{\partial z} = \frac{1}{\pi\sqrt{(r+r_0)^2+(z-z_0)^2}}\frac{(z_0-z)E}{(r-r_0)^2+(z-z_0)^2}, \tag{B.2}$$

$$\frac{\partial G^R}{\partial r} = \frac{1}{\pi\sqrt{(r+r_0)^2+(z-z_0)^2}}\frac{1}{2r}\left(\frac{r_0^2-r^2+(z-z_0)^2}{(r-r_0)^2+(z-z_0)^2}E-F\right), \tag{B.3}$$

where $k^2 = \frac{4rr_0}{(z-z_0)^2+(r+r_0)^2}$ and F and E are the complete elliptic integrals of the first and second kind with argument k, defined as

$$F(k) = \int_0^{2\pi}\frac{d\theta}{(1-k^2\cos^2\theta)^{1/2}}, \quad E(k) = \int_0^{2\pi}(1-k^2\cos^2\theta)^{1/2}d\theta. \tag{B.4}$$

The Stokeslets and Stresslets used in the boundary-integral formulations for Stokes flow are well documented in the literature (see Pozrikidis [48], Lee & Leal [33]). The Stokeslets in our notation are given by

$$M_{zz} = 2k\left(\frac{r}{r_0}\right)^{1/2}\left(F+\frac{(z-z_0)^2}{(z-z_0)^2+(r-r_0)^2}E\right), \tag{B.5}$$

$$M_{zr} = k\frac{z-z_0}{(r_0r)^{1/2}}\left(F-(r_0^2-r^2+(z-z_0)^2)\frac{E}{(z-z_0)^2+(r-r_0)^2}\right), \tag{B.6}$$

$$M_{rz} = -k\frac{z-z_0}{r_0}\left(\frac{r}{r_0}\right)^{1/2}\left(F+(r_0^2-r^2-(z-z_0)^2)\frac{E}{(z-z_0)^2+(r-r_0)^2}\right), \tag{B.7}$$

$$M_{rr} = \frac{k}{r_0r}\left(\frac{r}{r_0}\right)^{1/2}\left((r_0^2+r^2+2(z-z_0)^2)F-\right.$$
$$\left.(2(z-z_0)^4+3(z-z_0)^2(r_0^2+r^2)+(r_0^2-r^2)^2)\frac{E}{(z-z_0)^2+(r-r_0)^2}\right), \tag{B.8}$$

and the Green's functions in double layer potential ($S_{\alpha\beta} = Q_{\alpha\beta\gamma}n_\gamma$) are given by

$$S_{zz} = (-6r(z-z_0)^3 n_z - 6r^2(z-z_0)^2 n_r)I_{50} + 6rr_0(z-z_0)^2 n_r I_{51}, \tag{B.9}$$

$$S_{zr} = (-6r^2(z-z_0)^2 n_z - 6r^3(z-z_0)n_r)I_{50} +$$
$$(6rr_0(z-z_0)^2 n_z + 12r^2 r_0(z-z_0)n_r)I_{51} - 6rr_0^2(z-z_0)n_r I_{52}, \tag{B.10}$$

$$S_{rz} = (6rr_0(z-z_0)^2 n_z + 6r^2 r_0(z-z_0)n_r)I_{50} +$$
$$(-6r^2(z-z_0)^2 n_z - 6r(z-z_0)(r^2+r_0^2)n_r)I_{51} + 6r^2 r_0(z-z_0)n_r I_{52}, \tag{B.11}$$

$$S_{rr} = (6r^2 r_0(z-z_0)n_z + 6r^3 r_0 n_r)I_{50} + (-6r(z-z_0)(r^2+r_0^2)n_z -$$
$$6r^2(r^2+2r_0^2)n_r)I_{51} + (6r^2 r_0(z-z_0)n_z + 6r(r_0^3+2r^2 r_0)n_r)I_{52}$$
$$- 6r^2 r_0^2 n_r I_{53}, \tag{B.12}$$

where the integrals I_{mn} are defined as

$$I_{mn}(z,r,z_0,r_0) = \frac{4k^m}{(4rr_0)^{m/2}} \int_0^{\pi/2} \frac{(2\cos^2\omega - 1)^n}{(1-k^2\cos^2\omega)^{m/2}} d\omega, \tag{B.13}$$

and k is the same as it appears above.

REFERENCES

[1] ACRIVOS, A., AND RALLISON, J. M. A numerical study of the deformation and burst of a viscous drop in an extensional flow. *J. Fluid Mech. 89* (1978), 191–200.

[2] AMBRAVANESWARAN, B., WILKES, E. D., AND BASARAN, O. A. Drop formation from a capillary tube: comparison of one-dimensional and two-dimensional analyses and occurrence of satellite drops. *Phys. Fluids 14* (2002), 2606–2621.

[3] ARTANA, G., ROMAT, H., AND TOUCHARD, G. Theoretical analysis of linear stability of electrified jets flowing at high velocity inside a coaxial electrode. *J. Electrostatics 43* (1998), 83–100.

[4] ARTANA, G., TOUCHARD, G., AND ROMAT, H. Absolute and convective instabilities in an electrified jet. *J. Electrostatics 40-41* (1997), 33–38.

[5] BAI, R., CHEN, K., AND JOSEPH, D. Lubricated pipelining: stability of core-annular flow. part 5. experiments and comparison with theory. *J. Fluid Mech. 240* (1992), 97–132.

[6] BASSET, A. B. Waves and jets in a viscous liquid. *Am. J. Math. 16* (1894), 93–110.

[7] BENDER, C. M., AND ORSZAG, O. A. *Advanced Mathematical Methods for Scientists and Engineers.* Springer-Verlag, New York; New York, 1999.

[8] CHANDRASEKHAR, S. *Hydrodynamic and Hydromagnetic Stability.* Dover, 1961.

[9] CLOUPEAU, M., AND PRUNET-FOCH, B. Electrostatic spraying in cone-jet mode. *J. Electrostatics 22* (1989), 135–159.

[10] COHEN, I., BRENNER, M. P., EGGERS, J., AND NAGEL, S. R. Two-fluid drop snap-off problem: Experiments and theory. *Phys. Rev. Lett. 83* (1999), 1147.

[11] COLLINS, R. T., HARRIS, M. T., AND BASARAN, O. A. Breakup of electrified jets. *J. Fluid Mech. 588* (2007), 75–129.

[12] CRASTER, R. V., MATAR, O., AND PAPAGEORGIOU, D. T. Pinchoff and satellite formation in surfactant covered viscous threads. *Phys. Fluids 14* (2002), 1364–1376.

[13] DAY, R. F., HINCH, E. J., AND LISTER, J. R. Self-similar capillary pinchoff of an inviscid fluid. *Phys. Rev. Lett 80* (1998), 704.

[14] DUBASH, N., AND MESTEL, A. J. Behavior of a conducting drop in a highly viscous fluid subject to an electric field. *J. Fluid Mech. 581* (2007), 469–493.

[15] DUFFY, D. G. *Green's Functions with Applications.* CRC, 2001.

[16] EGGERS, J. Nonlinear dynamics and breakup of free-surface flows. *Rev. Mod. Phys. 69* (1997), 865.

[17] EGGERS, J., AND DUPONT, T. F. Drop formation in a one-dimensional approximation of the navier-stokes equations. *J. Fluid Mech. 262* (1994), 205–221.

[18] EGGERS, J., AND VILLERMAUX, E. Physics of liquid jets. *Rep. Prog. Phys. 71* (2008), 036601.

[19] GEORGIOU, E., PAPAGEORGIOU, D. T., MALDARELLI, C., AND RUMSCHITZKI, D. S. The double layer-capillary stability of an annular electrolyte film surrounding a dielectric-fluid core in a tube. *J. Fluid Mech. 226* (1991), 149–174.

[20] GLEESON, H., HAMMERTON, P. A., PAPAGEORGIOU, D. T., AND VANDEN-BROECK, J.-M. A new application of the Kortweg-de Vries Benjamin-Ono equation in interfacial electrohydrodynamics. *Phys. Fluids. 19* (2007), 031703.

[21] GRANDISON, S., VANDEN-BROECK, J.-M., PAPAGEORGIOU, D. T., MILOH, T., AND SPIVAK, B. Axisymmetric waves in electrohydrodynamic flows. *J. Eng. Math. 62(2)* (2007), 133–148.

[22] HAMMOND, P. S. Nonlinear adjustment of a thin annular film of viscous fluid surrounding a thread of another within a circular cylindrical pipe. *J. Fluid Mech. 137* (1983), 363–384.

[23] HINCH, E. J. *Perturbation Methods.* Cambridge Universiy Press, 1991.

[24] HOHMAN, M. M., SHIN, M., RUTLEDGE, G., AND BRENNER, M. P. Electrospinning and electrically forced jets. i. stability theory. *Phys. Fluids 13* (2001), 2201.

[25] HOU, T. Y., AND LI, R. Computing nearly singular solutions using pseudo-spectral methods. *J. Comput. Phys. 226* (2007), 379–397.

[26] HUEBNER, A. L. Disintegration of charged liquid jets. *J. Fluid Mech. 38* (1969), 679–689.

[27] HUEBNER, A. L., AND CHU, H. N. Instability and breakup of charged liquid jets. *J. Fluid Mech. 49* (1971), 361–372.

[28] JOHNSON, R. S. *A Modern Introduction to the Mathematical Theory of Water Waves.* Cambridge Universiy Press, 1997.

[29] KEAST, P., AND MUIR, P. Algorithm 688 epdcol - a more efficient pdecol code. *ACM. Trans. Math. Software 17* (1991), 153–166.

[30] KELLY, A. J. On the statistical quantum and practical mechanics of electrostatic atomization. *J. Aerosol Sci. 25* (1994), 1159–1177.

[31] KWAK, S., AND POZRIKIDIS, C. Effect of surfactants on the instability of a liquid thread or annular layer. part i: Quiescent fluids. *Intl J. Multiphase Flow 27* (2001), 1–37.

[32] LEE, H. C. Drop formation in liquid jets. *IBM J. Res. Develop. 18* (1971), 364–369.

[33] LEE, S. H., AND LEAL, L. G. The motion of a sphere in the presence of a deformable interface. *J. Colloid and Interface Science 87* (1982), 81.

[34] LEPPINEN, D. M., AND LISTER, J. R. Capillary pinchoff in inviscid fluids. *Phys. Fluids 15* (2003), 568–578.

[35] LISTER, J., RALLISON, J., KING, A., CUMMINGS, L., AND JENSEN, O. Capillary drainage of an annular film: the dynamics of collars and lobes. *J. Fluid Mech. 552* (2006), 311–343.

[36] LISTER, J. R., AND STONE, H. A. Capillary breakup of a viscous thread surrounded by another viscous fluid. *Phys. Fluids 10* (1998), 2758.

[37] LÓPEZ-HERRERA, J. M., AND GAÑÁN-CALVO, A. M. A note on charged capillary jet breakup of conducting liquids: experimental validation of a viscous one dimensional-model. *J. Fluid Mech. 501* (2004), 303–326.

[38] LÓPEZ-HERRERA, J. M., GAÑÁN-CALVO, A. M., AND PEREZ-SABORID, M. One-dimensional simulation of the breakup of capillary jets of conducting liquids. application to e.h.d. spraying. *J. Aerosol. Sci. 30* (1999), 895–912.

[39] LÓPEZ-HERRERA, J. M., RIESCO-CHUECA, P., AND NÓN CALVO, A. M. G. Linear stability analysis of axisymmetric perturbations in imperfectly conducting liquid jets. *Phys. Fluids 17* (2005), 034106.

[40] MAGARVEY, R. H., AND OUTHOUSE, L. E. Note on the break-up of a charged liquid jet. *J. Fluid Mech. 13* (1962), 151–157.

[41] MELCHER, J. R., AND TAYLOR, G. I. Electrohydrodynamics: a review of the role of interfacial shear stresses. *Ann. Rev. Fluid Mech. 1* (1969), 111–146.

[42] MESTEL, A. J. Electrohydrodynamic stability of a highly viscous jet. *J. Fluid Mech. 312* (1996), 311–326.

[43] NEWHOUSE, L. A., AND POZRIKIDIS, C. The capillary instability of annular layers and liquid threads. *J. Fluid Mech. 242* (1992), 193–209.

[44] PAPAGEORGIOU, D. T. Analytical description of the breakup of liquid jets. *J. Fluid Mech. 301* (1995), 109–132.

[45] PAPAGEORGIOU, D. T. On the breakup of viscous liquid threads. *Phys. Fluids 7* (1995), 1529–1544.

[46] PAPAGEORGIOU, D. T., MALDARELLI, C., AND RUMSCHITZKI, D. S. Nonlinear interfacial stability of core-annular film flows. *Phys. Fluids A 2(3)* (1990), 340.

[47] PAPAGEORGIOU, D. T., AND ORELLANA, O. Study of cylindrical jet breakup using one-dimensional models of the euler equations. *SIAM J. Appl. Math. 59* (1998), 286–317.

[48] POZRIKIDIS, C. *Boundary Integral and Singularity Method for Linearized Viscous Flow.* Cambridge Universiy Press, 1992.

[49] POZRIKIDIS, C. Capillary instability and breakup of a viscous thread. *J. Eng. Math. 36* (1999), 255–275.

[50] RACO, R. J. Electrically supported column of liquid. *Science 160* (1968), 311–312.

[51] RAMOS, A., GONZÁLEZ, H., AND CASTELLANOS, A. Experiments on dielectric liquid bridges subjected to axial electric fields. *Phys. Fluids 6* (1994), 3206–3208.

[52] RAYLEIGH, L. On the instability of jets. *Proc. Lond. Math. Soc. 10* (1878), 4–13.

[53] RAYLEIGH, L. On the equilibrium of liquid conducting masses charged with electricity. *Phil. Mag. 14* (1882), 184–186.

[54] SAVILLE, D. A. Electrohydrodynamic instability: fluid cylinders in longitudinal electric fields. *Phys. Fluids 13* (1970), 2987–2994.

[55] SAVILLE, D. A. Electrohydrodynamic instability: effects of charge relaxation at the interface of a liquid jet. *J. Fluid Mech. 48* (1971), 815–827.

[56] SAVILLE, D. A. Stability of electrically charged viscous cylinders. *Phys. Fluids 14* (1971), 1095–1099.

[57] SAVILLE, D. A. Electrohydrodynamics: the Taylor-Melcher leaky dielectric model. *Ann. Rev. Fluid Mech. 29* (1997), 27–64.

[58] SCHNEIDER, J. M., LINDBALD, N. R., HENDRICKS, C. E., AND CROWLEY, J. M. Stability of an electrified jet. *J. Appl. Phys.. 38* (1967), 2599–2605.

[59] SETIAWAN, E. R., AND HEISTER, S. D. Nonlinear modeling of an infinite electrified jet. *J. Electrostatics 42* (1997), 243–257.

[60] SIEROU, A., AND LISTER, J. R. Self-similar solutions for viscous capillary pinch-off. *J. Fluid Mech. 497* (2003), 381–403.

[61] STONE, H. A., AND LEAL, L. G. Relaxation and breakup of an initially extended drop in an otherwise quiescent fluid. *J. Fluid Mech. 198* (1989), 399–427.

[62] TAYLOR, G. I. Electrically driven jets. *Proc. R. Soc. London A313* (1969), 453–475.

[63] TJAHJADI, M., STONE, H. A., AND OTINO, J. M. Satellite and subsatellite formation in capillary breakup. *J. Fluid Mech. 243* (1992), 297.

[64] TOMOTIKA, S. On the instability of a cylindrical thread of a viscous liquid surrounded by another viscous fluid. *Proc. Roy. Soc. A 150* (1935), 322–337.

[65] VOLKOV, D., PAPAGEORGIOU, D. T., AND PETROPOULOS, P. G. Accurate and efficient boundary integral methods for electrified liquid bridge problems. *SIAM J. Sci. Comput 26* (2004), 2102–2132.

[66] WANG, Q., MÄHLMANN, S., AND PAPAGEORGIOU, D. T. Dynamics of liquid jets and threads under the action of radial electric fields: Microthread formation and touchdown singularities. *Phys. Fluids 21* (2009), 032109.

[67] ZHANG, W. W., AND LISTER, J. R. Similarity solutions for capillary pinch-off in fluids of differing viscosity. *Phys. Rev. Lett. 83* (1999), 1151.

[68] ZHANG, X., AND BASARAN, O. A. An experimental study of dynamics of drop formation. *Phys. Fluids 7* (1995), 1184–1203.